Numerical modelling of flame flashback in premixed tube burners with turbulent flow and high hydrogen content

by

M.J. van Put

to obtain the degree of Master of Science
at the Delft University of Technology,
to be defended publicly on Friday, March 5, 2021 at 12:30.

Student number:	4383877	
Project duration:	March, 2020 – February, 2021	
Thesis committee:	Prof. dr. ir. S.A. Klein,	TU Delft, supervisor
	Prof. dr. D.J.E.M. Roekaerts,	TU Delft, supervisor
	Dr. Ir. M.J. Tummers,	TU Delft, supervisor

An electronic version of this thesis is available at http://repository.tudelft.nl/.

TU Delft

Preface

This final thesis was written as part of the track Energy and Process Technology, which is a specialization of the MSc Mechanical Engineering program of the faculty 3mE at TU Delft. The thesis is a component of the program that is worked on individually and in this specific case took 11 months to complete. Due to COVID, working from home was the norm for the entire period of 11 months. Which meant that all meetings took place digitally and the course of events went slightly differently.

I would like to dedicate this part of the thesis to express my gratitude to all whom have contributed in making this study possible. First of all I would like to thank Sikke Klein, Dirk Roekaerts and Mark Tummers for taking time to help me out with questions and providing guidance on a weekly basis. Furthermore many thanks to Sikke Klein for being the daily supervisor during the process.

Finally many thanks to my family and friends for their support. Without their support, completing my thesis and studies in general would have been much more of a challenge.

M.J. van Put

Amsterdam, February 2021

Abstract

This study presents the numerical modeling of boundary layer flame flashback in premixed tube burners with turbulent flow and high hydrogen content. The modeling approach is based on a RANS turbulence model and a flamelet combustion model using a flame surface density approach in combination with multiple turbulent flame speed correlations to close the chemical source term. The Zimont turbulent flame speed correlation is used to model flame flashback and gain insight in the relevant mechanisms driving the occurrence of the instability. However, this approach has not let to a method to predict in advance that a flame is near flashback conditions. This implicates that the flashback process (when modeled with this specific modeling approach) seems to occur after a certain threshold has been passed. When this threshold has been passed the flashback process is self-amplifying. The ability of the modeling approach based on the Zimont correlation to predict flame flashback is compared to experimental data. Based on this comparison it is concluded that the numerical model performs fairly well. The most notable result is the flame regime map which shows that the numerical model is able to capture that an increase in the hydrogen concentration in the fuel leads to an increased flashback propensity, which was also seen in experimental results. Furthermore, high hydrogen concentration fuels are characterized by high flame speeds and, if sufficiently lean, by a Lewis number lower than 1. In combination with differential diffusion this leads to the thermal diffusive instability. At an attempt to improve the numerical model, two turbulent flame speed correlations that account for these effects were selected and implemented in the numerical model. However, these correlations did not lead to an improved ability of the model to predict flame flashback and flame shape. This reinforces the initial findings that the numerical model with the Zimont turbulent flame speed correlation already performed fairly well.

Contents

Nomenclature

Dimensionless numbers

Re_t	Turbulent Reynolds number
Re_y	Wall-distance-based, turbulent Reynolds number
Da	Damköhler number
Ka	Karlovitz number
Ka_r	Karlovitz number based on reaction zone thickness
Le	Lewis number
$Le_{eff,AFSW}$	Effective Lewis number for the AFSW model [22]
$Le_{eff,Cai}$	Effective Lewis number for the correlation presented by Cai et al. [16]

Symbols

α	Thermal diffusivity (m^2/s)
$\alpha_{c,exp}$	Experimental flame cone angle (°)
$\alpha_{c,Zimont}$	Zimont flame cone angle (°)
δ	Flame front thickness (m)
δ_L	Laminar flame front thickness (m)
δ_R	Reaction zone thickness (m)
δ_{PH}	Preheat zone thickness (m)
$\dot{\omega}_c$	Progress variable source term ($\mathrm{kg}/(\mathrm{m}^3\mathrm{s})$)
$\dot{\omega}_i$	Net rate of increase of mass of species i ($\mathrm{kg}/(\mathrm{m}^3\mathrm{s})$)
ϵ	Turbulent energy dissipation rate ($\mathrm{m}^2/\mathrm{s}^3$)
κ	Thermal conductivity ($\mathrm{W}/(\mathrm{m}\cdot\mathrm{K})$)
μ	Dynamic viscosity ($\mathrm{kg}/(\mathrm{m}\cdot\mathrm{s})$)
μ_t	Eddy viscosity (kg/m^3)
μ_{fuel}	Dynamic viscosity fuel ($\mathrm{kg}/(\mathrm{m}\cdot\mathrm{s})$)
ν	Kinematic viscosity (m^2/s)
ν_η	Kolmogorov velocity scale (m/s)
$\overline{A}$	Projected mean flame surface area (m^2)
$\overline{u_i}$	Ensemble average of the velocity component (m/s)
ϕ	Equivalence ratio (-)
ρ	Density (kg/m^3)

ρ_b Density of burnt mixture ($\mathrm{kg/m^3}$)

ρ_u Density of unburnt mixture ($\mathrm{kg/m^3}$)

ρ_{fuel} Density fuel($\mathrm{kg/m^3}$)

Σ Flame surface density ($\mathrm{m^{-1}}$)

τ_w Wall shear stress ($\mathrm{kg/(m \cdot s^2)}$)

$\tilde{f}$ Favre averaged quantity (-)

A_L Laminar flame front area ($\mathrm{m^2}$)

A_t Turbulent flame front area ($\mathrm{m^2}$)

c Progress variable (-)

C_p Pressure coefficient (-)

c_p Heat capacity ($\mathrm{J/K}$)

D Mass diffusivity ($\mathrm{m^2/s}$)

d, D Pipe internal diameter (m)

D_i Mass diffusion coefficient of species i ($\mathrm{m^2/s}$)

G Stretch factor (-)

h Enthalpy (J/kg)

I Turbulence intensity (%)

K Flame stretch ($\mathrm{s^{-1}}$)

k Turbulent kinetic energy ($\mathrm{m^2/s^2}$)

$K_{curvature}$ Flame curvature ($\mathrm{s^{-1}}$)

K_{strain} Flame strain ($\mathrm{s^{-1}}$)

L_M Markstein length (m)

l_t Integral length scale (m)

l_η Kolmogorov length scale (m)

p Pressure (Pa)

p_0, p_{ref} Reference pressure (Pa)

r Radius (m)

R_i Net rate of production of species i by chemical reaction ($\mathrm{kg/(m^3 s)}$)

S_i Rate of creation of species i by addition from the dispersed phase and the defined source ($\mathrm{kg/(m^3 s)}$)

S_L Laminar flame speed ($\mathrm{m/s}$)

S_L^0 Unstretched laminar flame speed ($\mathrm{m/s}$)

S_t Turbulent flame speed ($\mathrm{m/s}$)

T Mixture temperature (K)

t_t Turbulent time scale (s)

t_η Kolmogorov time scale (s)

T_{ad} Adiabatic flame temperature (K)

T_b Burnt mixture temperature (K)

t_F Chemical time scale (s)

T_{IG} Ignition temperature (K)

T_u Unburnt mixture temperature (K)

th Pipe wall thickness (m)

u' Fluctuating velocity or root mean square of the turbulent velocity fluctuations (m/s)

u^+ Non dimensional velocity (-)

u_i Instantaneous velocity component (m/s)

u_i' Fluctuating velocity component (m/s)

u_τ Friction velocity $(\mathrm{m/s})$

Ub, U_{bulk} Bulk velocity (m/s)

V_u Incoming flow velocity $(\mathrm{m/s})$

y^+ Non dimensional wall distance (-)

Y_F Fuel mass fraction (-)

Y_i Species i mass fraction (-)

Y_i^* Fine scale species i mass fraction (-)

$Y_{F,b}$ Fuel mass fraction in burnt mixture (-)

$Y_{F,u}$ Fuel mass fraction in unburnt mixture (-)

Z Mixture fraction (-)

List of Figures

List of Tables

1

Introduction

The energy transition is the global shift in the energy sector from fossil-based energy production and consumption such as oil, natural gas and coal to renewable energy sources like wind and solar. The main arguments for the energy transition are the need to reduce energy related carbon-dioxide emissions to limit climate change and to prevent depleting energy sources. According to the International Energy Agency the world total energy supply multiplied 2.6 times between 1971 and 2018 [40]. And although progress is being made, fossil fuels remained dominant in the energy supply as can be seen in figure 1.1.

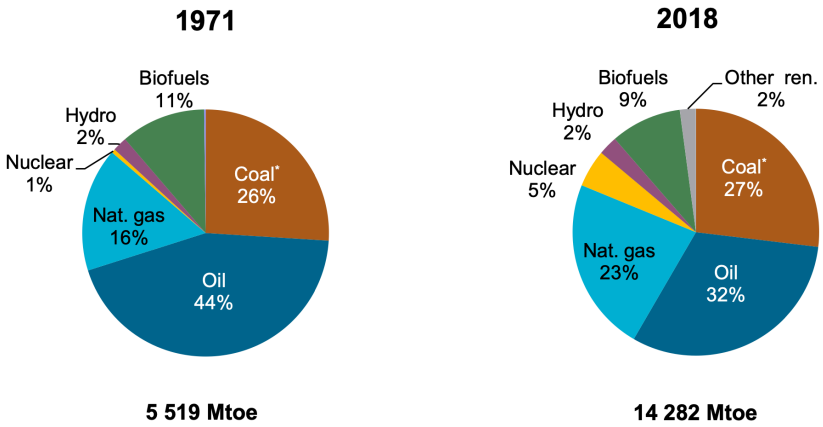

Figure 1.1: World total energy supply by fuel source. Figure taken from [40]

Power generation using renewable energy sources is just part of the energy transition. The transition is also driven by an increased use of technology to boost energy efficiency and the mass deployment of electric transport infrastructure and energy storage. Another key element in the energy transformation is storage of renewable energy, since some renewable energy sources have a variable and uncontrollable output. Current power grids can absorb variation in energy supply up to 10% due to integration of energy generation based on renewable energy sources without major technical problems and substantial extra costs [24]. However, the trend towards usage of renewable energy sources will demand even more flexibility from the energy systems. Energy storage can be used to increase the flexibility of energy systems by decoupling supply and demand [33], meaning that power can be delivered at any time, allowing temporary mismatches between supply and demand of electricity.

Energy can be stored with different methods, one method is to store chemical energy by using a method known as power-to-gas. Power-to-gas is a technology that uses electrical energy to produce a gaseous fuel, such as hydrogen or methane. If the amount of generated electrical energy is greater than the amount used, the surplus can be used to store energy by producing hydrogen. An electrolyzer can split water into hydrogen and oxygen, which can be used as a fuel if needed. Once energy is

stored it should also be converted again into electricity. To ensure a steady and reliable power supply, technologies are required to balance the fluctuations. A gas turbine can be used really well to supply a fluctuating demand due to the combination of a short start up time, a high turn-down ratio and a high efficiency.

Figure 1.2 illustrates how this balancing process between the renewable power supply and the required power would happen. The surplus of power is used to produce hydrogen, 'RE Energy to Storage', and a gas turbine is used in moments of shortcomings, 'Time-shifted Energy from Storage'. The figure shows the possibility for power to gas (hydrogen) technology in combination with a turbine to play a major role in the energy transition.

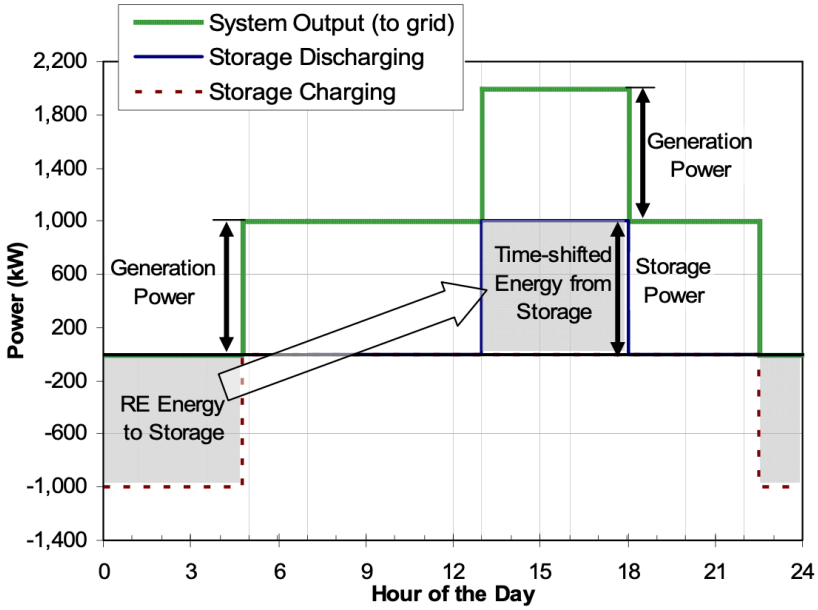

Figure 1.2: Baseload renewables energy time-shift. Figure taken from [29].

As mentioned, a main argument for the energy transition is the need to reduce energy related carbon-dioxide emissions to limit climate change. However, carbon-based fuels still dominate the world energy supply and therefore the emissions of carbon dioxide cannot be minimized easily. A possibility which eliminates these emissions entirely, is the use of carbon-free fuels such as pure hydrogen. However, premixed hydrogen combustion leads to other issues. Which are the origin of hydrogen and two technical issues being nitrous oxides (NOx) emissions and flame flashback. The origin of hydrogen refers to the production method of the hydrogen fuel, since hydrogen can be produced with or without carbon-dioxide emissions. Currently the majority, approximately 95%, of hydrogen is produced with fossil fuels instead of electrolysis [64]. Hydrogen produced from fossil fuels results in carbon emissions. These carbon emissions can be captured instead of released into the atmosphere to reduce pollution. Hydrogen produced with electrolysis does not result in carbon dioxide emissions. The origin of hydrogen is outside the scope of this thesis. The two technical issues encountered in hydrogen combustion, being NOx emissions and flame flashback, are within the scope of this thesis.

The use of hydrogen as a fuel means that carbon dioxide emissions can be eliminated. However the first technical issue that occurs is the formation of NOx. When a hydrogen-air fuel mixture is used, NOx can be produced during hydrogen combustion as an effect of high temperatures that are caused by the thermal mechanism. NOx is harmful to the respiratory tract, can lead to respiratory problems and has a greenhouse impact 300 times higher than that of carbon dioxide on a per molecule basis [11]. Therefore NOx emissions are strictly regulated. The thermal NOx formation mechanism is significant only at temperatures above 1800 K [17], meaning that NOx emissions can be reduced by keeping the flame temperature below 1800 K. Flame temperatures can be reduced by adding more oxygen than needed for stoichiometric conditions, or in other words by applying lean premixed combustion.

The other technical issue encountered during premixed hydrogen combustion is the risk of undesired upstream flame propagation, also known as flashback. Hydrogen is very reactive and when employed in lean premixed combustion it is characterized by inherently unstable processes, premixed hydrogen-air mixtures are especially prone to boundary layer flashback [38].

The combination of the facts that lean combustion can limit the emission of NOx and that hydrogen fuel suffers from flame instabilities such as flashback, has led this thesis to focus on flame flashback during lean premixed combustion of hydrogen-methane-air mixtures with high hydrogen content.

1.1. Thesis outline

The focus of the thesis is on numerical modeling of flame flashback in premixed tube burners with turbulent flow and high hydrogen content using a Reynolds-averaged Navier-Stokes (RANS) turbulence model (i.e. standard $k-\epsilon$) and a flamelet combustion model (i.e. flame surface density with a turbulent flame speed closure approach). More specifically, boundary layer flashback of turbulent jet flames of hydrogen-methane-air mixtures in the TU Delft tube burner was investigated. The numerical results have been verified using experimental data obtained by Filippo Faldella [30] in the combustion facilities of the faculty 3mE at the TU Delft. In short, the purpose of the thesis can be stated as:

- *Predicting flame flashback in premixed tube burners with turbulent flow and high hydrogen content using numerical modeling.*

Multiple numerical methods are available to model fluid flow and combustion. Therefore a number of options were evaluated, which provided a framework to select the numerical modeling approach used in this study. The content of this thesis will now be briefly explained per chapter.

In chapter 2 general theory on turbulence, turbulence modeling, laminar and premixed combustion and flashback mechanisms is provided. The chapter starts with a general description of turbulence and turbulent length scales. Thereafter a summary of turbulence modeling approaches is provided and the RANS equations are presented, including the Reynolds stress term. Then the standard $k-\epsilon$ model and certain quantities which are handy when working with computational fluid dynamics (CFD) are introduced. Furthermore a laminar premixed flame structure and the Bunsen laminar flame speed are described. Then flame stretch and flame instabilities for laminar flames are presented. Thereafter, a basic description of turbulent premixed combustion including combustion regimes and the turbulent flame speed are presented. At last, four different flashback mechanisms are explained.

In chapter 3 a literature review is presented. The first section of the review provides the theory behind combustion modeling approaches that can be applied in combination with a RANS turbulence model. Results found in literature obtained with the combustion models are also presented. This section answers the question:

- *Which combustion model, taking into account the required accuracy and the amount of computational power available, is best suited for this study?*

The second section of chapter 3 presents multiple turbulent flame speed correlations found in literature. The correlations are evaluated specifically for lean premixed combustion of hydrogen-methane-air mixtures with high hydrogen content. This section answers the question:

- *Which correlations could be an improvement with respect to the Zimont turbulent flame speed correlation?*

Chapter 4 presents the numerical setup used in this study. Firstly, it provides information on the set up and validity range of the turbulence model and the combustion model. The chapter also explains the used geometry and mesh. The chapter ends with a brief explanation on determining the needed combustion variables and a table containing these variables.

In chapter 5 the results are presented and discussed. The results are divided in three sections. The first section is dedicated to understanding the flashback process when modeled with the selected turbulence and combustion models and answers two questions:

- *Is it possible to model flame flashback using the selected turbulence and combustion models?*

The first question is whether it is possible to determine the flashback point at all with the models used. If it is possible to determine this point, the next logical question is whether it can be predicted that the flame is near flashback conditions. This is tested in the second section using multiple approaches including flashback theory found in literature and answers the question:

- *Can it be predicted that the flame is near flashback conditions?*

The second section of chapter 5 is dedicated to comparing the numerical results to experimental data and answers the question:

- *How well does the numerical model matches experiments?*

The final section of chapter 5 evaluates the turbulent flame speed correlations selected in the literature review by comparing numerical results as well as experimental data and answers the question:

- *Are the selected turbulent flame speed correlations an improvement with respect to the Zimont turbulent flame speed correlation?*

Finally, conclusions and recommendations for further investigations are presented in chapter 6.

2

General theory

This chapter presents and discusses general theory covering turbulence and combustion topics considered relevant for numerical modeling of flame flashback.

2.1. Turbulence

Turbulence continues to be one of the most daunting topics today and remains an unsolved issue, both from a physical and mathematical perspective [63]. Although it is difficult to give an exact definition of turbulence, its general features can be specified. In fluid dynamics, turbulence or turbulent flow is fluid motion characterized by chaotic vortex like structures, often called eddies. The irregularity is one of the most important features of turbulence. Which is in contrast to a laminar flow where a fluid flows in parallel layers, without any disturbance between those layers. Turbulence results from an instability between inertial and viscous forces, which is usually expressed with the Reynolds number [49].

Turbulent flows consist of eddies of different length scales [63]. Ranging from the integral length scales l_t, set by the geometry of the flow, to the Kolmogorov length scales l_η as seen in figure 2.1. Each different size eddy is characterized by an amount of kinetic energy dependent on the velocity fluctuation at that same eddy length scale. According to the energy cascade, energy from the average flow is supplied to the largest eddies of the integral length scale due to instabilities. The kinetic energy will largely be transferred to smaller eddies when the smaller eddies are stretched by the larger eddies, also known as vortex stretching [63]. The largest of the integral length scale are unstable and break up to smaller eddies. The break up continues until the eddy size reaches the Kolmogorov scale at which the energy will be dissipated through viscosity, therefore turbulence is always dissipative. The energy cascade process occurs in a region called the inertial subrange [26]. The spectrum in this range does not depend on the macroscales and the energy transfer rate is independent of molecular viscosity.

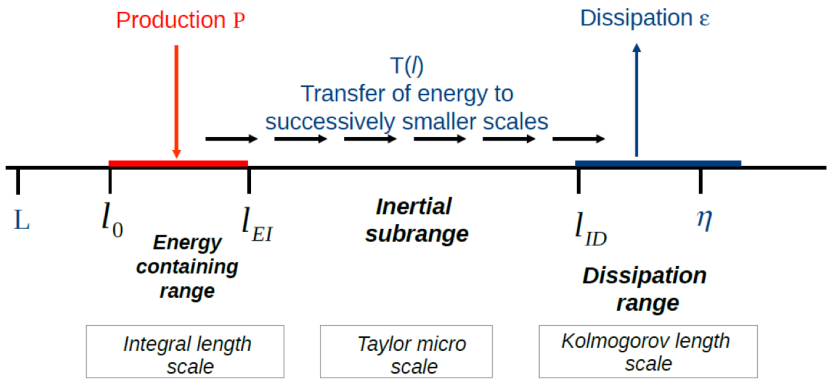

Figure 2.1: Turbulence energy cascade. Figure from [74].

A turbulent flow field can be described using the Reynolds decomposition by splitting an instantaneous quantity, such as the velocity component u_i into an average plus a fluctuating component as

seen in equation 2.1. In which the averaging operator is denoted by a bar above the quantity and the fluctuating component is denoted by a prime. The averaging operator is the ensemble average seen in equation 2.2.

$$u_i = \overline{u_i} + u_i' \tag{2.1}$$

$$\overline{u} = \lim_{N\to\infty} \frac{1}{N} \sum_{\alpha=1}^{N} u^{(\alpha)} \tag{2.2}$$

The Reynolds decomposition can be substituted in the Navier Stokes equations to derive the the Reynolds Averaged Navier Stokes equations (RANS).

Another decomposition which is often encountered when working with computational fluid dynamics (CFD) models is the Favre decomposition. Using the Favre decomposition any quantity *f* can be split into a mean and fluctuating term:

$$f = \tilde{f} + f'' \tag{2.3}$$

With $\widetilde{f''} = 0$ and in which $\tilde{f} = \frac{\overline{\rho f}}{\overline{\rho}}$.

2.1.1. Turbulence scales

In addition to the normal Reynolds number, a Reynolds number also exists specific for turbulent flows. This is known as the turbulent Reynolds number. The turbulent Reynolds number is usually defined at the energy containing scale i.e. l_t. In this case the velocity scale scales with u' which is the square root of the total turbulent kinetic energy. Therefore the turbulent Reynolds number is equal to:

$$\mathrm{Re}_t = \frac{u' l_t}{\nu} \tag{2.4}$$

The Reynolds numbers can be defined at different significant scales, such as the Kolmogorov scale. The Reynolds number associated with the Kolmogorov scale is equal to unity, since the flow at the Kolmogorov scale is dominated by viscosity and the viscous forces balance the inertial forces.

When defining the root mean square of the turbulent velocity fluctuations u' at the integral length scale i.e. $u'(l_t)$ and assuming isotropic turbulence, the total turbulent kinetic energy can be defined as seen in equation 2.5 [26]. The turbulent kinetic energy is produced in the energy containing scale seen in figure 2.1.

$$k \equiv \frac{1}{2}(u_i'^2 + u_j'^2 + u_k'^2) = \frac{3}{2}u'^2 \tag{2.5}$$

The rate of energy transfer in the inertial subrange, can be seen as the amount of energy per unit mass divided by the time needed for dissipation. And is usually referred to as the turbulent energy dissipation rate ϵ. The amount of time needed for dissipation is known as the integral turbulent time scale and is defined as:

$$t_t = \frac{l_t}{u'} \sim \frac{k}{\epsilon} \tag{2.6}$$

Using the integral turbulent time scale it is now possible to determine the turbulent energy dissipation rate as seen in equation 2.7. The turbulent dissipation rate scales with the total turbulent kinetic energy to the power 3/2 divided by the integral length scale. The dissipation occurs in the the dissipation range seen in figure 2.1.

$$\epsilon = \frac{u'^3}{l_t} \sim \frac{k^{\frac{3}{2}}}{l_t} \tag{2.7}$$

The dissipation range of the flow which occurs at the Kolmogorov scale [63] can also be characterized using scaling parameters. Due to conservation of energy, the rate at which energy is dissipated at the Kolmogorov scale has to be the same as the kinetic energy transferred from an eddy to another in the inertial subrange. The scaling parameters of the energy containing scale of the flow u' and l_t are not of direct importance to the Kolmogorov scale, since the characteristics are lost during the break up of larger eddies into smaller eddies. Considering that the energy of the flow will be dissipated through

viscosity at the Kolmogorov scale the essential parameters are the viscosity ν and the amount of energy per unit time that is dissipated ϵ. Using the scaling parameters ν and ϵ, the Kolmogorov length, time and velocity scales can be defined as:

$$l_\eta = \left(\frac{\nu^3}{\epsilon}\right)^{\frac{1}{4}}, \quad t_\eta = \left(\frac{\nu}{\epsilon}\right)^{\frac{1}{2}}, \quad v_\eta = (\nu\epsilon)^{\frac{1}{4}} \tag{2.8}$$

2.2. Modeling turbulent flow

Since the equations describing a turbulent flow can only be solved directly for simple flow cases, a turbulence model should be used to predict most turbulent flows. The turbulence modelling approaches can be divided in three main methods, being Reynolds-averaged Navier-Stokes (RANS), Large Eddy Simulations (LES) and Direct Numerical Simulation (DNS). The three methods can be divided on the scales of motion that are resolved. In a RANS model all turbulence scales are modelled, a LES method resolves the large scale eddies and models the smaller scales. And a DNS method solves the full instantaneous Navier-Stokes equations without an extra model for turbulence, meaning all scales of motion, down to the Kolmogorov scale are resolved. Usually the accuracy of a turbulence model increases with an increase in the amount of resolved turbulence scales, however this does come at the cost of an increase in computational power. Figure 2.2 provided by Poinsot and Veynante [68], shows an example of the information (in this case temperature) that is captured for a stabilized flame at a given point using the different modeling approaches.

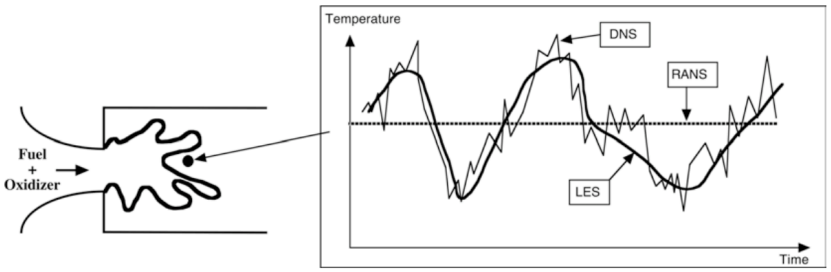

Figure 2.2: Time evolutions of local temperature computed with DNS, RANS or LES in a turbulent flame brush. Figure from [68].

2.2.1. RANS

To ease the numerical modelling of the Navier-Stokes equations, a possibility is the use of Reynolds-averaged Navier-Stokes (RANS) equations. The RANS equations can be found by using the principle of the substitution of the decomposed velocity components seen in equation 2.1 in the Navier-Stokes equations and applying time averaging. The RANS conservation equations for mass and momentum seen in equation 2.9 and equation 2.10 respectively are obtained by applying Favre averaging instead of Reynolds averaging. Due to the fact that for flows with a variable density, Reynolds averaging introduces other unclosed correlations between flow quantities and density fluctuations. Therefore Favre averaged Navier Stokes equations are more convenient when using CFD codes [68]. RANS equations can be used in combination with approximations (e.g. subsection 2.2.3) fit for the specific flow properties to give a description of the mean flow field. However the velocity fluctuations still appear in the RANS equations due to the Navier-Stokes equations being non linear. The non linear term in the RANS equations, $\overline{\rho}\widetilde{u_i''u_j''}$ is known as the Reynolds stress. To close the RANS equations the Reynolds stress should be modelled.

$$\frac{\partial\overline{\rho}}{\partial t} + \frac{\partial}{\partial x_i}(\overline{\rho}\tilde{u}_i) = 0 \tag{2.9}$$

$$\frac{\partial\overline{\rho}\tilde{u}_i}{\partial t} + \frac{\partial}{\partial x_i}(\overline{\rho}\tilde{u}_i\tilde{u}_j) + \frac{\partial\overline{p}}{\partial x_j} = \frac{\partial}{\partial x_i}\left(\overline{\tau}_{ij} - \overline{\rho}\widetilde{u_i''u_j''}\right) \tag{2.10}$$

2.2.2. Closure of Reynolds stress

The primary purpose of a RANS model is to close the Reynolds stress. The Reynolds stress term in the momentum equation can be closed by introducing the Boussinesq closure hypothesis [63] which uses the concept of an eddy viscosity, also known as the turbulent dynamic viscosity in order to model the momentum transfer caused by turbulent eddies. The equation used to express the Reynolds stress is mathematically analogous to the stress rate of strain relationship for a Newtonian fluid [49]. The equation for the Reynolds stress is defined as [68]:

$$\overline{\rho}\widetilde{u_i''u_j''} = -\mu_t\left(\frac{\partial\tilde{u}_i}{\partial x_j} + \frac{\partial\tilde{u}_j}{\partial x_i} - \frac{2}{3}\delta_{ij}\frac{\partial\tilde{u}_k}{\partial x_k}\right) + \frac{2}{3}\overline{\rho}k \tag{2.11}$$

In which μ_t is the eddy viscosity and δ_{ij} is the Kronecker symbol. The last term in equation 2.11 is the turbulent kinetic energy k defined in equation 2.5. To model the eddy viscosity multiple approaches have been proposed. Being the algebraic approach without additional balance equations such as the Prandtl mixing length model, followed by models using one additional transport equation such as the Prandtl-Kolmogorov model and finally two equation models such as the $k-\epsilon$ and $k-\omega$ models [68].

2.2.3. Standard k - epsilon model

In this study the standard $k-\epsilon$ model [41] will be used, meaning the eddy viscosity is modeled as:

$$\mu_t = \overline{\rho}C_\mu\frac{k^2}{\epsilon} \tag{2.12}$$

In which ϵ is the turbulent dissipation rate and C_μ is a model constant set to 0.09. The $k-\epsilon$ model is a two equation model, meaning the model is based on transport equations for the turbulent kinetic energy k and the turbulent dissipation rate ϵ [68]:

$$\frac{\partial}{\partial t}(\overline{\rho}k) + \frac{\partial}{\partial x_i}(\overline{\rho}\tilde{u}_i k) = \frac{\partial}{\partial x_i}\left[\left(\mu + \frac{\mu_t}{\sigma_k}\right)\frac{\partial k}{\partial x_i}\right] + P_k - \overline{\rho}\epsilon \tag{2.13}$$

$$\frac{\partial}{\partial t}(\overline{\rho}\epsilon) + \frac{\partial}{\partial x_i}(\overline{\rho}\tilde{u}_i \epsilon) = \frac{\partial}{\partial x_i}\left[\left(\mu + \frac{\mu_t}{\sigma_\epsilon}\right)\frac{\partial \epsilon}{\partial x_i}\right] + C_{\epsilon 1}\frac{\epsilon}{k}P_k - C_{\epsilon 2}\overline{\rho}\frac{\epsilon^2}{k} \tag{2.14}$$

The source term for the turbulent kinetic energy P_k is given by:

$$P_k = -\overline{\rho}\widetilde{u_i''u_j''}\frac{\partial\tilde{u}_i}{\partial x_j} \tag{2.15}$$

The model constants can be altered, however they are usually defined as [68]:

$$\sigma_k = 1.0, \quad \sigma_\epsilon = 1.3, \quad C_{\epsilon 1} = 1.44, \quad C_{\epsilon 2} = 1.92 \tag{2.16}$$

Next to the standard $k-\epsilon$ model, improved $k-\epsilon$ models exist. Such as the RNG $k-\epsilon$ model and the realizable $k-\epsilon$ model. In the RNG $k-\epsilon$ model an additional term is included in the transport equation for the turbulent dissipation. Which improves the accuracy for rapidly strained flows [86]. Also the effect of swirl on turbulence is included, enhancing accuracy for swirling flows. In the realizable $k-\epsilon$ model the model constant C_μ is no longer a constant, but depends on k and ϵ. A benefit of the realizable k- ϵ model is that it more accurately predicts the spreading rate of planar and round jets [75]. Furthermore it is probable that the model performs better for flows involving rotation, boundary layers under strong adverse pressure gradients, separation, and re-circulation. The standard $k-\epsilon$ model can also be improved with the use of wall functions, see subsection 2.2.4.

2.2.4. Non dimensional wall distance

Large gradients are observed in the viscosity affected regions near the walls, which greatly affects turbulent flows. A good prediction of a wall bounded turbulent flow is determined by an accurate representation of the velocity profile in the viscosity affected near wall region. Some turbulence models such as the previously described standard $k-\epsilon$ model are only valid for fully developed turbulent flow and do not perform well in the area close to the wall. Two approaches generally used in CFD to deal

with the viscosity affected near wall region are the use two-layers models or the use of wall functions. A two layer model applies a low Reynolds number turbulence model (used in this study, see subsection 4.1.1) in the viscosity affected near wall region. The low Reynolds number turbulence model is smoothly blended with the standard $k-\epsilon$ model which is applied in the fully turbulent region, hence the name two-layer model. Another possible approach to deal with the viscosity affected near wall region is the use of wall functions which describe the flow properties in the near wall region. The wall function approach relies on the universal law of the wall, which states that the velocity distribution in the vicinity of a wall is similar for most turbulent flows. To determine whether wall functions can be applied, the distance to the wall can be evaluated using the dimensionless wall distance y^+. The non dimensional wall distance is defined as [63]:

$$y^+ = \frac{yu_\tau}{\nu} \tag{2.17}$$

In which y is the absolute distance from the wall, ν is the kinematic viscosity and u_τ is the friction velocity. The friction velocity is a form of shear stress rewritten in units of velocity and defined as:

$$u_\tau = \sqrt{\frac{\tau_w}{\rho}} \tag{2.18}$$

In which τ_w is the wall shear stress and ρ is the density of the fluid. Using the friction velocity, a non dimensional velocity can be introduced as well:

$$u^+ = \frac{u}{u_\tau} \tag{2.19}$$

2.2.5. Wall regions and layers

Fluid flowing over a solid boundary with a no slip boundary condition, will develop a boundary layer due to friction. Which creates a thin layer of fluid near the surface of the boundary in which the velocity changes from zero at the surface to the free stream velocity away from the surface. The boundary layer flow can be divided into three layers being the inner layer, the overlap layer and the outer layer. The mean velocity profile in these layers can be presented using the normalized velocity profile u^+ and the normalized wall normal distance y^+. This enables a classification of the flow regions [70], see figure 2.3:

- Viscous sublayer $y^+ < 5$, where viscous shear forces are dominant and the velocity profile is linear:
$$u^+ = y^+ \tag{2.20}$$
- Buffer layer $5 < y^+ < 30$, which is a transition region between the viscous sublayer and the logarithmic layer. In this region viscous and turbulence forces are of similar magnitude and the velocity profile is not well defined.
- Logarithmic region $y^+ > 30$, the turbulent forces dominate the flow and the velocity profile is described by a logarithmic wall law, also known as the law of the wall:
$$u^+ = \frac{1}{\kappa}\ln y^+ + B \tag{2.21}$$
In which κ is the Kármán constant equal to 0.41 and B is equal to 5.2.

The viscous sublayer and the buffer layer are part of the inner layer, where viscous shear forces are dominating. The logarithmic region, where both turbulent and viscous shear forces are important belongs to the log-law region in the inner layer. This region is also referred to as the overlap layer. Finally there is the outer layer, where turbulent forces dominate.

As described in the previous subsection, the wall function approach relies on the universal law of the wall, which states that the velocity distribution in the vicinity of a wall is similar for most turbulent flows. However if a study aims at identifying flow instabilities such as boundary layer separation, wall

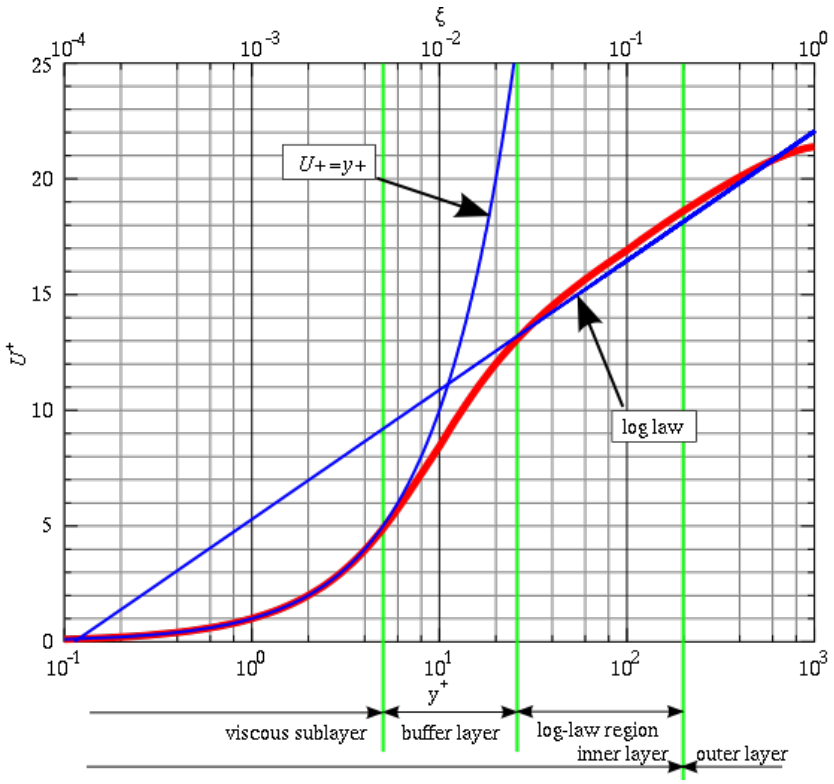

Figure 2.3: The law of the wall, figure taken from [85].

functions should not be used since the log-based wall functions do not correctly predict the velocity profile. Since this study focuses on boundary layer flashback, the viscosity affected near wall region should be resolved without the application of wall functions to obtain accurate results. Therefore a two-layer model is applied, which uses a low Reynolds number turbulence model in the viscosity affected near wall region and the standard $k-\epsilon$ model in the fully turbulent region. This method is further explained in subsection 4.1.1.

2.3. Premixed combustion

The amount of excess fuel or oxidizer in a premixed fuel mixture is determined using the equivalence ratio ϕ, which is defined as the fuel to air ratio of the mixture divided by the fuel-air ratio at stoichiometric conditions. A stoichiometric mixture is indicated by an equivalence ratio equal to 1. A lean mixture has an equivalence ratio lower than 1 and a rich mixture higher than 1. The use of lean premixed combustion results in excess air in the premixed fuel mixture, which has a cooling effect on the flame. The temperature dependent formation of NOx can be limited due to this cooling effect.

2.4. Laminar premixed combustion

Figure 2.4 shows a laminar premixed one dimensional flame structure. The premixed mixture burns with a mixture dependent laminar flame speed S_L (S_L^0 if the flame is unstretched), defined as the propagation speed of the flame front relative to the mixture flow. The structure seen in figure 2.4 assumes that the flame is thin, one-dimensional, stationary and the reaction profile is single-step with large activation energy, as indicated by Benim and Syed in [8]. Based on these assumptions, it can be assumed that no reaction occurs until the ignition temperature, indicated by T_{IG}, is reached. Once the ignition conditions have been reached, the reaction occurs very quickly until the reactant is consumed. Figure 2.4 also shows how the structure can be divided into different zones. The side upstream of the flame front is defined as the unburned side. The flame front itself, with thickness δ_L, can be divided in the preheat zone, with thickness δ_{PH}, and the reaction zone, with thickness δ_R. The zone downstream of the flame front is defined as the burned side.

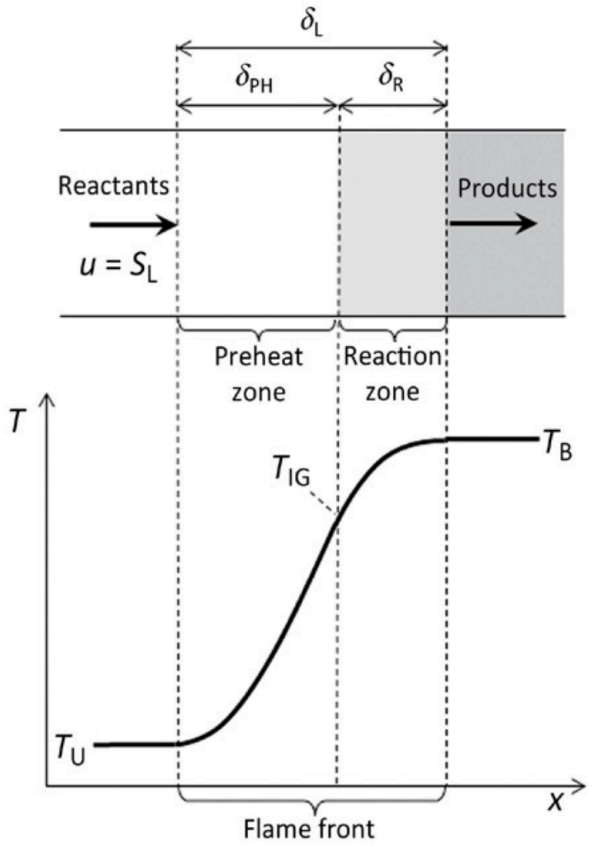

Figure 2.4: Schematic of a one-dimensional planar and unstretched flame front, figure from [8].

In the reaction zone products are formed from reactants, which generates heat. The generated heat diffuses from the reaction zone to the preheat zone while reactants diffuse in the opposite direction. The balance between thermal diffusion α and mass diffusion D is described with the Lewis number, seen in equation 2.22. The Lewis number indicates whether heat or mass diffusion is dominant. In

lean hydrogen combustion the Lewis number is smaller than one. This means that hydrogen diffusion towards the reaction zone occurs at a higher rate than the diffusion of heat out of the reaction zone into the preheat zone. Therefore, the enthalpy in the reaction zone will increase locally, which leads to an increase of the local flame velocity [5].

$$Le = \frac{\alpha}{D} \tag{2.22}$$

2.4.1. Bunsen laminar flame speed

The Bunsen burner is a device to generate a laminar premixed flame. The burner consists of a pipe which acts as a mixing chamber for air and fuel. A flame can be established at the pipe outlet due to the evenly premixed mixture. If the velocity of the incoming flow, indicated by V_u in figure 2.5, is larger than the laminar flame speed the flame front will burn at an angle with respect to the pipe axis resulting in the conical flame shape. The relation between the laminar flame speed, cone angle and incoming flow velocity is given by equation 2.23:

$$S_L = V_u \sin\theta \tag{2.23}$$

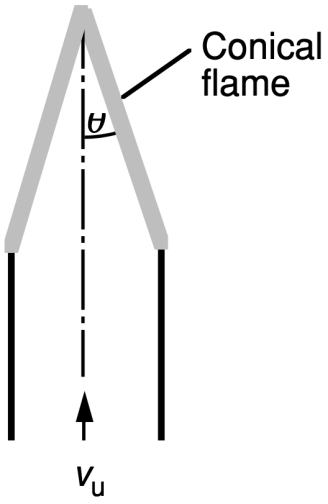

Figure 2.5: Bunsen burner schematic. Figure from [84].

The described relation between the laminar flame speed, cone angle and incoming flow velocity for the Bunsen burner applies to laminar flames. However it can also be used to describe aspects of turbulent flames as will be seen in the results of this study. Using the linearised flame front (see subsection 5.2.2) the flame cone angle can be determined. The flame cone angle can be related to certain flame characteristics such as the velocity increase over the flame front.

2.4.2. Flame stretch

Flame stretch *K* is a quantity which measures the amount of stretch of a flame surface due to flame curvature and velocity field strain [68]. The flame stretch rate is defined as the normalized time rate of change of the flame front area:

$$K = \frac{1}{A}\frac{dA}{dt} \tag{2.24}$$

The flame stretch can also be written as the sum of the two phenomena causing flame stretch as seen in equation 2.25. Poinsot and Veynante [68] use figure 2.6 to illustrate typical configurations used to study the different phenomena causing flame stretch.

$$K = K_{strain} + K_{curv} \tag{2.25}$$

As indicated by Poinsot and Veynante [68], the only theory used to study the stretched flame speeds comes from asymptotic theories. These theories suggests that if the Karlovitz number (see subsection

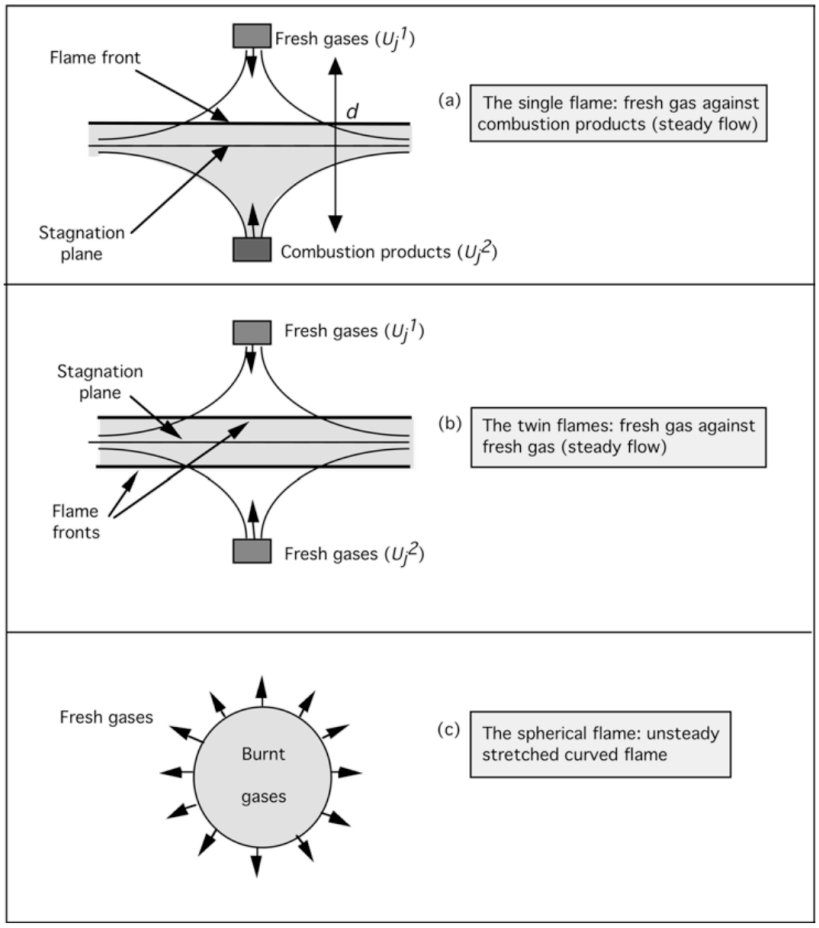

Figure 2.6: Examples of typical configurations used to study flame stretch in laminar premixed flames. (a) and (b) show flames that are stretched due to flow strain and (c) shows stretch due to flame curvature. Figure from [68].

2.5.1) is much smaller than one, meaning that the flame is weakly stretched, the dependency of the flame on the various stretch phenomena can be assumed to be the same. In this case the stretched laminar flame speed can be expressed by means of the Markstein length and is defined as seen in equation 2.26. The mixture dependent Markstein length L_M determines the sensitivity of the flame speed to flame stretch. It depends on parameters such as mixture equivalence ratio and the Lewis number. If the Lewis number is non unity the unbalanced thermal and mass diffusion can increase or decrease the laminar flame speed of stretched flames as will be further explained in subsection 2.4.3.

$$S_L^s = S_L^0 - L_M K \tag{2.26}$$

For the combustion modeling approach used in this study, ANSYS Fluent provides one option to include the effect of flame stretching. Flame stretching can be taken into account by multiplying the source term of the progress variable (see subsection 3.1.3) with a stretch factor G, which can range from 0 to 1. The ANSYS Fluent Theory Guide [4] states that this stretch factor represents the probability that the stretching will not quench the flame. The stretch factor is equal to 1 if there is no stretching, meaning that the probability that the flame will be unquenched is 100%. For hydrogen combustion, stretch leads to an increase of the flame speed. Therefore the option provided in Fluent to include flame stretching is not useful for hydrogen combustion.

2.4.3. Laminar flame front instabilities

Various instabilities, such as thermodiffusive instabilities, can appear along premixed flame fronts. Thermodiffusive instabilities are controlled by unbalanced thermal and mass diffusion effects, or in

other words a non unity Lewis number. The thermodiffusive instabilities are explained by Poinsot and Veynante [68] using figure 2.7.

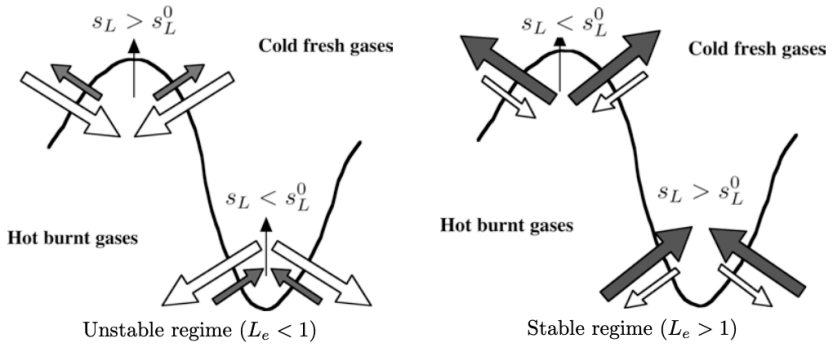

Figure 2.7: Sketch of thermodiffusive instabilities. For a Lewis number smaller than one, mass diffusion (indicated by the white arrows) is larger than thermal diffusion (indicated by the grey arrows) and the wrinkling of the flame front is enhanced (left figure). For a Lewis number greater than one, a stable planar flame is obtained (right figure). Figure from [68].

To summarize; if the Lewis number is lower than one, which is the case with lean hydrogen combustion, the mass diffusion of reactants is higher than the thermal diffusion. If the flame shape is convex with respect to the fresh gases, reactants diffuse faster towards the burnt side than the heat diffuses towards the cold unburnt side. Therefore the reactants are heated, resulting in an increase in the local flame speed with respect to the speed of the planar flame front. While for a flame front that is convex with respect to the burnt side, reactants diffuse in a large region due to the convex flame shape and the flame velocity is decreased with respect to the speed of the planar flame front. This means that the flame front surface increases and the situation is inherently unstable.

On the other hand if the Lewis number is greater than one, the mass diffusion is lower than the thermal diffusion, leading to an opposite effect. Meaning that the thermodiffusive instabilities have a stabilizing effect on a flame with a Lewis number greater than one.

Another contributing effect to the thermodiffusive instabilities is the effect of differential diffusion. These effects are caused by a difference in mass diffusion between the fuel and the oxidizer, leading to local differences in equivalence ratio.

2.5. Turbulent premixed combustion

The presence of combustion in a turbulent flow increases the complexity. In real world engineering applications, combustion is often accompanied by turbulent flow [87]. In turbulent combustion there is interaction between the turbulent flow and the flame [68]. Heat released by combustion will cause a thermal expansion and drive the flow, potentially resulting in turbulence. The expansion due to combustion results in a reduction of fluid density, which has a damping effect on vorticity and may decrease turbulence. The turbulent velocity fluctuations curve and wrinkle the flame front, as a result turbulent premixed flames are characterized by higher flame surface and burning velocity than laminar premixed flames [84]. Furthermore enhanced mixing due to turbulence can amplify combustion, but once turbulence intensity reaches a certain level it can also result in flame extinction.

2.5.1. Combustion regimes

In 2.1.1 The characteristic scales of turbulent flow have been defined. Combustion regimes can be defined using the length scales defined in section 2.4, being the flame thickness δ, and the reaction zone thickness δ_r which is usually much smaller than the flame thickness. Different turbulent combustion regimes can be classified based on the thickness and speed of the flame front, unstretched laminar flame speed S_L^0 of the mixture and turbulent eddies. Usually this is done in terms of the turbulent Reynolds, Damköhler and Karlovitz number. The turbulent premixed combustion regimes can be classified using the specified dimensionless numbers using the Borghi diagram. Such as the diagram seen in figure 2.8 proposed by Peters [66].

Assuming that the Schmidt number seen in equation 2.27 is equal to unity, the flame thickness δ

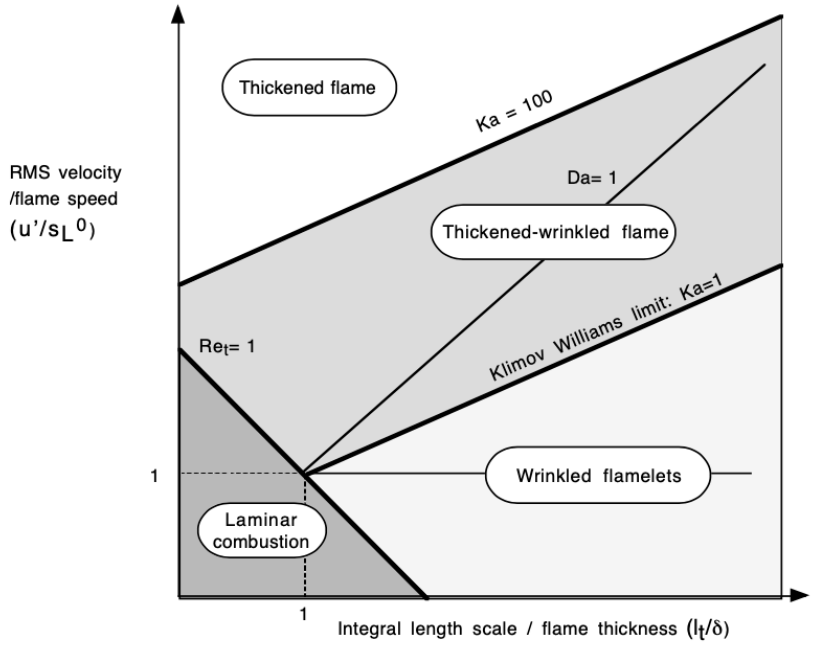

Figure 2.8: Combustion (Borghi) diagram separating combustion regimes in terms of length (l_t/δ) and velocity (u'/s_L^0), figure taken from [68].

and chemical time scale t_F are defined as in equation 2.28. The turbulent Reynolds, Damköhler and Karlovitz number are defined by Peters [65] as seen in equations 2.29, 2.32 and 2.30. The Damköhler number is the ratio of the integral turbulent time scale to the chemical time scale, while the Karlovitz number is the ratio of the chemical time scale to the Kolmogorov time scale.

$$Sc = \frac{\nu}{D} \tag{2.27}$$

$$\delta = \frac{D}{S_L^0} = \frac{\nu}{S_L^0}, \quad t_F = \frac{\delta}{S_L^0} \tag{2.28}$$

$$\mathrm{Re}_t = \frac{u' l_t}{S_L^0 \delta} \tag{2.29}$$

$$Ka = \frac{t_F}{t_\eta} = \frac{\delta^2}{l_\eta^2} = \frac{v_\eta^2}{{S_L^0}^2} \tag{2.30}$$

The Karlovitz number can be recast in various forms, however it should be seen as the ratio of the chemical time scale t_F and the Kolmogorov time scale. Which means that if all chemical reactions occur faster than the smallest turbulent time scale, the flame thickness is smaller than the smallest turbulent scale and the Karlovitz number is smaller than unity, therefore turbulence does not affect the flame structure. An additional Karlovitz number based on the reaction zone thickness can be defined as in equation 2.31. If Ka_r is equal to unity the Kolmogorov scale is equal to the reaction zone thickness.

$$Ka_r = (\frac{\delta_r}{l_\eta})^2 \tag{2.31}$$

The Damköhler number is defined as in equation 2.32. A large Damköhler number implies small chemical time scales compared to the integral turbulent time scales which means turbulence is not able to affect the flame structure in a significant way. A low value for the Damköhler number implies the opposite which is a flame strongly influenced by turbulence.

$$Da = \frac{t_t}{t_F} = \frac{l_t S_L^0}{u' \delta} \tag{2.32}$$

Regime	Dimensionless numbers	Description
Flamelet	Ka <1 and Da>1	Flame is thinner than turbulent scales
Thickened-wrinkled flame or thin reaction zones	1 < Ka <100	Small turbulent scales can enter the flame front
Thickened flame	Ka >100 (or Ka_r >1) and Da <<1	All turbulent time scales are smaller than the chemical time scales

Table 2.1: Combustion regimes

The relationship between the turbulent Reynolds number, the Karlovitz number and the Damköhler number is given by the following relation:

$$\mathrm{Re}_t = Da^2 Ka^2 \tag{2.33}$$

Using the Karlovitz and the Damköhler number in combination with the diagram in figure 2.8 various regimes can be identified as seen in table 2.1. A visual representation of a wrinkled and thickened-wrinkled flamelet is provided in figure 2.9.

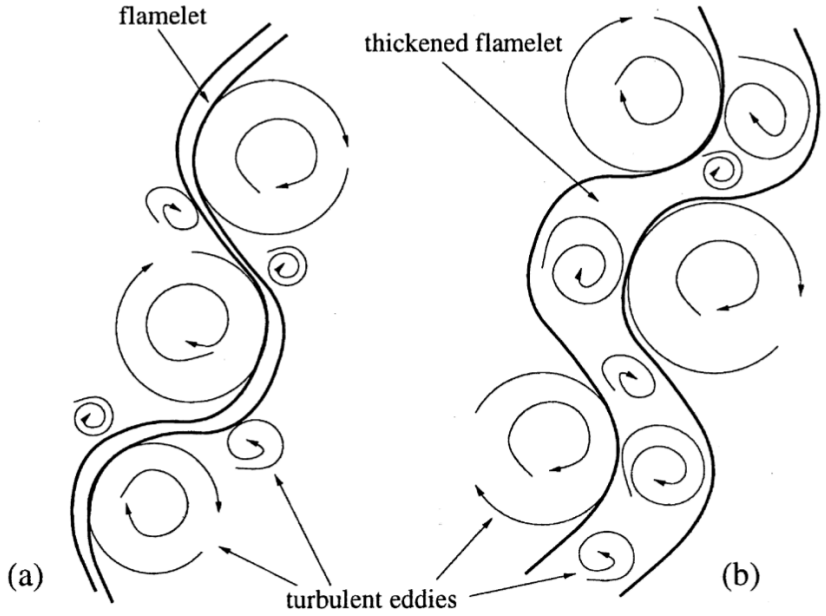

Figure 2.9: Visual representation of wrinkled (a) and thickened-wrinkled (b) flamelet. Figure from [89].

2.5.2. Turbulent flame speed

From a highly simplified viewpoint the influence of turbulence on premixed combustion can assumed to be the wrinkling of an infinitely thin flame front. In that case the turbulent flame is considered to be a wrinkled laminar flame. In 1940 Damköhler proposed a model based on this assumption using mass conservation [18]:

$$\rho_u S_t A_t = \rho_u S_L A_L \tag{2.34}$$

Where ρ_u is the density of the unburnt mixture, S_t, S_L, A_t and A_l are the turbulent and laminar flame speed, and the turbulent and laminar area of the flame front respectively. Looking at figure 2.10 it can be seen that the turbulent flame speed can be defined as the flame speed a flat flame front should have in order to have the same mass burning rate as the turbulent flame front.

Using equation 2.34 the basic turbulent flame speed relation seen in equation 2.35 can be obtained.

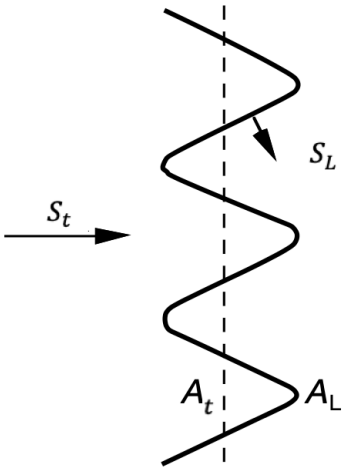

Figure 2.10: Propagation of a premixed flame front into a turbulent mixture. Figure from [84].

$$S_t = S_L \frac{A_L}{A_t} \tag{2.35}$$

Equation 2.35 shows that the ratio of the turbulent and laminar flame areas is the same as the ratio between the respective flame speeds. Meaning that wrinkling of a the flame increases the turbulent flame area and therefore the turbulent flame speed. Damköhler used equation 2.36 to relate the turbulence intensity to the ratio of the turbulent and laminar flame areas. This physical mechanism is taken into account by the vast majority of premixed turbulent combustion models as can be seen later in section 3.2.

$$\frac{A_L}{A_t} = 1 + \frac{u'}{S_L} \tag{2.36}$$

2.6. Flashback mechanisms

Flame flashback is a mechanism in which a flame propagates upstream of the desired anchoring position or holding volume (such as a combustion chamber) of the flame [43]. Flashback tendency is a typical feature of premixed combustion, since a combustible mixture is always available upstream of the desired flame position. Flame flashback can cause damage to components that are not designed for the high flame temperatures. Therefore a good understanding of flame flashback is important when designing equipment for premixed combustion. The different mechanisms causing flashback are core flow flashback, combustion instability induced flashback, combustion induced vortex breakdown and boundary layer flashback as indicated by [51], [67] and [79]. The following provides a short explanation of each flashback mechanism:

- **Core flow flashback:** This instability occurs when the laminar or turbulent flame speed exceeds the flow velocity in the core flow. In industrial combustors core flashback is generally not an issue since the axial flow velocities are usually much higher than the flame speeds [8].
- **Combustion instability induced flashback:** This flashback mechanism occurs due to large amplitude fluctuations in the flow field [43]. The combustion instabilities can be generated by the interaction of acoustic modes, unsteady heat release, and flow structure.
- **Combustion induced vortex breakdown:** This flashback mechanism can occur in swirl stabilized burners [8]. Swirling is a method used to stabilize a flame by creating a re-circulation area in the core flow at the burner inlet. The combustion induced vortex breakdown occurs under certain conditions as a result of the interaction of heat release in the combustion chamber with turbulence in the burner duct. This can lead to the upstream propagation of the re-circulation zone.

- **Boundary Layer Flashback:** Boundary layer flashback is the typical flashback mechanism observed in jet and Bunsen flames [43]. If operating normally the velocity of the incoming premixed mixture is higher than the flame speed meaning that flashback will not occur in the core flow of these burners. But, at the burner wall the flow velocity decreases to zero due to the no-slip boundary condition at the wall. Which results in the formation of a boundary layer. If the local flow velocities drop below the laminar or turbulent flame speed, flashback can be initiated and the flame can propagate upstream.

This study focuses on premixed combustion of methane-hydrogen-air mixtures in Bunsen burners. Furthermore the boundary layer flashback is the flashback mechanism of interest.

2.7. Modeling combustion

In combustion processes, fuel and oxidizer are mixed and burned. This study focuses on combustion of methane-hydrogen-air fuel mixtures. The stoichiometric combustion reactions of hydrogen and methane are seen in equations 2.37 and 2.38 respectively. In subsection 2.2.1 equations governing turbulent flow were presented. To model turbulent combustion, additional equations are needed to take the influence of the combustion reactions into account.

$$\mathrm{H_2} + 0.5\ \mathrm{O_2} + 0.5 * 3.762\mathrm{N_2} \rightarrow \mathrm{H_2O} + 0.5 * 3.762\mathrm{N_2} \tag{2.37}$$

$$\mathrm{CH_4} + 2.0\ \mathrm{O_2} + 2.0 * 3.762\mathrm{N_2} \rightarrow \mathrm{CO_2} + 2.0\ \mathrm{H_2O} + 2.0 * 3.762\mathrm{N_2} \tag{2.38}$$

The equations needed to model turbulent combustion are the transport equations for overall continuity, momentum and scalars to resolve the thermodynamic state of the mixture. The scalar equations should govern the composition of the mixture (e.g. mass or mole fractions) and provide a measure of energy (e.g. internal energy or enthalpy). The governing transport equation for species *i* is seen in equation 2.39 [20]. The net rate of increase of mass of species *i*, $\dot{\omega}_i$, needs modeling. Furthermore D_i is the mass diffusion coefficient of the species. Although not always accurate, this diffusion coefficient is often assumed to be the same for all species in the fuel mixture.

$$\frac{\partial}{\partial t}(\rho Y_i) + \frac{\partial}{\partial x_j}(\rho u_j Y_i) = \frac{\partial}{\partial x_j}\left(\rho D_i \frac{\partial Y_i}{\partial x_j}\right) + \dot{\omega}_i \tag{2.39}$$

Some combustion modeling approaches also require a transport equation specifically for enthalpy, seen in equation 2.40. In this equation κ is the thermal conductivity.

$$\frac{\partial}{\partial t}(\rho h) + \frac{\partial}{\partial x_i}(\rho h u_i) = \frac{\partial}{\partial x_i}\left(\kappa \frac{\partial T}{\partial x_i}\right) + \sum_{i=1}^{N} \frac{\partial}{\partial x_i}\left(h_i \rho D_i \frac{\partial Y_i}{\partial x_i}\right) \tag{2.40}$$

Multiple options for the combustion modeling approach will be further explained in chapter 3.

3

Literature review

CFD modeling of combustion calls for the proper selection and implementation of a model suitable for the representation of the phenomenon associated with the specific combustion process. In this chapter RANS-based turbulent combustion models for the prediction of premixed flame characteristics will be evaluated. It should be noted that a RANS turbulence model was selected, since this would result in the lowest amount of computational time. Since a large amount of calculations was needed to get enough data for a proper comparison with experimental results.

3.1. RANS-based Premixed turbulent combustion modeling

Combustion is a process governed by chemical reactions and mixing. The equations describing a reacting flow differ from the conservation equations describing a non reaction flow [84]. Next to the continuity equation and the conservation of momentum one additionally has to take into account an equation which describes the species conservation and optionally an equation which describes the conservation of enthalpy. A turbulence model such as a RANS turbulence model can be used to account for the enhanced mixing due to the turbulent flow in combination with a turbulent combustion model to account for the turbulence-chemistry interaction describing chemical species conversion and heat release [68].

Combustion models can be categorized based on the way the reaction kinetics are modeled, being infinitely fast chemistry or finite rate chemistry. In which the reactions are assumed to happen infinitely fast or at a finite rate respectively. All combustion models aim at closing the chemical source term, the approach of several closure methods will be discussed. An overview of some combustion models is provided at the end of this section in table 3.1. The models taken into account in this review are: Eddy Dissipation Concept (EDC), Turbulent Flame Speed Closure (TFC), Algebraic Flame Surface Wrinkling (AFSW), Flamelet Generated Manifold (FGM), Level set (G-equation) and the Transported Probability Density Function (PDF).

3.1.1. Direct closure of the chemical source term (Arrhenius)

Although the Arrhenius or laminar finite rate model is inaccurate for turbulent flames due to highly non linear Arrhenius chemical kinetics, [57] it is worth noting the existence of the model since it is the simplest combustion model. The model neglects the effects of turbulence on turbulent combustion.

The reaction rate of the reactions is based on the molecular collisions between the fuel and oxidizer. Instead of neglecting the influence of turbulence like the Arrhenius model, turbulence can also be used as a controlling factor for the reaction rate. As for example in the Eddy Break Up model (EBU) or the Eddy Dissipation Concept (EDC) model, which will be treated in the next subsection.

3.1.2. Eddy Dissipation Concept (EDC)

The Eddy Dissipation Concept [56] has evolved from the Eddy Dissipation Model (EDM) with the aim of including detailed chemical mechanisms in turbulent flows. The concept is mainly based on the assumption that reactions occur within small turbulent structures which are called the fine scales [9],

i.e. in the flamelet regime in the Borghi diagram. When the time scale of the mixing process due to turbulence is similar to the characteristic time scale of the reaction rate, the reaction rate is assumed to be dominated by the turbulent properties of the flow. Therefore the reaction rate is a function of the turbulent kinetic energy k and the dissipation rate ϵ as seen in equations 3.2, 3.3 and 3.4 for the source term, fraction occupied by the fine structures and time scale of reaction for the species in the fine structures respectively [35]. It should be noted that the EDC approach requires a high computational capability when combined with a detailed chemical reaction mechanism.

The transport equation for species *i* is given by equation 3.1. In which R_i is the net rate of production of species *i* by chemical reaction and S_i is the rate of creation by addition from the dispersed phase and the defined source. D_i is the diffusion flux of the species.

$$\frac{\partial}{\partial t}(\rho Y_i) + \frac{\partial}{\partial x_j}(\rho u_j Y_i) = -\frac{\partial}{\partial x_j}(D_{i,j}) + R_i + S_i \tag{3.1}$$

The source term (reaction rate) in the conservation equation for the mean species *i* is given by equation 3.2. In which the fine scale species mass fraction is given by Y_i^* after reaction time τ^*.

$$R_i = \frac{\rho * (\xi^*)^2}{\tau^*[1-(\xi^*)^3]}(Y_i^* - Y_i) \tag{3.2}$$

$$\xi^* = C_\xi \left(\frac{\nu\epsilon}{k^2}\right)^{\frac{1}{4}}, C_\xi = 2.1377 \tag{3.3}$$

$$\tau^* = C_\tau \left(\frac{\nu}{\epsilon}\right)^{\frac{1}{2}}, C_\tau = 0.4082 \tag{3.4}$$

Various results obtained by means of the EDC model can be found in the literature. Two examples of such studies and the authors their opinion on the performance of the EDC model are the study by Nanduri, Parsons, Yilmaz, Celik and Strakey [61] and the study by Tabet, Sarh, Birouk and Gokälp [76].

Nanduri, Parsons, Yilmaz, Celik and Strakey [61] applied the EDC model in combination with both a RSM and a RNG $k-\epsilon$ turbulence model to assess the prediction of emission from lean premixed combustion of methane. The setup to study the flames is a lean premixed, confined, bluff body-stabilized combustor. They found both models to overpredict the temperature. However they observed that the RNG $k-\epsilon$ model appears to out perform the RSM turbulence model in the prediction of temperature at all axial locations. Although the RNG $k-\epsilon$ still overpredicts the temperature, the error is significantly smaller than the RSM turbulence model. Furthermore they found that neither the RSM nor the RNG $k-\epsilon$ turbulence model could capture the measured root mean square velocity profiles either qualitatively or quantitatively.

Tabet, Sarh, Birouk and Gokälp [76] applied the EDC model in combination with a RSM (Reynolds Stress Model) turbulence model on a turbulent non premixed hydrogen-air flame to assess the prediction of mixing and air entrainment in the near-field region of the flame. Their results showed that the model is inapproapriate to describe mixing in the near-field region of this flame and that the integral turbulence time scale is slightly underpredicted. They stated that overall, predictions of species, and flame temperatures are in reasonable agreement with experimental data. However the model tends to overpredict mixing in the near-field region while in the far-field region estimation agrees reasonably well with experimental data.

3.1.3. Flamelet (topological) models

A flamelet is the thin region between the burnt and unburned gases. The concept of the model is based on the assumption that the reaction zones retain their structure and are not influenced by turbulence. This assumption can only be valid if the thickness of the reaction zone is sufficiently small compared to the Kolmogorov length scale. [68] In case of intense turbulence the Kolmogorov eddies become sufficiently small to penetrate the reaction zone. The model assumes that all chemical reactions are faster than the smallest turbulent time scale or *Ka* smaller than unity. Therefore the chemical reactions happen on a thin layer which can be seen as the flame front. One basic effect of turbulence in turbulent premixed combustion is flame wrinkling due to the fluctuating velocity field. In the flamelet theory, valid

in the flamelet regime in the Borghi diagram, this effect is described by the flame surface density. This quantity conveys most of the effects of the turbulence on the rate of energy release and can be obtained through various methods. First the concept of the progress variable and the flame surface density will be explained, thereafter several methods based on the flamelet assumption are evaluated.

Progress variable and Flame surface density
Following the assumption of a thin reaction zone, a turbulent premixed can be described based on the following assumptions: in an adiabatic case the state of the mixture in a premixed flame can be characterized with a single combustion progress variable *c* and in the case of a non-adiabatic case the mixture can be characterized by two variables, the progress variable *c* and the enthalpy *h*. The transport equations of the progress variable and the enthalpy are seen in equation 3.6 and 2.40 respectively. The progress variable is also referred to as the reduced temperature. This progress variable describes a two state system, showing either the 'unburned state' or a 'burned state' with all main species and temperature corresponding to the unburned or burned mixture species and temperature respectively. The assumption concerning the progress variable can be justified by invoking one of the following three chemistry approximations: single-step chemistry and equidiffusive mixture, flamelet combustion regime in the Borghi diagram or two-fluid flow [20]. For the remainder of this section the single step chemistry will be assumed (the same result can be obtained for the flamelet approximation). The model for the average location of the reaction zone describes the probability of finding the burned gas state. This probability is described by the progress variable, which can be defined using a mass fraction or the temperature as seen in equation 3.5. In which Y_F denotes the fuel mass fraction and the subscripts *u* and *b* denote unburned and burned mixture quantities. The progress variable can only be expressed as a ratio of temperatures under the assumptions of adiabatic flames and constant specific heat C_p of the mixture.

$$c = \frac{Y_F - Y_{F,u}}{Y_{F,b} - Y_{F,u}} = \frac{T - T_u}{T_b - T_u} \tag{3.5}$$

By definition *c* = 0 in the unburned gas and *c* = 1 in the burned gas. A transport equation for the progress variable can be derived from the relevant transport equations for species mass fraction. The transport equation for the progress variable, which is the transport equation used in ANSYS Fluent for this study, is seen in equation 3.6. Where D is the diffusion coefficient.

$$\frac{\partial}{\partial t}(\rho c) + \frac{\partial}{\partial x_i}(\rho u_i c) = \frac{\partial}{\partial x_i}\left(\rho D \frac{\partial c}{\partial x_i}\right) + \dot{\omega}_c \tag{3.6}$$

The Favre-averaged transport equation for the progress variable is given by:

$$\frac{\partial}{\partial t}(\overline{\rho}\tilde{c}) + \frac{\partial}{\partial x_i}(\overline{\rho}\tilde{u}_i\tilde{c}) = \frac{\partial}{\partial x_i}\left(\overline{\rho D \frac{\partial c}{\partial x_i}}\right) - \frac{\partial}{\partial x_i}\overline{\rho u_i'' c''} + \overline{\dot{\omega}_c} \tag{3.7}$$

After applying Favre-averaging to equation 3.6 and the balance equations for mass, momentum and enthalpy. Assuming the molecular transport term is neglected (first term on right hand side of equation 3.7), three unclosed terms requiring modeling remain, being: the turbulent stress tensor, the mean reaction rate, and the turbulent scalar transport term (second term on right hand side of equation 3.7) consisting of the species and enthalpy turbulent fluxes. The turbulent stress tensor is modelled using a turbulence model, the turbulent scalar transport is usually modelled using a gradient assumption. When using a flame surface density model the mean reaction rate is modelled as seen in equation 3.8 [27]. In which S_L^0 is the unstretched laminar flame speed, G is the flame stretch factor which was shortly explained in subsection 2.4.2 and Σ is the flame surface density, which can be seen as the flame surface per unit volume. To close the mean reaction rate term the flame surface density must be modelled, which will be explained in the following subsection. The approaches to model the source term based on the flamelet assumption are discussed in the sections 3.1.4, 3.1.5, 3.1.6 and 3.1.7.

$$\dot{\omega}_c = \rho_u S_L^0 G \Sigma \tag{3.8}$$

3.1.4. Turbulent Flame Speed Closure (TFC); Zimont

The TFC model described here is known as the Zimont Turbulent Flame Speed Closure model [88]. In the Turbulent Flame Speed Closure model the flame surface density can be expressed by using the

gradient of the progress variable in combination with flame surface wrinkling ratio as seen in equation 3.9, in which A_t is the turbulent flame surface area and $\bar{A}$ is the projected mean flame surface area. In combination with a relation for the turbulent flame speed seen in equation 3.10.

$$\Sigma = \frac{A_T}{\bar{A}} |\nabla \tilde{c}| \tag{3.9}$$

In which $\tilde{c}$ indicates the Favre-averaged progress variable.

$$S_t \approx S_L^0 \frac{A_T}{\bar{A}} \tag{3.10}$$

Combining the above equations gives the mean reaction rate seen in equation 3.11. In this equation the effect of flame stretch is neglected. To take this flame stretching into account, the mean reaction rate can be multiplied by a stretch factor.

$$\dot{\omega}_c = \rho_u S_t |\nabla \tilde{c}| \tag{3.11}$$

Zimont developed an expression to model the turbulent flame speed seen in the following equation. In which l_t is integral length scale, u' is root mean square of the velocity fluctuations at the same length scale and α is the molecular thermal diffusivity.

$$S_t = 0.52 {u'}^{3/4} S_L^{0\,1/2} l_t^{1/4} \alpha^{-1/2} \tag{3.12}$$

The constant 0.52 is a single model constant and equation 3.12 was derived under several constraints, being $\mathrm{Re}_t >> 1$, *Da* >> 1, *Ka* > 1 and a constraint concerning the flame-development time [20]. The turbulent Reynolds number is defined as $\mathrm{Re}_t = u' l_t / \nu$.

Dinkelacker and Hölzler [21] validated the model by comparing numerical results, based on a standard $k-\epsilon$ turbulence model with experimental data from a turbulent premixed V-shaped flame stabilized on a wire above the burner exit. The conditions of the turbulent flow and of the chemical processes have separately been varied. The validated flames have Damköhler numbers between 2 and 70 and Karlovitz numbers between 0.1 and 4.6, indicating a range wider than the originally specified constraints. The comparison between experimental data and numerical results shows that for the different flow rates and equivalence ratios the calculated flame location corresponds to the location determined by experiments. They also concluded that regarding the simple structure of this model, it is found to predict the shape and width sufficiently well. Although they concluded the model is too simple for a quantitative agreement.

3.1.5. Algebraic Flame Surface Winkling (AFSW), part 1

AFSW model is an extension of the TFC model, developed by Dinkelacker and Muppala [58]. The difference between the models can be seen by expressing the reaction rate as seen in equation 3.13.

$$\dot{\omega}_c = \rho_u S_L^0 \left(\frac{A_T}{\bar{A}} \right) |\nabla \tilde{c}| \tag{3.13}$$

The difference between the TFC and AFSW model is that instead of using the relation described in equation 3.10 a different algebraic relation is used for the flame surface wrinkling ratio:

$$\frac{A_T}{\bar{A}} = 1 + \frac{0.46}{Le} \mathrm{Re}_t^{0.25} \left(\frac{u'}{S_L^0} \right)^{0.3} \left(\frac{p}{p_0} \right)^{0.2} \tag{3.14}$$

In which *Le* is the Lewis number and p/p_0 is a pressure dependency with p_0 equal to 1 bar. In contrast to the TFC model described in the previous section, the AFSW model does include the flame stretch effect in the flame wrinkling ratio relation.

Dinkelacker, Manickam and Muppala [22] further improved the AFSW model by applying an effective Lewis number approach to hydrogen/methane mixtures. Although highly turbulent flames are thought to be dominated by turbulent mixing instead of molecular transport. Dinkelacker et al. indicated that recent work on reaction modeling of turbulent lean premixed combustion has shown, that if different

fuels and varied pressure are regarded the Lewis number poses significant influence even at high turbulence intensities. Therefore they proposed a model for an effective Lewis number approach seen in equation 3.15. In which Le^* is the effective Lewis number and x_i being the volumetric fractions of the fuel mixture. The complete derivation of the model can be found in their paper.

$$\frac{1}{Le^*} = \frac{x_{CH_4}}{Le_{CH_4}} + \frac{x_{H_2}}{Le_{H_2}} \tag{3.15}$$

They concluded that their model in combination with a standard $k-\epsilon$ turbulence model shows a very good agreement of flame length data when compared to experimental data for turbulent pressurized Bunsen flames and highly turbulent pressurized dump combustor flames with hydrogen content of the fuel up to 20 volumetric percent. Despite the fact that the model even shows a rather good agreement for 30% and 40% hydrogen it is concluded that the limit of the model is reached at about 20% or 30% hydrogen added to methane.

This model will be further explained in subsection 3.2.1. Furthermore the authors their conclusion will also be viewed based on the results they have presented in their work.

3.1.6. Flamelet Generated Manifold (FGM)

The FGM model is a tabulated chemistry method [80]. The model can be seen as a combination of a manifold, such as Intrinsic Low-Dimensional Manifolds (ILDM) [55] and a flamelet approach [65]. It follows the idea that the turbulent flame can be viewed as an ensemble of small laminar flame elements. The FGM method uses a chemical library based on one-dimensional unstretched premixed flames to model the chemistry of a multi-dimensional flame and to construct a manifold. The concept used by the model is very similar to a steady flamelet model since it assumes local flame conditions can be obtained from pre calculated laminar flames. However the difference is that the FGM not only uses a flamelet to determine the scalar composition, but the chemical source term for the progress variable as well. The model is incorporated in a flow solver by solving the transport equations for the control variables together with the momentum and continuity equations. These control variables are usually chosen as the progress variable c and the mixture fraction Z. The interaction between chemistry and turbulence is taken into account by a joint probability density function (PDF) for the mixture fraction and the progress variable [71]. Usually The joint PDF is created by assuming that the the mixture fraction and progress variable are statistically independent which means the joint PDF can be written as a product of the presumed PDFs of the variables. The Favre-averaged values of the thermo-chemical variables are obtained by integrating the relationships over *Z* and *c*, using presumed probability density Beta functions [9]:

$$\tilde{\phi} = \iint \phi(Z,c)\beta(Z;\tilde{Z},\widetilde{Z''^2})\beta(C;\tilde{C},\widetilde{C''^2})\,dZ\,dc \tag{3.16}$$

Albrecht, Zahirovic, Bastiaans, Oijen and de Goey [2] applied the FGM model in combination with a RANS turbulence model to first validate a Sandia Flame D diffustion flame and second to a biomass combustion grate furnace. They compared the FGM model with the EDC model, discussed in section 3.1.2. The authors state that the two models predict similar results, however the FGM model reduces the calculation time from weeks to hours.

Van Oijen, Donini, Bastiaans, ten Thije Boonkkamp and de Goey [81] have reviewed the current state-of-the-art of FGM for the modeling of premixed and partially-premixed flames. They validated the FGM approach in combination different turbulence models based on several test cases. It is stated that results obtained with a LES turbulence model a have superior accuracy compared to results obtained with a RANS turbulence model.

3.1.7. Level set approach (G-equation)

Another method based on the flamelet assumptions is the level set method using the G-equation. This approach is mathematically similar to a flame surface density approach, however it differs in the introduced assumptions and the closure developments. The method assumes the flame front to be a geometrical entity, which separates the domain into burnt and unburnt regions. When using a RANS turbulence model the flame brush is described as a surface propagating with a turbulent flame speed s_T. The turbulent flame is then identified as an isosurface G^* of the non-reacting scalar *G*. The transport

equation for the variable *G* is called the G-equation. After applying Favre-averaging the G-equation is given by equation 3.17 [44]. When compared to the transport equation for the progress variable it can be seen that the G-equation does not include a term for molecular diffusion.

$$\bar{\rho}\frac{\partial G}{\partial t} + \bar{\rho}\tilde{u}_i\frac{\partial G}{\partial x_i} = \rho_u s_T|\nabla G| \tag{3.17}$$

Herrmann [36] proposed an extension to the level set flamelet model for premixed turbulent combustion that takes the effects of ambient air entrainment into account. The inner structure of the instantaneous flame front is accounted for by using an approach based on a presumed pdf of laminar flamelets. The level set model is used in combination with a standard $k-\epsilon$ turbulence model and applied to three turbulent Bunsen flames, only differing by Reynolds number. The predicted simulation results are compared to measurements of the corresponding flames and showed good overall agreement. However several discrepancies occur especially concerning temperature. The comparison of the computed gradient in the radial temperature distribution shows an overprediction for all three flames. Which indicates an underpredicted turbulent flame brush thickness in the simulation. A reason for the observed discrepancies between simulation and measurements given by the author is the employed turbulence model in combination with the uncertainty in the turbulent inflow boundary conditions. A solution proposed for this problem, is a coupling with a more advanced turbulence models e.g. Large Eddy Simulation (LES).

3.1.8. Transported PDF

The transported PDF method applies a different approach to model the chemical source term. The main advantage of the transported probability density function method is that the chemistry can be treated exactly [84]. The method works by finding a solution for the PDF transport equation. A transport equation describing the time dependent PDF behaviour can be derived from the basic transport equations [69]. The joint scalar PDF is usually represented by a an ensemble of particles also known as notional particles. The time evolution of the particles is described by convection, chemical reaction, molecular transport and body forces. Therefore the evolution of the particles follows the same evolution as the PDF. When using a transported PDF approach in combination with a RANS turbulence model the joint PDF for scalars (e.g. temperature or density) and velocity known as the velocity-composition joint PDF is usually reduced to a PDF for scalars known as the composition joint PDF and the velocity is computed using the RANS turbulence model. This does produce less accurate results, but simplifies the transport equation. The joint composition PDF equation is given by equation 3.18. In which f_ϕ is the Favre averaged joint PDF. S_k is the reaction rate for species k, ψ is the composition space vector, u_i'' is the fluid velocity fluctuation vector and $J_{i,k}$ is the molecular diffusion flux vector.

$$\frac{\partial}{\partial t}(\rho f_\phi) + \frac{\partial}{\partial x_i}(\rho u_i f_\phi) + \frac{\partial}{\partial \psi_k}(\rho S_k f_\phi) = -\frac{\partial}{\partial x_i}\left[\rho\langle u_i''|\psi\rangle f_\phi\right] + \frac{\partial}{\partial \psi_k}\left[\rho\langle\frac{1}{\rho}\frac{\partial J_{i,k}}{\partial x_i}|\psi\rangle f_\phi\right] \tag{3.18}$$

The transported PDF method does need closure models for the molecular mixing term. The combustion and turbulence models are coupled using the density ρ. The PDF model generates a density field, which is used by the turbulence model to calculate a flow field. The newly calculated flow field returns information to the PDF, thereafter the iteration is repeated until convergence is reached.

Lindstedt and Vaos [53] applied the transported PDF approach with a different closure approach being a closure at the joint composition–enthalpy level. They applied the model to a number of premixed turbulent flames with different Reynolds numbers. The study investigates the effects of variations in the time-scale ratio. Also the effect of heat losses to the burner is evaluated. Furthermore the impact of an extended algebraic relationship for the scalar dissipation rate accounting for small-scale properties has been evaluated. Comparison with experiments show that the extended scalar dissipation-rate closure and the modified Curl's model which accounts for the molecular mixing term produce turbulent flame speeds which are in close agreement with measurements. The authors state that the study indicates that a closure at the joint scalar level combined with comprehensive chemistry has the potential to reproduce the detailed chemical structure of premixed turbulent flames.

3.1.9. Conclusion on combustion models

Several combustion models have been evaluated, with the focus of applying the models in combination with a RANS turbulence model. The evaluated models are: the Eddy Dissipation Concept (EDC), Turbulent Flame Speed Closure (TFC), Algebraic Flame Surface Wrinkling (AFSW), Flamelet Generated Manifold (FGM), Level set (G-equation) and the Transported Probability Density Function (PDF). In table 3.1 an overview is provided of the evaluated models and also other models encountered in literature. The models are subdivided in models either applicable to both premixed and non-premixed combustion or only premixed or non-premixed. The models are assessed based on three characteristics: possibility to include detailed chemistry, possibility to include effects of differential diffusion in the mean equations or in the mean reaction rate and finally the possibility to take into account the effect of turbulent fluctuations (i.e. flame stretch effects) on the mean reaction rate.

Based on the literature review multiple conclusion can be drawn. Firstly, if the scope of the numerical model is to provide qualitative results of the flame shape and location, the TFC and AFSW models seem to deliver satisfactory results. However it should be noted this does not automatically implicate the same for predicting flame instabilities, since the studies presented in literature did not focus specifically on predicting flame instabilities. Secondly, the FGM and Level set (G-equation) approach could provide more quantitative results. However literature indicates both models perform better when coupled with a more advanced turbulence model such as LES [36], [81]. Therefore when choosing one of the aforementioned models one should consider switching to a more sophisticated turbulence model. Furthermore literature indicates that FGM can produce results similar to EDC but with drastically lower calculation times. And finally, within the RANS turbulence framework the Transported PDF approach seems to deliver the most promising results.

Even so, one should keep in mind that even though the mentioned approaches are based on different concepts, they are closely related as can be seen from the explicated relations by Veynante and Vervisch [83]. Which does not mean any of the approaches have a decisive advantage over others. The results will mainly depend on the closure of the unclosed terms.

Both premixed and non-premixed	**Detailed chemistry**	**Differential diffusion**	**Turbulent fluctuations**
Laminar reaction rates	Yes	In mean equations	Not included
Eddy Dissipation Model (EDM)	One step only	In mean equations	Not included (overall scaling)
Eddy Dissipation Concept (EDC)	Yes	In mean equations	Not included (overall scaling)
Flamelet Generated Manifold (FGM)	Yes	Yes, in flamelets	Yes, via PDF(Z,c)
Transported PDF (particle method)	Yes (costly)	Not standard	Fully represented
Transported PDF (stochastic field method)	Yes (costly)	Not standard	Fully represented
Conditional Moment Closure (CMC)	Yes	Yes	Yes, via conditional moments and PDF(Z)
Premixed only			
Progress variable	No	No	Yes, via PDF(c)
Flame Surface Density (FSD)	No	No	Yes, via flame stretch factor and FSD equation
Turbulent Flame speed Closure (TFC)	No	No	Yes, via turbulent flame speed correlation
Algebraic Flame Surface Wrinkling (AFSW)	No	Via Lewis number dependency	Yes, via flame area correlation
Level set approach (G-equation)	No	No	Yes, via turbulent flame speed correlation
Non-premixed only			
Mixture fraction + equilibrium	No	No	Yes, via PDF(Z)
Mixture fraction + flamelets	Yes	Yes, in real space flamelets	Yes, via PDF(z,χ)

Table 3.1: Combustion modeling approaches overview

3.2. Turbulent flame speed

As described in section 3.1.4 the source term in the Favre-averaged transport equation for the progress variable can be closed by modeling the turbulent flame speed. Besides the Zimont Turbulent Flame Speed Closure model other possibilities exist to model the turbulent flame speed. In this section options for the turbulent flame speed, provided in literature, that have the potential to work better than the Zimont correlation when hydrogen is used as fuel will be evaluated.

3.2.1. Algebraic Flame Surface Winkling (AFSW), part 2

One relation which can be used to model the turbulent flame speed has already been described in section 3.1.5. The development of this model is elaborated in [58]. The flame surface wrinkling ratio is modelled with an algebraic parameterized relation. It is stated that studies such as [59] and the similarity to turbulent flame speed relations indicate that an approach with three empirical parameters may be applicable:

$$\frac{A_T}{\overline{A}} = 1 + a\mathrm{Re}_t^{0.25}\left(\frac{u'}{S_L^0}\right)^b\left(\frac{p}{p_0}\right)^c \tag{3.19}$$

In order to determine the fit parameters a,b and c, a numerical optimization study was performed by Muppala et al. [58]. They calculated and measured flame angles of 101 different Bunsen-type flames for lean methane/air, ethylene/air and propane/air mixtures were compared for operating pressure ranging from 0.1 to 1.0 MPa and inflow conditions consisting of an equivalence ratio range of 0.5 to 0.9 and u'/S_L^0 values approximately between 1 and 5.5. They found that for all the fuels investigated this relation collapses to a unique equation, in which the Lewis number of the fuel/air mixture is included. This equation is seen in equation 3.14, together with equation 3.15 this forms the AFSW model. Although the model is based on the aforementioned 101 Bunsen flames, the model is fairly successful at modeling lean premixed turbulent methane/hydrogen/air flames. In [22] it is stated that for up to 20 vol.% hydrogen a comparison of the flame length data between experiments and the model shows a very good agreement. A rather good agreement is shown for flames with hydrogen content of the fuel up to 40 vol.%. As discussed earlier in section 3.1.5 it is concluded that the limit of the model is reached at about 20% or 30% hydrogen added to methane.

Despite this conclusion Muppala, Manickam and Dinkelacker [60] used the AFSW model in more recent work, where they modified the Lewis number term as seen in equation 3.20. Besides a case with pure methane/air they specifically focus on flames with 40 to 100 vol.% hydrogen. They state that their proposed reaction model with the incorporation of an effective Lewis number of the fuel mixture is found to work rather well.

$$\frac{S_t}{S_L^0} = 1 + \frac{0.46}{exp\left(Le_{eff} - 1\right)}\mathrm{Re}_t^{0.25}\left(\frac{u'}{S_L^0}\right)^{0.3}\left(\frac{p}{p_0}\right)^{0.2} \tag{3.20}$$

However a further evaluation of the claim that their proposed model works rather well does leave room for debate. For example results are shown of a reacting flow field, see figure 3.1. The figure shows normalized mean axial flow velocities along the middle axis for 40, 60, 80 and 100 vol.% hydrogen enriched methane flames. Experimental results are compared with the AFSW model with an effective Lewis number approach, and another combustion model being the tLV model ('tuned' Lindstedt-Váos), for more information on this model see [57]. And although the proposed model predicts results which are closer to the experimental results, the predictions clearly do not match the experimental results and there is definitely room for improvement.

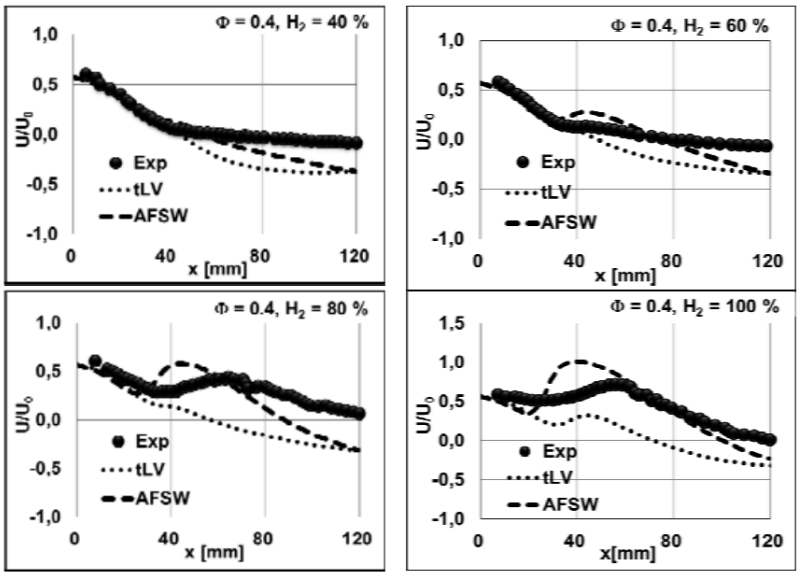

Figure 3.1: Experimental data of normalized mean axial flow velocities along the middle axis for 40, 60, 80 and 100 vol.% hydrogen enriched methane flames compared to results produced with AFSW and tLV combustion models, image from [60].

3.2.2. Turbulent flame speed for syngas

The next method of modeling the turbulent flame speed is a correlation found in the work of Daniele, Jansohn, Mantzaras and Boulouchos [19]. The article focusses on describing turbulent combustion characteristics and in particular turbulent flame speeds for a variety of premixed syngas based fuel mixtures at gas turbine like conditions. The fuel mixtures used are pure methane/air, methane/hydrogen/air and various syngas compositions. The fuel with the highest vol.% hydrogen contains 67 vol.%. The equivalence ratios range from 0.25 to 0.75. Furthermore the gas turbine like conditions implicate much higher values of u'/S_L^0, which exceed 100 and temperatures up to 773 K. Pressure ranges from 0.1 MPa up to 2.0 MPa. The database of measured operating conditions is seen in figure 3.2. The provided correlation for the turbulent flame speed is seen in equation 3.21 and corresponds to the dashed line in the figure.

$$\frac{S_t}{S_L} = a\left(\frac{u'}{S_L}\right)^{0.63}\left(\frac{l_t}{\delta_L}\right)^{-0.37}\left(\frac{p}{p_0}\right)^{0.63}\left(\frac{T}{T_0}\right)^{-0.63} \tag{3.21}$$

In which a = 337.5, S_L is the laminar flame speed, δ_L is the laminar flame thickness p/p_0, and T/T_0 account for pressure and inlet temperature variation p_0 equal to 0.01 MPa and 1 K respectively. The authors state that the correlation captures effects of differential diffusion and hydrodynamic instabilities and is valid for all the investigated fuel mixtures. Taking into account the wide range of operating conditions and fuel mixtures for which the correlation has been derived it seems a rather good fit. However when modeling fewer fuel mixtures and a smaller range of operating conditions, a correlation focused more on the specific application will probably perform better.

3.2.3. Turbulent flame speed for hydrogen rich fuel

In the work of Lin, Jansohn and Boulouchos [52] several correlations for the turbulent flame speed of hydrogen rich fuel gases are presented. Similar to the work described in section 3.2.2 the focus lies on gas turbine relevant conditions. Meaning the fuel is preheated up to 623 K and pressurized up to 2.0 MPa, the equivalence ratios range from 0.26 to 0.54. Based on their acquired data for the hydrogen rich fuel gases; hydrogen/nitrogen, pure hydrogen and syngas, correlations are derived to provide an overview on the characteristics of the turbulent flame speeds. The work focuses on turbine relevant conditions (i.e. high pressures and high turbulence intensities). Two correlations are presented, one for the fast chemistry regime (equation 3.22) and one for the slow chemistry regime (equation 3.23) with a Damköhler number greater than 1 and smaller than 1 respectively.

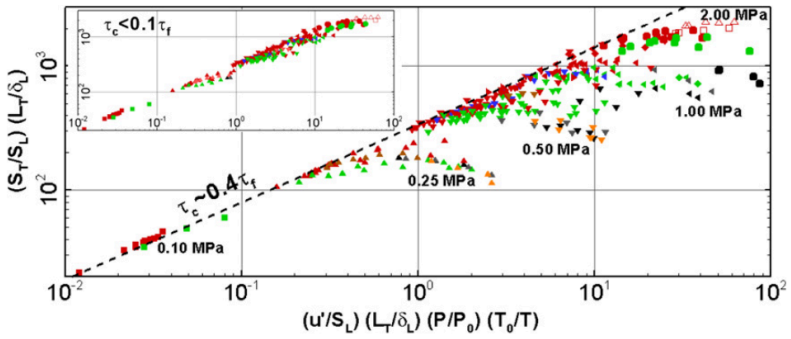

Figure 3.2: Normalized turbulent flame speed data, τ_f is the integral turbulent time scale and τ_c is the time necessary for the flame front to travel through the flame brush thickness. Figure from [19].

$$\frac{S_t}{S_L^0} = 0.8 Le_{eff}^{-1.38} \left(u'/S_L^0\right)^{0.67} \mathrm{Re}_t^{0.13} \tag{3.22}$$

$$\frac{S_t}{S_L^0} = 4.6 Le_{eff}^{-1.84} \left(l_t/\delta\right)^{-0.08} Ka^{0.4} \tag{3.23}$$

In which Le_{eff} is the effective Lewis number. Furthermore a 'global' correlation for S_t/S_L^0 is presented:

$$\frac{S_t}{S_L^0} = 10.5 Le_{eff}^{-0.82} \left(u'/S_L^0\right)^{0.45} \left(\frac{l_t}{\delta_L}\right)^{-0.41} \left(\frac{p}{p_0}\right)^{0.75} \left(\frac{T}{T_0}\right)^{-1.33} \tag{3.24}$$

In figure 3.3, S_t/S_L^0 predicted by equation 3.24 (5) is plotted against the measured $S_t/S_L^0$for selected H2-rich and syngas flames. The predictions are obtained by entering flow data measured at c = 0.05 into equation 3.24. An error range of approximately 20 % from the measured S_t/S_L^0 is indicated by red dashed lines. The turbulent flame speed of both hydrogen rich and syngas flames seem to be well described the proposed correlation. However once again it should be noted that if the focus is on modeling a smaller range of operating conditions, a correlation focused more on the specific operating conditions will probably perform better.

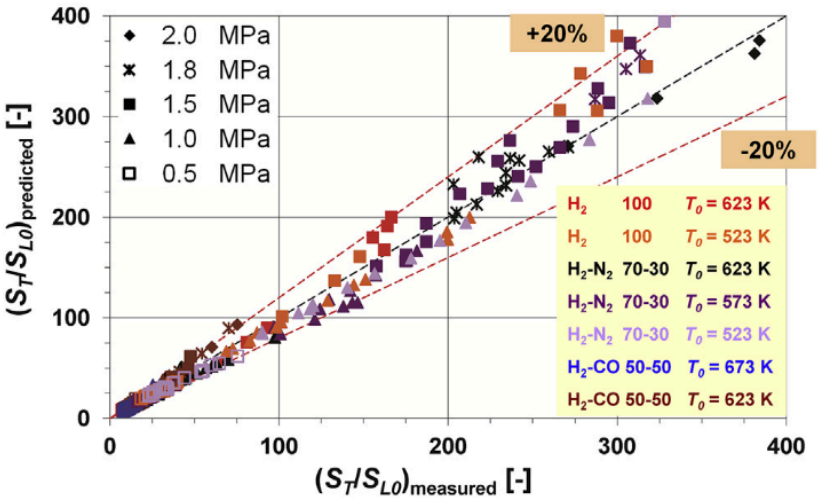

Figure 3.3: Experimental S_t/S_L^0 for selected H2-rich and syngas flames compared to S_t/S_L^0 at c = 0.05 predicted by the turbulent flame speed correlation seen in equation 3.24. Predictions are obtained by entering flow data measured at c = 0.05 into the turbulent flame speed correlation. Figure from [52].

3.2.4. Turbulent flame speed for methane/hydrogen/air flames

The study presented by Cai et al. [16] reports the turbulent flame speed for turbulent expanding flames of methane/hydrogen/air mixtures with methane/hydrogen ratios from 20 up to 80 vol.% hydrogen. For a wide range of turbulence intensities and equivalence ratios from 0.4 up to 1. The u'/S_L^0 values seen approximately are between 0.1 and 30. All the experiments are performed at an initial temperature of 298K and a pressure of 0.1 MPa The study demonstrates the role of differential diffusion, which is characterized by the effective Lewis number, on flame propagation even for intense turbulence.

A correlation for the turbulent flame speed at the location where the progress variable is equal to 0.5, based on experimental data and general correlations of Bradley et al. [14] and Kitagawa et al. [45] is presented. The general correlations are valid for mixtures with Lewis number both greater and smaller than unity. However, the study aims at seeking a power-law correlation which also considers the self-similar propagation during flame expansion and differential diffusion effects. The correlation proposed is seen in equation 3.25.

$$\frac{S_{t,c=0.5}}{S_L} = 1 + 0.164\left(Re_{T,f}Le_{eff}^{-2}\right)^{0.66} \tag{3.25}$$

Le_{eff} is the effective Lewis number. The fuel Lewis number is calculated based on a volumetric fraction weighted average of the Lewis numbers of methane and hydrogen as proposed in [13]. The overall effective Lewis number, Le_{eff}, is determined while taking the influence of the excess and deficient reactants in consideration (i.e. for a lean mixture: excess reactant is the oxidizer and deficient reactant is the fuel) , as suggested in [1]. And $Re_{T,f}$ is the turbulent flame Reynolds number, which is defined based on the averaged flame radius and the thermal diffusivity. It differs from the turbulent Reynolds number, which keeps constant in the propagation event. In case of a non-expanding flame the classical turbulent Reynolds number can be used.

The authors state that the correlation is able to predict not only the experimental data presented. But also the turbulent flame speeds measured using turbulent Bunsen flames and expanding flames at high pressures. Their statement is reinforced by comparing their correlation with experimental data. The results of the comparison of their correlation with their data can be seen in figure 3.4 where the S_t/S_L^0 is plotted against Re_t/Le_{eff}^2. Furthermore their correlation is also compared to previous data of turbulent Bunsen flames from Kobayashi et al. [46], [47] and turbulent expanding flames from Nguyen et al. [62] and Kitagawa et al. [45] seen in figure 3.5. It is seen that the experimental data collapses well onto the proposed correlation.

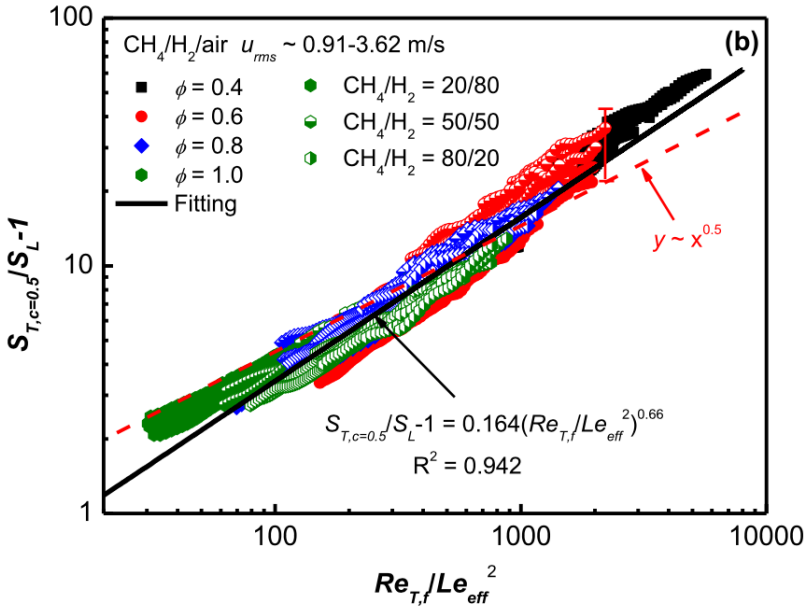

Figure 3.4: Experimental data compared to correlation presented by Cai et al. [16].

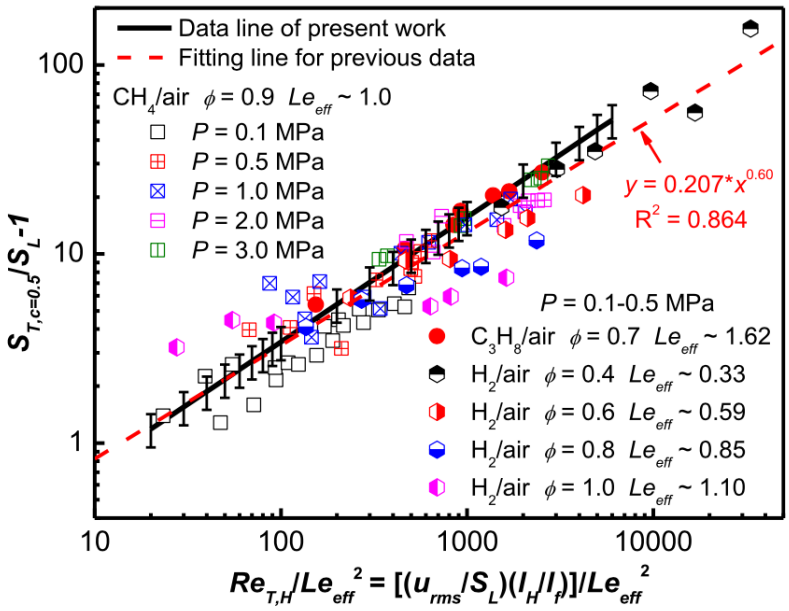

Figure 3.5: Previous experimental data compared to correlation presented by Cai et al. [16].

It is noted by the authors that the Le^{-1} dependence of the turbulent flame speed has been suggested in previous experimental and numerical studies, such as the work of Dinkelacker presented in sections 3.1.5 and 3.2.1. It is stated that these studies further inspire the confidence in their correlation for the turbulent flame speed which is also based on a near Le^{-1} dependence.

3.2.5. Remarks on selecting turbulent flame speed correlations

Driscoll [25] evaluates the effect of flamelet structure on turbulent flame speed. He states that for a model to be considered to be robust, it is not enough to demonstrate that by changing certain parameters the expected flame speeds match an experiment. A robust simulation should also correctly predict parameters such as Σ and δ as well as S_t. Furthermore he states that experiments indicate that flamelet wrinkling is geometry dependent. Which has as a results that models must be able to simulate wrinkling with differential equations and not rely on empirical correlations. In contrary to empirical correlations, differential equations can account for the wrinkling that occurred upstream. Also he reports a relation for the turbulent flame speed presented in [32]. It is made clear that the difficulty of fitting a turbulent flame speed relation on experimental results lies mostly in the non linear relation between the turbulent flame speed and u'/S_L^0 for values larger than the relatively large values 4-8.

Lipatnikov and Chomiak [54] discuss the effect of the Lewis number on the turbulent flame speed. A discussion on experimental data shows the drastic effect of the Lewis number on turbulent flame speed. They emphasize the important role played by highly perturbed flamelets in premixed turbulent combustion. They discuss the lack of a straightforward correlation for the slope of $S_t(u')$, which implies that the increase in burning velocity by moderate turbulence and flame quenching by strong turbulence are controlled by different mechanisms. It is stated that the effects of the Lewis number on the turbulent flame speed can be very strong.

When selecting a turbulent flame speed correlation one should consider the viewpoint of the authors that presented the specific turbulent flame speed correlation. A correlation can be based on experimental data and aims to be used to predict turbulent flame speeds based on flow values measured at a single point e.g. progress variable equal to 0.05. Another possibility is that a correlation is derived specifically for the use in CFD. Of the turbulent flame speed correlations in this chapter, only the correlations by Zimont (see subsection 3.1.4) and Dinkelacker et al. (see subsections 3.1.5 and 3.2.1) have been derived by the authors for direct use in CFD. The other three correlations presented by Daniele et al. (see subsection 3.2.2), Lin et al. (see subsection3.2.3) and Cai et al. (see subsection3.2.4) were based on experimental data and not optimized for use in CFD.

3.2.6. Conclusion on the comparison of different turbulent flame speed correlations

Various approaches to model the turbulent flame speed have been evaluated. Additionally a few effects on the turbulent flame speed mentioned in literature were briefly discussed. Based on the literature review and the theory on flame stretch (see subsection2.4.2) and flame front instabilities (see subsection 2.4.2) it has become clear that the Lewis number potentially has a great influence on the turbulent flame speed. Another factor which has to be taken into account is the range of u'/S_L^0 values for which the correlation has been derived. The present work focuses on lean fuel mixtures with high hydrogen content. Since these mixtures have a Lewis number below unity it is likely that a correlation including the Lewis number will perform better than a correlation that does not. Additionally the u'/S_L^0 values of the flames studied in this work will probably be the most similar to values seen (i.e. approximately 1 to 5) in the work presented by Dinkelacker et al. [22], since the studied flames are similar. Taking this into account the correlations proposed by Dinkelacker et al. and Cai et al., described in sections 3.2.1 and 3.2.4 are the most promising. Since they both include Lewis number effects and are derived for a turbulence intensity expected to be similar to the turbulence intensity for the flames in this study.

To ensure the most successful selection of a correlation an initial evaluation is made using a simple sensitivity analysis. The correlations for the turbulent flame speed used in the Zimont Turbulent Flame Speed Closure model and the models described in sections 3.2.1 and 3.2.4 are evaluated. In this analysis the mixture properties depending on the vol.% hydrogen such as the unstretched laminar flame speed, thermal diffusivity and the effective lewis number are changed accordingly. In addition, the range of the equivalence ratios corresponding to a certain vol.% hydrogen is the same as the range of the equivalence ratios that will be investigated in section 5.2.1 covering the flame regime map in the results chapter. The integral length scale is estimated based on the geometry dimensions used by Faldella [30] in his experiments. Since these dimensions will also be used in this study. This results in a value of $1.4E-3$ m for the integral length scale. The flame thickness is estimated using the following approximation $\delta = \nu/S_L^0 = \mu/\rho S_L^0 \approx 1.5E{-}5/(1{*}0.1)$. Where the viscosity and density values are typical for air and the laminar unstretched flame speed is similar to the values reported in [22]. Resulting in δ set to $1.5E-6$ m. The value varied independently either as 1 or 10 is the root mean square turbulent velocity fluctuations u'. Tables 3.2 and 4.4 provide an overview of the parameters, vol.% hydrogen, ϕ, effective Lewis numbers, α and S_L^0 that are varied in the analysis and the effect on the calculated turbulent flame speeds.

The results of the sensitivity analysis are also seen in figures 3.6 and 3.7. It is seen that the AFSW model predicts values for the turbulent flame speed much lower than the two other models for both low and high vol.% hydrogen and both values of u'. The model proposed by Cai et al. predicts values close to the Zimont model for low vol.% hydrogen and u'. On the other hand the predicted values show lower values with respect to the Zimont model for an increase in u'. For the higher vol.% hydrogen range the model proposed by Cai et al. predicts a trend similar as seen in the low vol.% hydrogen. Although the slope for the low value of u' differs, the predicted turbulent flame speeds start to deviate more from the values predicted by the Zimont model once the u' is increased. The results of the sensitivity analysis in the intermediate vol.% hydrogen range i.e. 40% and 60% are not shown since they do not show a clear trend.

As seen later in section 5.2.1 the predicted flashback bulk velocities using the Zimont model are close to the experimental values for the lower vol.% hydrogen range, but they are overestimated with respect to the experimental values for the mixture with 100% hydrogen content. Therefore the model proposed by Cai et al. still seems to be the most promising. However, this is a very preliminary conclusion and it is difficult to draw a definitive conclusion from this simple analysis. Since important factors such as the interaction of turbulence and combustion and flame shape have not been considered. For a proper analysis the turbulent flame speed correlations should be implemented in CFD, the results of this implementation can be found in section 5.3. It should be noted that the absolute values for the turbulent flame speed seen in the figures are not realistic, but when considering the values relatively to each other the comparison is useful.

vol.% hydrogen	ϕ	u' $(\mathbf{m \cdot s^{-1}})$	$Le_{eff,AFSW}$ (-)	$Le_{eff,Cai}$ (-)	St_{Zimont} $(\mathbf{m \cdot s^{-1}})$	St_{AFSW} $(\mathbf{m \cdot s^{-1}})$	St_{Cai} $(\mathbf{m \cdot s^{-1}})$
0	0.8	1	0.955	0.93	10.90	1.71	8.86
0	0.9	1	0.955	1.02	12.45	1.97	10.97
0	0.8	10	0.955	0.93	61.28	5.40	39.55
0	0.9	10	0.955	1.02	70.04	6.14	48.95
20	0.8	1	0.655	0.96	10.93	2.29	9.43
20	0.9	1	0.655	1.02	12.42	2.62	11.20
20	0.8	10	0.655	0.96	61.48	7.42	42.13
20	0.9	10	0.655	1.02	69.86	8.39	49.92
80	0.6	1	0.337	0.7	11.74	3.72	7.33
80	0.7	1	0.337	0.79	13.73	4.47	9.73
80	0.8	1	0.337	0.89	15.32	5.11	12.44
80	0.9	1	0.337	1.05	16.65	5.69	16.48
80	0.6	10	0.337	0.7	66.00	12.16	32.02
80	0.7	10	0.337	0.79	77.19	14.36	42.39
80	0.8	10	0.337	0.89	86.17	16.21	54.14
80	0.9	10	0.337	1.05	93.65	17.84	72.02
100	0.6	1	0.29	0.6	15.73	5.95	8.38
100	0.7	1	0.29	0.76	17.92	7.07	12.63
100	0.8	1	0.29	0.87	19.51	8.01	16.24
100	0.9	1	0.29	0.95	20.85	8.87	19.41
100	0.6	10	0.29	0.6	88.48	18.72	34.98
100	0.7	10	0.29	0.76	100.80	21.82	53.13
100	0.8	10	0.29	0.87	109.73	24.32	68.48
100	0.9	10	0.29	0.95	117.25	26.58	81.82

Table 3.2: Overview of turbulent flame speeds calculated with the Zimont, Dinkelacker et al. and Cai et al. correlations with varied root mean square turbulent velocity fluctuations u'. The listed effective Lewis numbers are calculated according to the methods specified by the authors in [16] and [22].

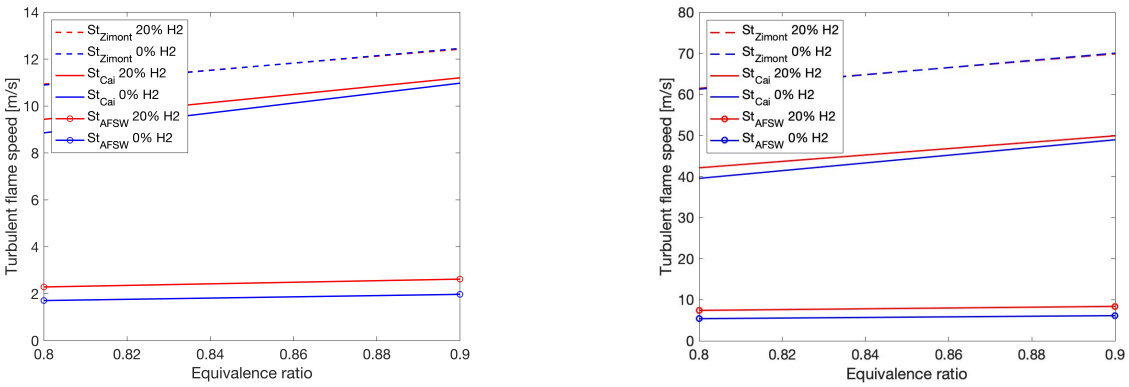

(a) 0% and 20% H2, u' = 1 m/s

(b) 0% and 20% H2, u' = 10 m/s

Figure 3.6: Turbulent flame speed

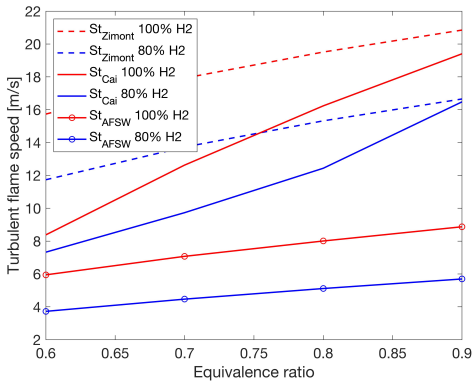

(a) 80% and 100% H2, u' = 1 m/s

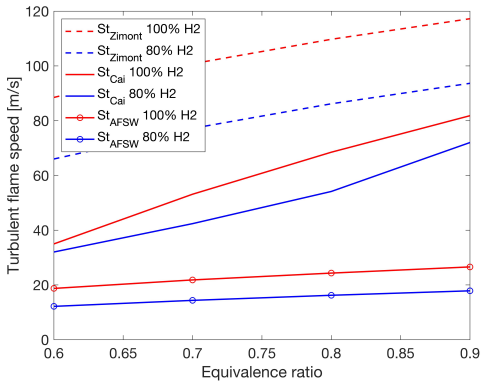

(b) 80% and 100% H2, u' = 10 m/s

Figure 3.7: Turbulent flame speed

4

Methodology

4.1. Numerical setup

This section presents the numerical setup used for the analysis of the lean premixed hydrogen tube burner. ANSYS Fluent was used for the complete study, in addition MATLAB has been used to calculate fuel mixture parameters and to process results.

4.1.1. Turbulence and combustion model

Since a large amount of calculations needed to be done to get enough data for a proper comparison with experimental results. A RANS turbulence model was selected, since this would result in the lowest amount of computational time. The used RANS model is the standard $k-\epsilon$ model as it is known for its robustness, economy, and reasonable accuracy for a wide range of turbulent flows [31]. Other RANS turbulence models were evaluated as well, however due to difficulties with reaching converged solutions it was decided to stick with the standard $k-\epsilon$ model. The standard $k-\epsilon$ has been explained in subsection 2.2.3.

The standard $k-\epsilon$ model is primarily valid for turbulent core flows, so care needs to be taken to ensure that the model is suitable for wall bounded flows. Therefore Enhanced Wall treatment was employed. The exact equations and working mechanism of Enhanced Wall Treatment can be found in the ANSYS Fluent Theory Guide [4]. A short explanation of the method will be provided in the following paragraph. Enhanced Wall Treatment combines a two-layer model and enhanced wall functions. This extends the applicability of the standard $k-\epsilon$ model throughout the near-wall region. The two-layer model will resolve the flow field up to the wall provided that the mesh is fine enough. If the mesh is not fine enough, enhanced wall functions are applied. Figure 4.1 provides an illustration of these two approaches. The mesh constraints for Enhanced Wall Treatment are based on the y^+ values of the mesh cell at the wall. The two-layer model is applied if the y^+ value for the mesh cells at the wall is equal to 1. Or at least well inside viscous sub-layer, which is the case if the y^+ value for the mesh cells at the wall is lower than 5. If this is not the case and the mesh is too coarse and wall y^+ falls inside the wall buffer region, enhanced wall functions are applied. The two layer model divides the flow in two regions, being “fully turbulent” and “viscosity affected near wall region”. In the fully turbulent region the standard $k-\epsilon$ model is applied. A region is defined as fully turbulent if: $\mathrm{Re}_y > \mathrm{Re}_y^*; \mathrm{Re}_y^* = 200$. With Re_y defined as:

$$\mathrm{Re}_y \equiv \frac{\rho y \sqrt{k}}{\mu} \tag{4.1}$$

If the constraint for the fully turbulent region is not satisfied (i.e. $\mathrm{Re}_y^* < 200$), the region is defined as the viscosity affected near wall region. In this region the one equation model of Wolfstein is employed. The one equation model of Wolfstein is a low Re number model, which dampens the turbulent viscosity close to the wall. The two-layer viscosity is smoothly blended with the high Re number viscosity from the outer region. As previously mentioned, enhanced wall functions are applied if the mesh is too coarse, that is if the y^+ value for the mesh cells at the wall is greater than 5. The enhanced wall function is in principle a wall law for the entire near wall region, general theory on wall functions can be

found in subsection 2.2.5. The wall law for the entire near wall region is achieved in Fluent by blending linear (for laminar flow) and logarithmic (for turbulent flow) laws-of-the-wall. This guarantees correct flow behavior in case the mesh is not fine enough. In this study the mesh is always designed to ensure the y^+ values for the mesh cells at the wall are always lower than 5. Therefore the two layer model is always applied.

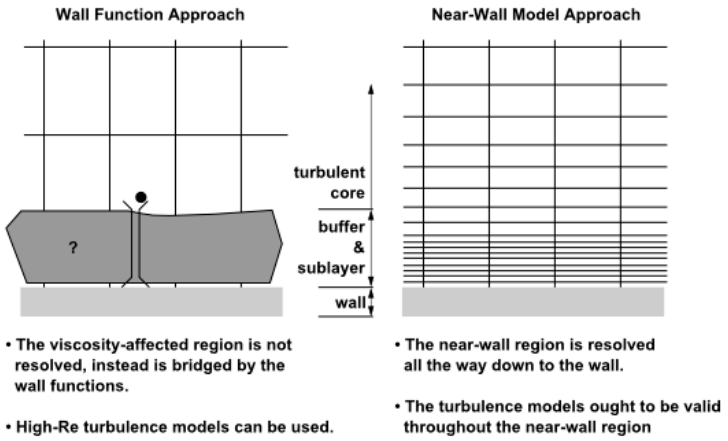

Figure 4.1: Near wall treatment methods. The left side shows a wall function approach and the right side shows a near wall model (e.g. Low Reynolds number model) approach. Figure from taken from the ANSYS theory guide [4].

The combustion model that is used in this study is the adiabatic premixed combustion model with the Zimont turbulent flame speed correlation, which is a standard ANSYS Fluent model. This model is a flamelet model. The flamelet modeling approach and the transport equation for the progress variable were presented in subsection 3.1.3. The source term in the progress variable transport equation is modeled using the Zimont turbulent flame speed correlation presented in subsection 3.1.4. An attempt to improve the numerical model will be based on changing the turbulent flame speed correlation implemented in ANSYS Fluent, the results of this improvement attempt can be found in section 5.3. For all cases the stretch factor G is set to 1.

As described earlier in subsection 3.1.4 the Zimont turbulent flame speed correlation was derived under several constraints, being $\mathrm{Re}_t >> 1$, $Da >> 1$, $Ka > 1$. Dinkelacker and Hölzler [21] validated the model for a wider range than the originally specified constraints being Damköhler numbers between 2 and 70 and Karlovitz numbers between 0.1 and 4.6. The typical values of the flames in this study are $\mathrm{Re}_t \approx 3.5\mathrm{e}3$ to $10\mathrm{e}3$, $Da \approx 15$ to 30 and $Ka \approx 0.7$ to 2.5.

For all the simulations performed, the used solver is pressure based. A second order upwind scheme was used to solve the equations for pressure, momentum, turbulent kinetic energy, turbulent dissipation rate and progress variable. The ANSYS Fluent Theory Guide [4] states that a coupled algorithm improves the solution in case of poor mesh or large time steps. And since the meshes will be used for multiple flames the coupled scheme was applied to the pressure-velocity coupling. Which ensures proper convergiences even if the mesh is not optimal. Furthermore, the Least Squares Cell Based approach was used for the calculation of gradients.

The modeling approach can be either steady state or transient. A steady state simulation computes a fully developed flow field that does not change in time. If no instabilities occur a steady state approach can suffice. The results of section 5.1 were produced using multiple steady state simulations corresponding to different bulk velocities. If the goal of the simulation is to determine the occurrence of an instability such as flashback, a transient method is more convenient. A transient simulation computes the instantaneous values at each moment in time for each quantity. Meaning a developing flow field can be captured. It should be noted that a transient simulation has much higher computational requirements in comparison to a steady state simulation. Furthermore a transient simulation requires a specified time step and a number of iterations per time step. A rule of thumb applied to determine the

time step, is to set the time step to a value smaller than the smallest cell size divided by the velocity. The smallest cell size can be determined from the mesh. The observed velocity differs and therefore the time step can vary per case. The number of iterations per time step is often used in CFD modeling ranges from 15 to 20, however most important is that the solution converges and therefore this value can also be varied for each case. In this study it was observed that for most cases convergence could be reached using a time step of $1.25e{-}3$ seconds and 10 iterations per time step. Since this study focuses on finding the moment of flashback, the studied flames are stable until they are close to flashback. Furthermore this study focuses on flame characteristics such as flame cone angles of stable flames. As a result the time step can be quite long and the number of iterations per time step can be quite low. Finally the total number of iterations/time steps is dictated by the available computational power and depends on the required time to be simulated. In this study the maximum number of time steps was usually set to 8000. The results of sections 5.2 and 5.3 were obtained using the described transient modeling approach.

4.1.2. Geometries and boundary conditions

Faldella [30] used three different pipe diameters for his experiments. Since his experimental results will be used to validate the numerical results, the same diameters are used in the numerical setup. Since a pipe geometry is modeled, the most efficient geometry setup is 2D axisymmetric. Which is employed in this study.

The complete geometry is seen in figure 4.2. The geometry dimensions corresponding to the different pipe diameters are seen in table 4.1. Turbulent flow in a pipe is known to be fully developed after a flow length of $50D$ as indicated by Doherty et al [23]. Therefore the length of the pipe is chosen as 50 diameters. To avoid feedback effects of the pressure when modeling a jet flow, the far field boundary condition is required a domain of 20 times the characteristic length. In this case that is the pipe diameter. Therefore the radial far field boundary should be approximately $20D$ from the pipe axis. To include the pipe wall thickness this boundary is located at $20D + th$. The pressure inlet boundary conditions is located $25D$ upstream of the pipe outlet, to ensure proper modeling of effects at the pipe outlet. The length of the geometry downstream of the pipe outlet is $100D$, which is an area large enough for flames with varying bulk velocities.

The boundary conditions corresponding to the numbers 1, 2, 3, 4 and 5 seen in figure 4.2 are listed in table 4.2. The relevant parameters for the boundary conditions are specified as well. Boundary condition 1 is a velocity inlet. The magnitude of the velocity is the specified bulk velocity, this is a variable value changed according to the flame requirements. If the goal is to determine the bulk velocity near the flashback point, a transient modeling approach is employed and this boundary condition is time dependent. After 4 simulated seconds (e.g. 3000 iterations of 1.25e-3 second) the bulk velocity is lowered 1 m/s or 0.5 m/s over the duration of 1 second using a user defined function for the boundary condition. This process repeats until flashback occurs, the occurance of flashback is identified visually. Furthermore the inlet temperature of boundary condition 1 is always set to 300 K. The turbulence intensity is set to 5% for all cases, since all bulk velocities of the modeled flames result in an initial turbulence intensity close to 5%. Boundary condition 2 is a velocity inlet with a velocity magnitude of only 0.05 m/s. This boundary conditions allows for suction effects of the flame on the surroundings, which results in stronger convergence during modeling. The far field boundary condition 3 is a symmetry boundary, another possibility for this boundary condition would be a pressure inlet or outlet. However there is almost no interaction between this boundary and the flame, therefore a symmetry boundary results in stronger convergence during modeling. Boundary condition number 4 is a pressure outlet, the turbulent kinetic energy and turbulent dissipation rate of the potential back flow of this boundary are set to 0, the potential back flow of the progress variable is set to 1. Boundary condition number 5 is the pipe axis.

Burner tube internal diameter, D **(mm)**	$150D$ **(mm)**	$125D$ **(mm)**	$50D$ **(mm)**	$25D$ **(mm)**	$19.5D$ **(mm)**	$20D + th$ **(mm)**	**Wall thickness,** th **(mm)**	$D/2$ **(mm)**
20.06	3009	2507.5	1003	501.5	391.17	402.2	1	10.03
25.67	3850.5	3208.75	1283.5	641.75	500.565	514.5	1.1	12.835
39.2	5880	4900	1960	980	764.4	785.4	1.4	19.6

Table 4.1: Geometry dimensions

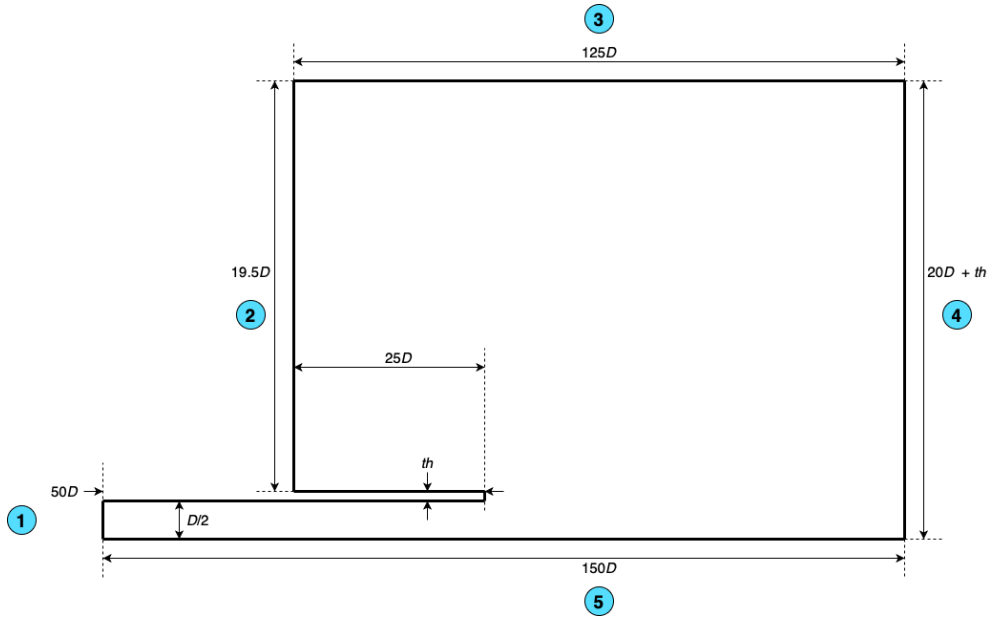

Figure 4.2: Geometry dimensions, proportions not on scale.

Number	Boundary condition	Velocity magnitude U ($\mathbf{ms^{-1}}$)	Turbulent kinetic energy k ($\mathbf{m^{-2}s^{-2}}$)	Turbulent dissipation rate ϵ ($\mathbf{m^{-2}s^{-3}}$)	Turbulence intensity I (%)	Integral length scale l_t (m)
1	Velocity inlet	Variable	-	-	5	$0.07D$
2	Velocity inlet	0.05	0	0	-	-
3	Symmetry	-	-	-	-	-
4	Pressure outlet	-	0	0	-	-
5	Axis	-	-	-	-	-

Table 4.2: Boundary conditions. If a value does not need to be specified at a certain boundary condition it is left blank (-).

4.1.3. Mesh

A computational fluid dynamics model, tries to approximate a continuous solution using discrete elements. These discrete elements are formed by the mesh. As the number of mesh elements increases and the mesh becomes finer, typically the solution will be more accurate. However, a finer mesh also results in an increased computation time. Using an optimized mesh, an ideal trade-off between required accuracy and available computational power can be obtained.

A method used to determine whether the trade-off between accuracy and computational time is optimal, is the mesh independence study. In other words the mesh independence study checks that given a level of accuracy for the solution, the used mesh is fine enough to achieve that accuracy using minimum possible computational power. Optionally the results of the numerical solution can be compared to experimental data or data generated using a modeling approach with higher accuracy such as LES or DNS. An optimum mesh should result in a level of accuracy which is able to capture all the necessary flow features, such as velocity gradients and so forth. A mesh that is too coarse will not be able to capture all the relevant flow features and is therefore not a solution of the required accuracy level. A finer mesh on the other hand will result in a solution of a little higher accuracy than required but at the expense of computational power and time.

The mesh independence study can be performed by isolating an area of interest on the geometry. And if the model is small enough, this can be the entire geometry. First an initial coarse mesh is developed for the area of interest. Then multiple finer meshes are created for the same area. Only

the mesh sizing is changed. Other settings such as the element type, or the geometry size are not changed. This ensures a proper comparison between the meshes. Furthermore the refinement of the mesh should be significant. And for a proper comparison at least 3 meshes with sufficient differences should be studied. Finally the influence of the mesh refinements on the results should be studied, ideally multiple flow quantities are evaluated. For this study the selected flow quantity is the velocity profile.

Ideally a mesh independence study would be performed for every simulation. However due to limited availability of computational power and time this is not feasible. Therefore only a mesh independence study is conducted for a cold flow using the geometry seen in figure 4.2 with a pipe diameter of 39.2 mm and a Reynolds number of 5300 in combination with the turbulence model explained in subsection 4.1.1. The selected flow quantity used to study the influence of the mesh refinement is the axial velocity in the pipe normalized with the center line velocity versus the non dimensional pipe radius. The turbulent velocity profile is determined 10 diameters in front of the pipe exit. The mesh is a structured grid with quadrilateral elements. The element density at the pipe exit is increased while maintaining a smooth transition of smaller to larger mesh elements. The result of the mesh independence study is seen in figure 4.3. Looking at figure 4.3a it can be seen that the coarse and fine meshes result in a similar velocity profile. Although by zooming in on the velocity profile, it becomes evident that refining the mesh does influence the velocity profile. However the changes in the velocity profile are far less significant when the mesh is refined from 128032 nodes to 488061 mesh compared to a refinement from 4812 to 128032. Therefore it can be concluded that the mesh refinement study indicates a mesh independence for the cold flow for a mesh with approximately $125e3$ nodes.

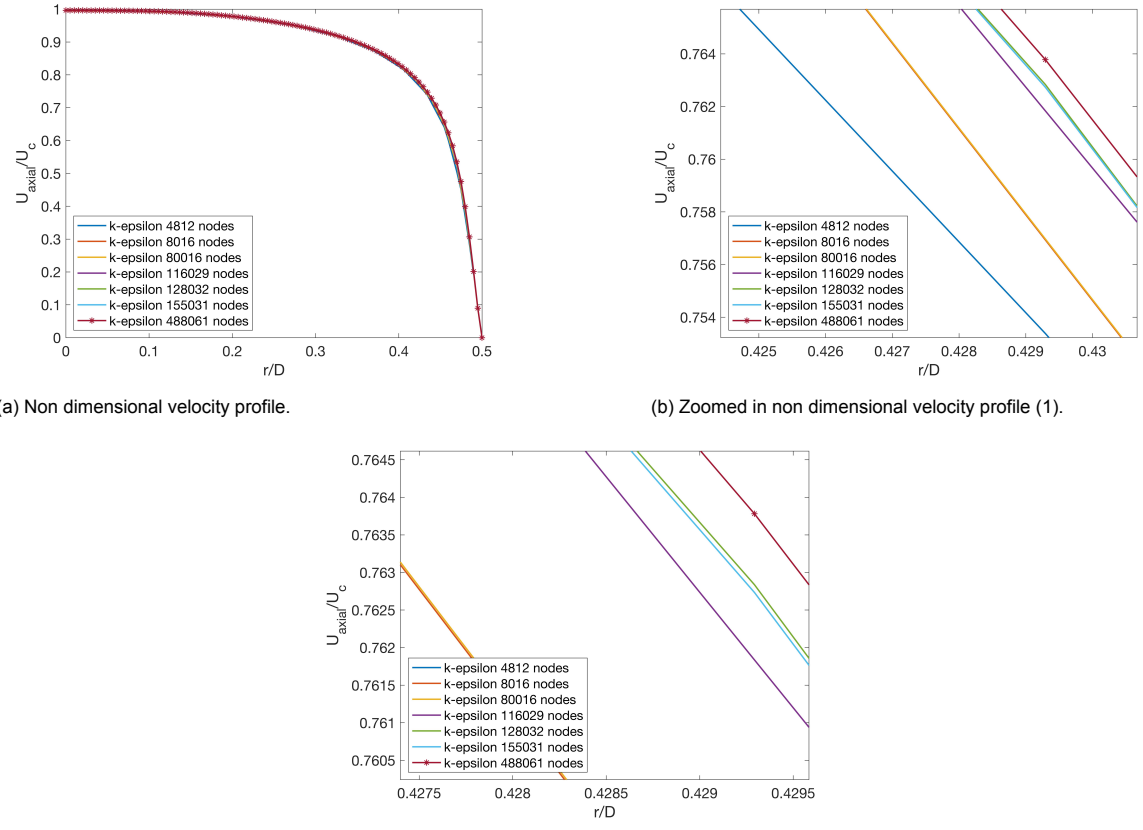

(a) Non dimensional velocity profile.

(b) Zoomed in non dimensional velocity profile (1).

(c) Zoomed in non dimensional velocity profile (2).

Figure 4.3: Non dimensional turbulent pipe flow velocity profile grid refinement study.

The mesh independence study focused on a case with cold flow and a Reynolds number of 5300. During this study, which focuses on combustion, it became clear that it was becoming more difficult to reach convergence for flows with higher Reynolds numbers. Therefore it was decided to use a mesh

finer than the initially determined optimal point. For all tree different geometries a mesh with 307066 nodes was used, as can be seen in table 4.3.

Geometry diameter (mm)	Number of cells	Number of nodes	Aspect ratio	Minimum orthogonal quality
20.06	304500	307066	15.37	0.9284
25.67	304500	307066	15.37	0.9288
39.20	304500	307066	15.37	0.9292

Table 4.3: Mesh information.

An overview of the mesh properties is seen in figure 4.4. Figure 4.5 shows two zoomed in mesh views, where the mesh bias towards the pipe exit is clearly observed.

Figure 4.4: Mesh overview.

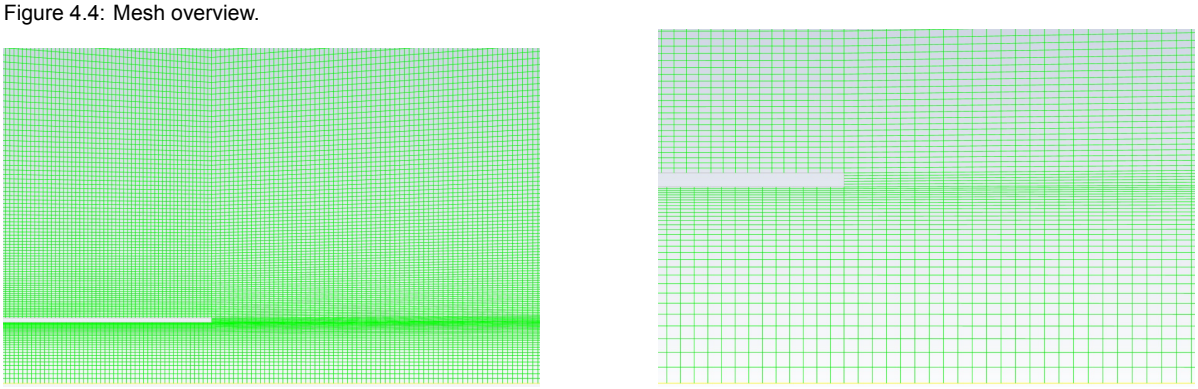

(a) Zoomed in mesh (1).

(b) Zoomed in mesh (2).

Figure 4.5

Furthermore the mesh information table shows the minimum orthogonal qualities and the aspect ratios. The mesh orthogonality relates to how close the angles between adjacent element faces are to the optimal angle (i.e. 90 degrees). The orthogonal quality ranges from 0 to 1, an ideal mesh would have a minimum orthogonal quality equal to 1. It should be noted that due to the increased mesh density at the pipe exit, the minimum values in orthogonal quality are observed far from the pipe exit, as can be seen in figure 4.6. Therefore the lower values of the orthogonal quality can be tolerated in the used mesh.

To ensure stable convergence the aspect ratio should have values lower than 35 in the entire domain, lower than 10 in the boundary layer and lower than 5 in the bulk flow. These constraints are also satisfied and the highest aspect ratios are observed far away from the pipe exit, similar to the orthogonal quality.

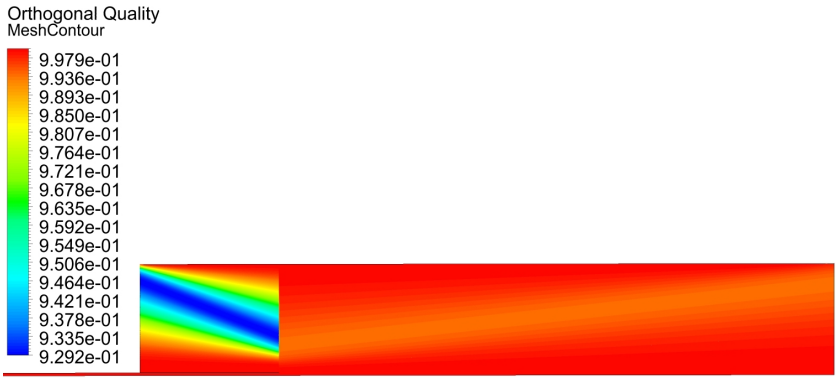

Figure 4.6: Orthogonal quality of the mesh of the geometry with a diameter of 39.20mm.

4.1.4. Combustion parameters

To complete the numerical setup multiple fuel mixture properties should be determined. The variables to be determined are the adiabatic flame temperature T_{ad}, unstretched laminar flame speed S_L^0, thermal diffusivity α, density ρ_{fuel} and the dynamic viscosity μ_{fuel}. This subsection will explain how these fuel properties are determined. The adiabatic flame temperature has been determined using equilibrium calculations with the chemical kinetics software Cantera [34]. The other fuel mixture properties have been determined using a variety of correlations. The correlations are mostly focused on one of the elements of the fuel mixture; hydrogen, methane or air. Combining the correlations enables the possibility to determine all the mentioned properties of the fuel mixture in different compositions.

The thermal conductivities of hydrogen, methane and air have been determined using the correlations found in [6], [77], and [42] respectively. The viscosities were obtained at room temperature and pressure. Pressure and temperature effects can then added according to Sutherland's law with three coefficients. The mass diffusivities were also obtained at room conditions and then pressure and temperature dependence can be added according to correlation by Fuller, Schetter and Gittings. The specific heat capacities have been calculated using NASA polynomials, information on the NASA polynomials can be found in [15]. The densities of hydrogen and methane have been determined using the correlations found in [50] and [48] respectively. The density of air has been determined using the ideal gas law, since the operating conditions are far away of the critical points. The unstretched laminar flame speeds of hydrogen and methane have been determined using the correlations found in [72] and [3] respectively. The unstretched laminar flame speed of the hydrogen methane mixtures has been determined using the correlation found in [12], which interpolates the calculated unstretched laminar flame speeds of hydrogen and methane. The thermal diffusivities are determined using the following formula:

$$\alpha = \frac{\kappa}{\rho_{fuel} c_p} \tag{4.2}$$

In which κ is the thermal conductivity and c_p is the specific heat capacity. An overview of the fuel mixture properties of all flames modeled in this study is seen in table 4.4.

vol.% hydrogen	**vol.% methane**	ϕ	α $(\mathbf{m^2 \cdot s^{-1}})$	ρ_{fuel} $(\mathbf{kg \cdot m^{-3}})$	μ_{fuel} $(\mathbf{kg \cdot m^{-1} \cdot s^{-1}})$	T_{ad} **(K)**	S_L^0 $(\mathbf{m \cdot s^{-1}})$
0	100	0.8	2.2121E-05	1.1359	1.7612E-05	1997	0.2596
0	100	0.9	2.2118E-05	1.1313	1.7555E-05	2134	0.3391
20	80	0.8	2.3390E-05	1.1192	1.7634E-05	2008	0.2763
20	80	0.9	2.3527E-05	1.1127	1.7580E-05	2145	0.3589
40	60	0.8	2.5189E-05	1.0960	1.7664E-05	2024	0.3210
40	60	0.9	2.5524E-05	1.0871	1.7613E-05	2159	0.4115
60	40	0.7	2.7290E-05	1.0744	1.7756E-05	1890	0.3250
60	40	0.8	2.7941E-05	1.0618	1.7709E-05	2047	0.4402
60	40	0.9	2.8575E-05	1.0495	1.7662E-05	2182	0.5520
80	20	0.6	3.0291E-05	1.0431	1.7862E-05	1755	0.4124
80	20	0.7	3.1499E-05	1.0243	1.7821E-05	1930	0.5866
80	20	0.8	3.2671E-05	1.0063	1.7781E-05	2087	0.7582
80	20	0.9	3.3808E-05	0.9891	1.7740E-05	2219	0.9268
100	0	0.6	3.8141E-05	0.9560	1.7973E-05	1838	0.9333
100	0	0.7	4.0459E-05	0.9276	1.7943E-05	2013	1.2847
100	0	0.8	4.2692E-05	0.9010	1.7911E-05	2167	1.6066
100	0	0.9	4.4845E-05	0.8760	1.7878E-05	2296	1.9268

Table 4.4: Properties of the fuel mixture compositions.

5

Results and Discussion

This chapter presents and discusses the results of three different topics on numerical modeling of flame flashback.

1. Identification of the conditions leading to flashback.
2. Experimental validation.
3. Evaluation of turbulent flame speed correlations.

5.1. Identification of the conditions leading to flashback

This section explains the results of modeling the approach to flashback conditions using the standard k-epsilon model with enhanced wall treatment in combination with the Zimont turbulent flame closure model for a flame with 20 vol.% hydrogen, 80 vol.% methane and an equivalence ratio of 0.8 using a pipe geometry with inner diameter of 39.20 mm and a wall thickness of 1.4 mm. Since enhanced wall treatment is employed, the flow is resolved up to the wall instead of using a wall function. Therefore the actual boundary layer flashback process can be modeled. However it should be noted that using a Reynolds averaged turbulence model results in the averaged 'real world' transient flashback process. Therefore this modeling approach is not used to study the actual flashback process, but only to determine when the flashback occurs. The flashback is initiated by lowering the bulk velocity from 5.5 m/s to 2.64 m/s which is on the flashback limit, further lowering the bulk velocity by only 0.5% leads to flashback. The aim of this numerical experiment is to gain insight in the relevant mechanisms driving the occurrence of the instability and trying to identify a method for predicting flashback. The results of the experiment will be presented in two ways, firstly by evaluating pressure contours and secondly by testing hypotheses and flashback theory using multiple graphs focusing on certain flow properties.

5.1.1. Pressure contours and flame front

The pressure contour graphs seen in figures 5.1, 5.2, 5.3 and 5.4 show the development of the pressure values in the vicinity of the flame front. They also show the change in flame front location due to the change in bulk velocity and pressure. It should be noted for all figures that the legends have different values, the max value in figures 5.1, 5.2, 5.3 and 5.4 corresponds to 8, 6, 5 and 4 pascal respectively. Furthermore the white area represents the pipe wall.

Looking at figures 5.1, 5.2, 5.3 and 5.4 a few things stand out that apply to all figures. The flame front corresponding to a progress variable value of 0.2, lies approximately along the line dividing the green and blue low pressure contours. (The value 0.2 is chosen since the steepest gradient in density is always observed near this value. Therefore it represents a realistic flame front location.) Also it immediately stands out that there is a high pressure in front of the flame front and a low pressure downstream the flame front. This high pressure upstream and low pressure downstream of the flame front is caused by the flame induced adverse pressure gradient. Following Bernoulli's principle it can be understood that the flame induced pressure gradient is the result of the acceleration of gas over the

flame front due to the temperature increase in the flame. The maximum pressure near the pipe wall (red region in the figures) is the result of the flame front being more perpendicular to the incoming flow at the location near the pipe wall. Therefore it is expected that the resulting pressure field has a stronger influence on the incoming flow at this location, this expectation will be tested in subsection 5.1.2 using multiple hypotheses. Another effect is the smaller distance from the radial plane at the pipe outlet to the flame front location resulting in a stronger effect of the burner wall that hampers flow deflection.

Now when looking at the change of the location of the flame front it can be seen that lowering the bulk velocity results in a shorter flame and a flame front which lies more parallel to the radial plane of the pipe. In particular, the flame front increases to be more parallel to the radial plane of the pipe at a radial location almost equal to the pipe radius. As a result of this change in flame front angle, the isobars of the pressure field will also start to be increasingly parallel to the radial plane of the pipe for a decreasing bulk velocity. The effect of the changing pressure field will also be evaluated in the next subsection. Furthermore it is expected that due to the adverse pressure gradient of the flame, the incoming flow is slowed down. The decrease of the axial velocity component, implicates that the mass must flow in a different direction. Therefore the radial velocity component must increase with respect to the axial velocity component, since the mass continuity equation must be satisfied. This hypothesis will also be tested in the following subsection. Moreover, it can be seen that for the flame closest to flashback the flame front starts to be increasingly more parallel to the radial plane of the pipe over a greater length of the flame front.

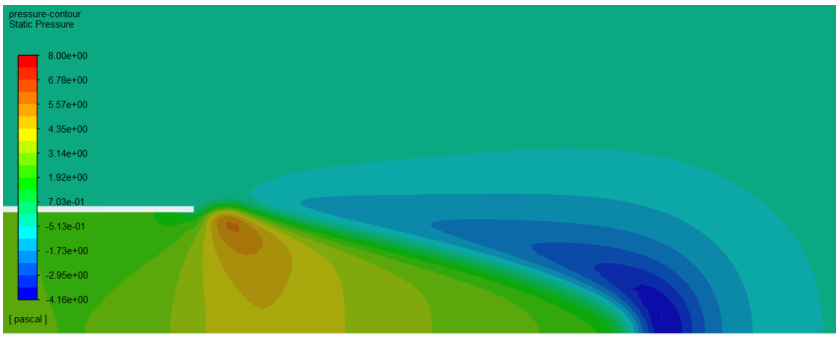

Figure 5.1: Pressure contours, bulk velocity = 5.5 m/s.

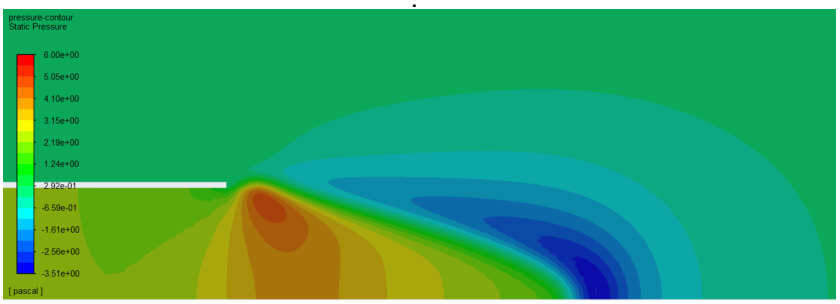

Figure 5.2: Pressure contours, bulk velocity = 4.5 m/s.

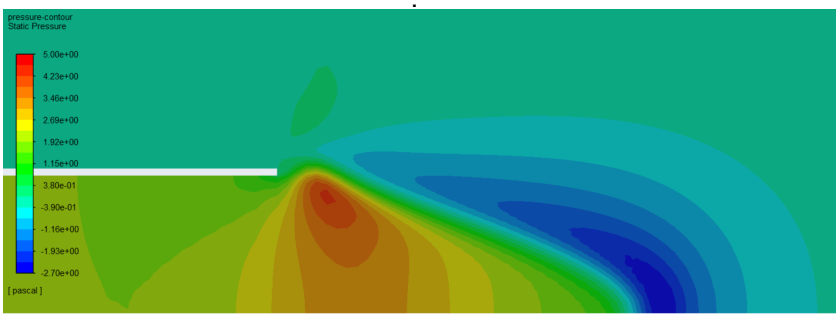

Figure 5.3: Pressure contours, bulk velocity = 3.5 m/s.

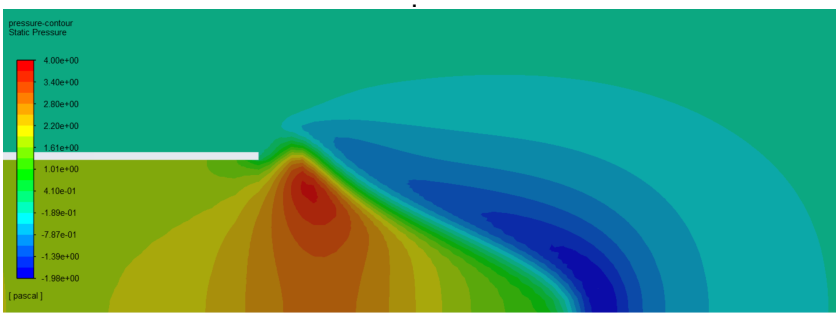

Figure 5.4: Pressure contours, bulk velocity = 2.64 m/s.

5.1.2. Local analysis of flashback initiation

The pipe wall and the flame front locations corresponding to a progress variable of 0.2 for flames with the bulk velocities ranging from 2.64 to 5.5 m/s are plotted in figure 5.5. As described previously, the flame length decreases when the bulk velocity decreases, resulting in a flame front which is increasingly more parallel to radial plane of the pipe. Furthermore it is even more obvious that this occurs the most near the pipe outlet at a radial location almost equal to the pipe radius as seen in figure 5.5b. The resulting pressure field therefore has a stronger influence on the incoming flow at this location. In this subsection certain hypotheses will be tested to determine if this is indeed the case. Furthermore it will be evaluated whether the results can also be used to predict in advance that the flame is close to flashback.

Since this study focuses on boundary layers flashback and the area at a radial location just below the pipe wall seems to be the most interesting to study, the main focus will be on values along a constant radius near the pipe wall. This line is plotted in the figures as 'y line' and corresponds to r/D is equal to 0.4847 (or y = 0.019 m).

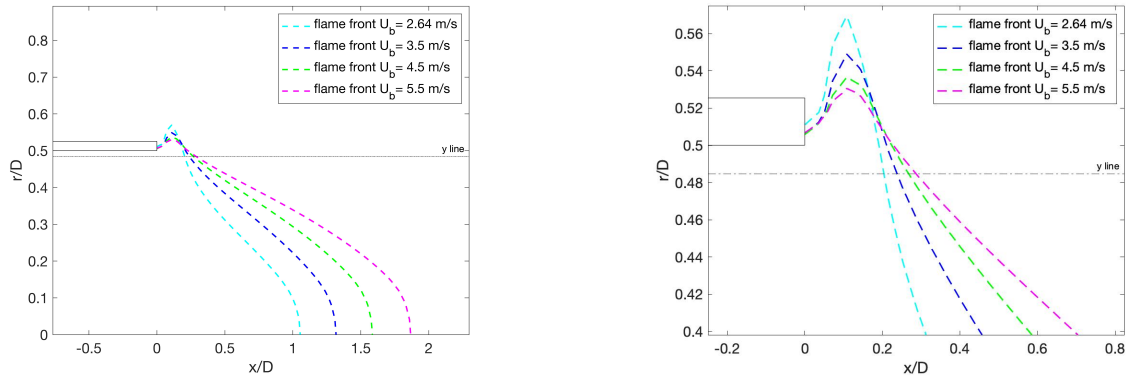

(a) Flame front locations.

(b) Flame front locations zoomed in.

Figure 5.5: Flame front locations overview and zoomed in.

As seen in subsection 5.1.1 the development of the pressure field plays an important role in the flashback process. However as previously indicated the absolute values of the observed pressure differ. Therefore a dimensionless relative pressure allows for a better comparison. The dimensionless pressure used is seen equation 5.1 and is known as the pressure coefficient [49].

$$C_p = \frac{p(x) - p_{ref}}{\frac{1}{2}\rho U_b^2} \tag{5.1}$$

In which $p(x)$ is the pressure along a (stream)line, ρ is the density of the unburned mixture, U_b is the bulk velocity of the unburned mixture in the pipe defined as the total volumetric flow rate divided by the cross sectional area of the pipe. And p_{ref} is the reference pressure, here defined as the ambient pressure equal to zero. In other words $p(x) - p_{ref}$ is the static pressure. Meaning a pressure coefficient below the ambient pressure is negative. Using this method it is the same for all cases.

First hypothesis:

- *The gradient with respect to the x axis of the pressure coefficient will show the highest maximum and lowest minimum for the flame closest to flashback.*

To gain more insight in the development of the pressure when approaching flashback conditions by lowering the bulk velocity, the gradient of the pressure coefficient dC_p/dx is plotted along the 'y line' previously described, see figure 5.6. The left and right vertical dotted lines, seen in the figure correspond to the flame front locations ($c = 0.2$) at the height of the 'y line' of the flames with a bulk velocity of 2.64 m/s and 5.5 m/s respectively. The vertical line located at x/D equal to zero is the location of the pipe outlet. Taking into consideration the results presented in subsection 5.1.1 the dimensionless

pressure gradients are as expected. Meaning a maximum value is observed upstream of the flame front and minimum value is observed just downstream of the flame front due to the acceleration over the flame front and the pressure resulting from the flame induced adverse pressure gradient. Finally the gradient converges back to zero, since the pressure approaches ambient pressure. Interestingly the dimensionless pressure gradient shows the highest maximum and lowest minimum value for the flame closest to flashback conditions. Which confirms the first hypothesis. However, these maximum and minimum values do not appear to be fixed values that can be used to predict that the flame is near flashback.

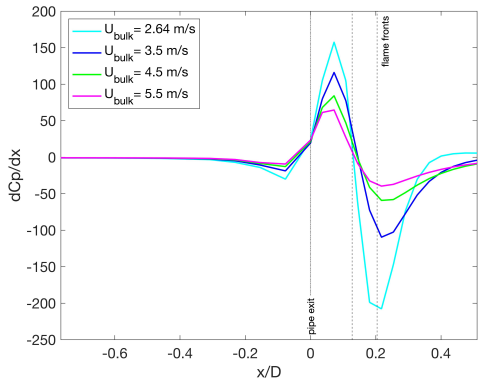

Figure 5.6: dCp/dx plotted along y line with constant r.

Second hypothesis:

- *The radial velocity will increase with respect to the bulk velocity during the approach to flashback conditions.*

It is expected that when the flame front and the isobars of the pressure field start to be more parallel to the radial plane of the pipe exit, the incoming axial flow velocity component will slow down. This should result in an increase in the radial flow velocity component, since the continuity equation must be satisfied. In figure 5.7a the radial velocity along the constant radius 'y line' is plotted. In figure 5.7b the radial velocity divided by the bulk velocity is plotted along the same line. Once again the vertical lines indicate the flame fronts and pipe outlet. The figure shows that the radial velocity remains zero and starts to increase just before the pipe outlet. Once the flow has exited the pipe the radial velocity keeps increasing. Only when the flow is at a certain distance downstream of the flame front, the radial velocity starts to decrease again. Despite the differences in bulk velocity, the radial velocity observed before the flow reaches the flame front increases at almost the same rate for all flames. This means that the radial velocity increases with respect to the bulk velocity as seen in figure 5.7b. Where can be seen that the radial velocity increases at the highest rate with respect to the bulk velocity for the flame closest to flashback conditions. This means that due to a decreasing bulk velocity and increasingly parallel flame front with respect to the radial plane of the pipe, the axial velocity component is hampered and therefore the radial velocity component increases. Which confirms the second hypothesis. Although it is very clear that the flow is hampered, the comparison of radial velocity does not provide enough information to predict that the flame is near flashback.

Third hypothesis:

- *The wall shear stress will go to zero during the approach to flashback conditions. (Confined flashback theory)*

The pressure rises when the flow approaches the flame front, therefore the fuel mixture is decelerated. As the bulk velocity decreases and the flame gets closer to flashback conditions, the dimensionless flame induced adverse pressure gradient rises. The flow in the boundary layer is affected more greatly by the increasing pressure gradient, due to the lower velocity with respect to the center-line velocity. Since the fuel mixture moves along the pipe wall which is a solid boundary a shear stress will be

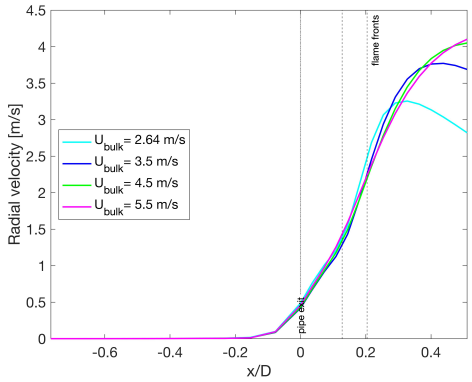

(a) Radial velocity plotted along y line with constant r.

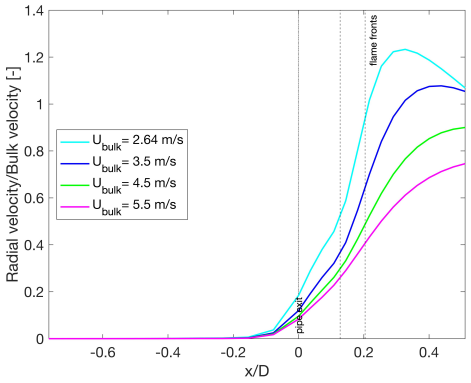

(b) Radial velocity/Bulk Velocity, plotted along y line with constant r.

Figure 5.7: Radial velocity and Radial velocity/Bulk velocity, plotted along y line with constant r.

exerted on the boundary, as seen in equation 5.2. However as long as the velocity gradient at the wall is positive, the shear stress is still positive as well.

$$\tau_w = \mu \left(\frac{\partial u}{\partial y} \right)_{y=0} \tag{5.2}$$

According to the theory for confined boundary layer flashback based on the Stratford's turbulent boundary layer separation criterion as developed by Eichler [28] and further worked out by Hoferichter [38]. The backpressure generated by the flame can induce great enough flow separation from the wall to allow the flame to propagate upstream and trigger flashback. This flow separation occurs when the wall shear stress goes to zero. Meaning the separation point is defined by a velocity gradient equal to zero. The paper by Björnsson et al. [10] presents a generalized separation criterion which is an improvement and extension of the boundary layer flashback model. In this model the flame induced pressure gradient caused by thermal expansion is related to the turbulent flame speed using the following equation:

$$S_t = \sqrt{\frac{\Delta p}{\rho_u \left(\frac{\rho_u}{\rho_b} - 1 \right)}} \tag{5.3}$$

In which Δp is the difference between the pressure in the unburned and burned regions. In figure 5.8 this turbulent flame speed is compared to the Zimont turbulent flame speed. Since the predicted values match fairly well, the flame induced pressure gradient is related to the turbulent flame speed in a similar way when modeled with the Zimont model and applied to an unconfined geometry.

To summarize; there is a moment where the fluid close to the wall cannot flow towards the pipe outlet anymore as the axial velocity component vanishes. As a consequence, the fluid particles are deflected away from the wall and a back flow region is formed. This moment is defined by the separation point with a velocity gradient and wall shear stress equal to zero. In theory it should be possible to find the separation point with the used modeling approach, since enhanced wall treatment is used and the flow is resolved all the way up to the pipe wall. Furthermore figure 5.8 shows that the Zimont correlation results in a relation between the turbulent flame speed and the pressure difference over the flame similar to the relation used in the theory on confined flashback. To study the separation point, the wall shear stress of the different flames is plotted in figure 5.9. The figure shows that the wall shear stress decreases for a decreasing bulk velocity. This is in line with expectations since the velocity gradient reduces due to a decreasing bulk velocity. However even very close to flashback conditions the wall shear stress is still positive and no separation point occurs. This means the results did not confirm the third hypothesis.

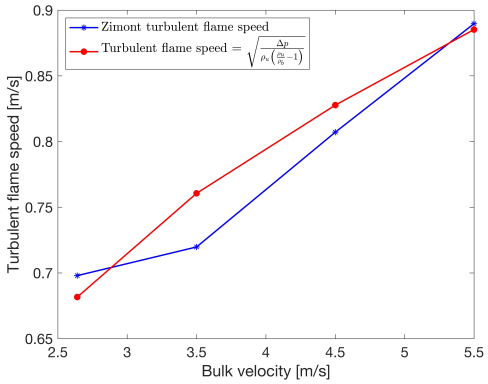

Figure 5.8: Turbulent flame speeds on the flame front along the y-line based on the Zimont correlation and equation 5.3. Actual experiments indicated by markers

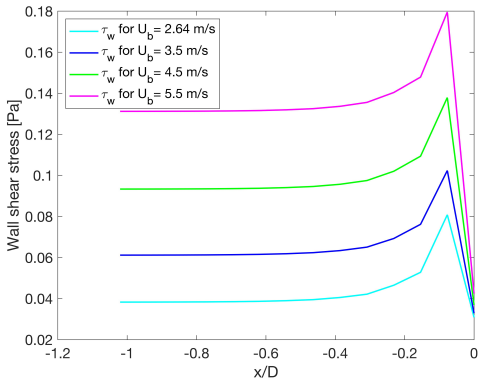

Figure 5.9: Wall shear stress.

Fourth hypothesis:

- *The flow velocity falls below the turbulent flame speed of the flame near flashback conditions. (Unconfined flashback theory)*

In this study an unconfined flame is modeled and so far only flashback theory for confined flames has been considered. Flashback theory also exists for unconfined geometries as presented by Baumgartner et al. in [7]. Who concluded that boundary layer flashback of unconfined flames is initiated if at some point the flow velocity falls below the turbulent burning velocity of the flame. Prior to this point, the axial flow velocity should equal the axial component of the turbulent flame speed. The theory to predict the flashback limits for unconfined flashback has been substantiated by Hoferichter [37]. To evaluate if the theory for unconfined flame flashback holds for this study, the axial component of the turbulent flame speed has been plotted against the axial velocity just upstream of the flame front (which is just downstream of the pipe exit), along multiple constant radius lines including the 'y-line'. The results seen in the figures 5.10 are quite interesting since they show that the axial component of the turbulent flame speed increases for a decreasing bulk velocity. Which is due the fact that the flame front is increasingly parallel to the radial plane of the pipe and therefore the magnitude of the axial velocity component of the turbulent flame speed increases. The results also show that for the flame closest to flashback conditions, the axial component of the turbulent flame speed has a value similar to the axial velocity slightly upstream of the flame front. The magnitude of the velocities have the most similar values along the constant radius line closest to the pipe wall, as seen in figure 5.10c. However the velocities do not have the same value and the flow velocity is still higher than the turbulent flame speed. Therefore the fourth hypothesis has not been confirmed.

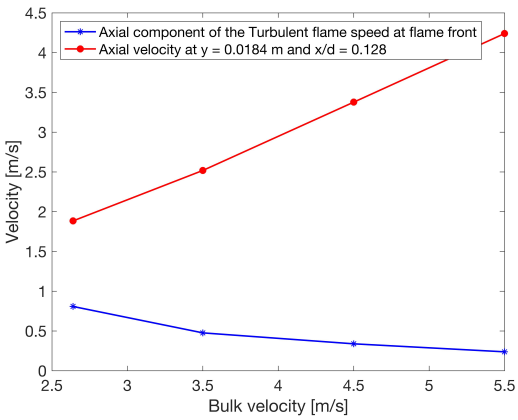

(a) Along radial line y = 0.0184 m (or r/D = 0.4694).

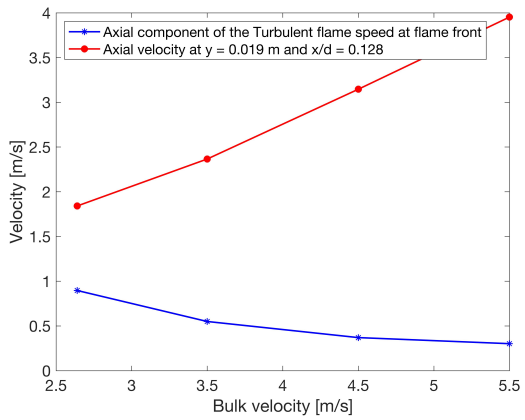

(b) Along y-line, y = 0.019 m (or r/D = 0.4847).

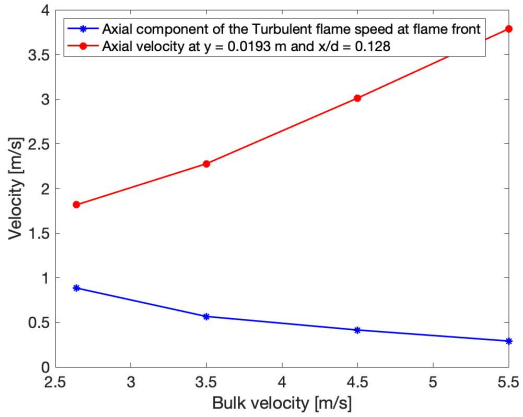

(c) Along radial line y = 0.0193 m (or r/D = 0.4923).

Figure 5.10: Axial component of turbulent flame speed vs axial velocity upstream of pipe exit along multiple constant radius lines. Actual experiments indicated by markers.

Fifth hypothesis:

- *If a flame is closer to flashback, a streamline close to the pipe wall will be deflected stronger.*

The gradient of the pressure coefficient (which is corrected for the difference in bulk velocities) shows the highest maximum and lowest minimum for the flame closest to flashback. Therefore it is expected that a streamline starting from one point will show the greatest deflection for the flame closest to flashback. To test this hypothesis streamlines starting far upstream of the flame at the same radius as the 'y-line' are plotted in figure 5.11. The pipe wall and corresponding flame fronts are plotted as well. To complete this analysis the pressure and pressure coefficient are also plotted along the streamlines in figure 5.12. The figures are in line with the results previously discussed. The pressure coefficient shows the largest jump for the flame closest to flashback conditions. The pressure which has not been made dimensionless shows that the largest jump occurs for the flame with the highest bulk velocity and the smallest jump for the flame with the lowest bulk velocity. Taking both figures into consideration the fifth hypothesis can be confirmed. However, the results again do not appear to provide enough information to predict that the flame is near flashback.

Concluding hypothesis:

- *The flashback process will only start after passing a threshold.*

Looking at the presented results it is clear that during the approach to flashback conditions the flame front is becoming increasingly more parallel to radial plane of the pipe. The resulting pressure field therefore has a stronger influence on the incoming flow. Especially at the radial locations near the pipe

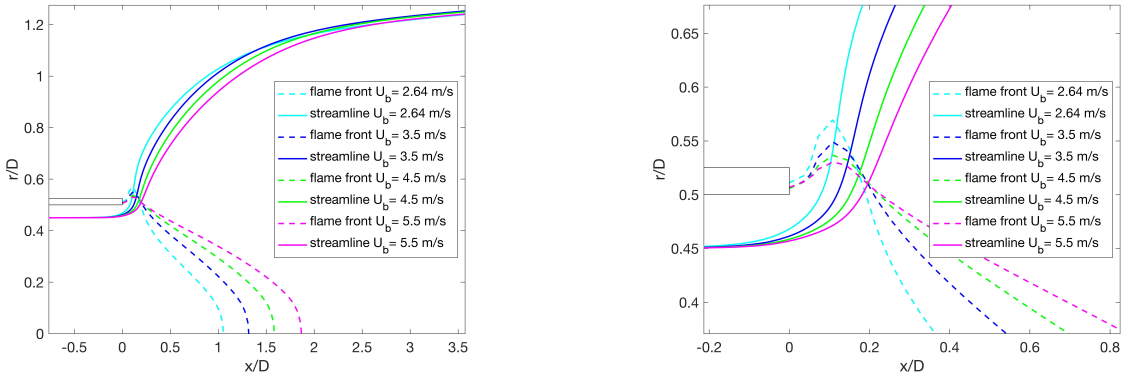

(a) Flame front and streamline locations.

(b) Flame front and streamline locations zoomed in.

Figure 5.11: Flame front and streamline locations overview and zoomed in.

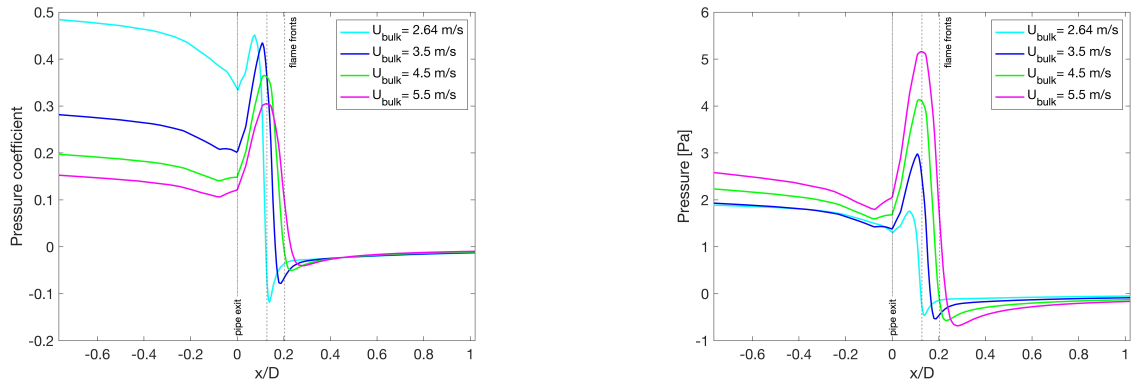

(a) Pressure coefficients along streamline.

(b) Pressure along streamline.

Figure 5.12: Pressure coefficients and pressure along streamline.

wall. However this analysis has not led to a way to predict the flashback in advance. Apparently there is a certain tipping point after which flashback occurs. The flashback process (when modeled using a standard k-epsilon model with enhanced wall treatment in combination with the Zimont turbulent flame closure model) seems to occur after a certain threshold has been passed. When this threshold has been passed the flashback process is self-amplifying. Meaning that due to a decrease in bulk velocity the flame front is increasingly parallel to the radial plane of the pipe outlet, and therefore the isobars of the pressure field are too. That reduces the axial velocity, which in turn causes the flame front to be even more parallel to the radial plane of the exit of the pipe after which the process continues until flashback occurs. The concluding hypothesis can neither be confirmed or denied based on the presented results. However the hypothesis appears to be a logical explanation.

5.2. Experimental validation

In the previous section the flashback process was explained. The analysis led to the conclusion that the model was unable to predict that the flame was near the threshold of flashback. However the model is able to predict the actual flashback process occurring. When using a steady state modeling approach, this means a converged solution can no longer be obtained. If a transient modeling method is employed the flashback can be observed visually. This section is dedicated to validating the numerical results using experimental data. The results in this section including the flame regime map, the flame cone angle and flame induced adverse pressure gradient, obtained using the Zimont turbulent flame closure model in combination a transient standard k-epsilon model are compared to experimental results obtained by Faldella, from [30].

5.2.1. Flame regime map

The flame regime map will be presented for the configurations seen in table 5.1.

	Fuel composition	**Equivalence ratio ϕ (-)**	**Burner tube internal diameter D (mm)**	**Re**
Case 1	100% CH_4	0.8 - 0.9	39.20	4298 - 5052
Case 2	80% CH_4 - 20% H_2	0.8 - 0.9	39.20	5225 - 6451
Case 3	60% CH_4 - 40% H_2	0.8 - 0.9	39.20	6324 - 7017
Case 4	40% CH_4 - 60% H_2	0.7 - 0.9	39.20	3558 - 10482
Case 5	20% CH_4 - 80% H_2	0.6 - 0.9	25.67	4197 - 12166
Case 6	100% H_2	0.6 - 0.9	20.06	8535 - 19167

Table 5.1: Investigated flames

Figure 5.13 shows how bulk velocity near flashback conditions change as a function of the equivalence ratio. The different lines in the graph refer to different fuel mixture compositions. The fuel mixtures range from 100 vol.% methane and 0 vol. % hydrogen, to 0 vol.% methane and 100 vol.% hydrogen with the vol.% hydrogen increasing in steps of 20 volumetric %. The solid lines represent the results obtained using the Zimont Turbulent Flame Closure model, the dashed lines represent the experimentally obtained results.

Firstly, the effect of increasing hydrogen concentration is considered for a given equivalence ratio. When the hydrogen concentration in the fuel increases the flashback propensity increases. Fuels with high vol.% hydrogen are characterized by high flame speeds and less than unity Lewis number which results in a higher ability of the flames to propagate upstream. This effect is clearly seen in the results obtained using the Zimont Turbulent Flame Closure model as well as the experimentally obtained results.

In figure 5.13 it can be observed for both the numerical and the experimental results that an increase in 20% of hydrogen concentration does not cause the same increase in flashback propensity. Which is in line with expectations since the laminar burning velocities increase exponentially with the increase of volumetric hydrogen concentrations in fuel mixtures [39]. The behaviour for the lower volumetric concentrations of hydrogen being 0%, 20% and 40% is similar. When the volumetric concentration hydrogen is increased even further to 60 vol. % hydrogen the change in flashback propensity is also not very strong yet. However at 80%, and in particular at 100% hydrogen content in the fuel, the propensity changes drastically. Furthermore it stands out that the numerical model underestimates the bulk velocity of the incoming mixture for all equivalence ratios for the fuel mixtures with 0, 20, 40, 60 and 80 vol.% hydrogen and for the 100 vol.% hydrogen with an equivalence ratio lower than 0.65. The underestimation of the bulk velocity implies a turbulent flame speed predicted by the Zimont Turbulent Flame Closure model which is lower than the turbulent flame speed observed in the experiments. This underestimation can be the result of an underestimation of the turbulent kinetic energy or the root mean square of the turbulent velocity fluctuations. Which tends to result in an underestimation of the turbulent flame speed [82], since the turbulent flame speed is dependent on the root mean square of the turbulent velocity fluctuations. On the other hand it is seen in the figure that the bulk velocity near

flashback for fuel mixtures containing 100 vol.% hydrogen and having an equivalence ratio higher than approximately 0.65 are overestimated by the Zimont Turbulent Flame Closure model. Which would imply the opposite i.e. an overestimation of the turbulent flame speed.

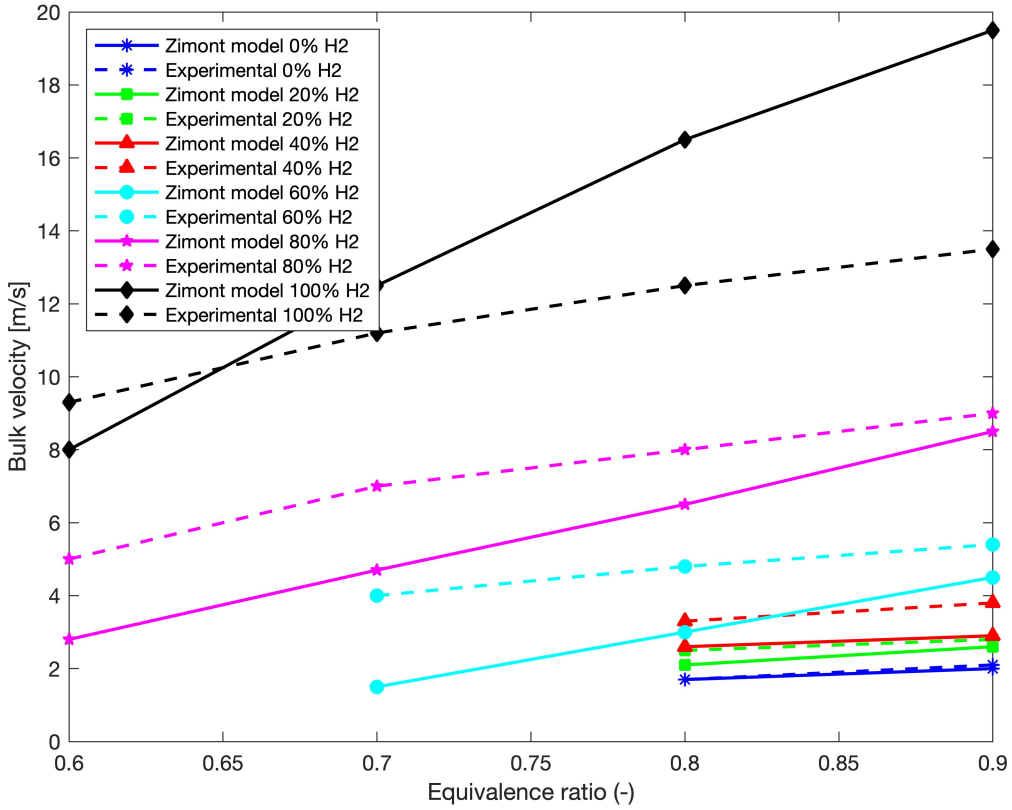

Figure 5.13: Bulk velocity as function of equivalence ratio at flashback conditions, for different fuel composition mixtures. Actual experiments indicated by markers.

5.2.2. Flame cone angle

The flame cone angle is an important parameter since it is related to the acceleration of flow over the flame front. The gas expansion related to the increase in temperature due to combustion affects only the velocity component normal to the flame front. Furthermore the flame cone angle has been used to predict flame flashback by Hoferichter [37], since it has been found to be strongly related to the onset of flashback. Therefore this section is dedicated to the investigation of the flame cone angle. Firstly, it will be explained how the cone angle is defined and calculated. Thereafter, the sensitivity of the cone angle to changes in bulk velocity is evaluated for the different flames. Thirdly, the absolute values of the cone angles determined numerically are compared to the experimentally determined values. And finally, the results will be evaluated while taking the expectations derived from the flame regime map into account.

To calculate the flame cone angle, first the density along the red lines in figure 5.14a (i.e. x/d = 0.2, 0.7 and 1.2) is determined. Next the location r/d on the red lines at which the density equals the full width at half width maximum (FWHM) density, equal to the maximum density divided by 2, is determined. A linearised flame front location is determined by plotting a line through the three points, see the blue line in figure 5.14b. Finally the flame cone angle can be calculated using the gradient of the line, as indicated by the blue arc in the figure. In the figures seen in 5.14 a flame front based on a progress value of approximately 0.2 is shown as an illustration to indicate where the red lines are with respect to the flame front at c = 0.2 and to indicate how the linearised flame front relates to a realistic

flame shape. It should be noted that the described method using the FWHM density to determine to flame cone angle is not dependent on the progress variable at c = 0.2.

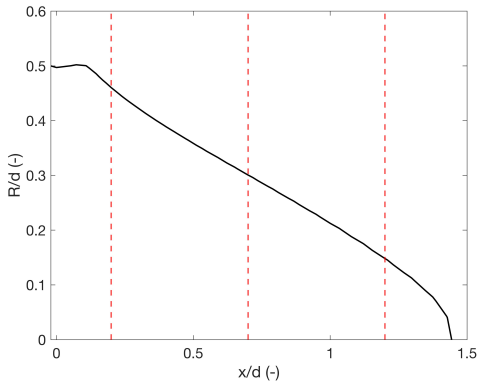

(a) Lines along FWHM density is determined (red lines).

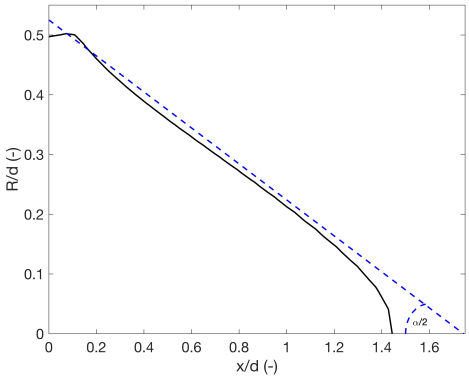

(b) Linearised flame front (blue line) used to determine flame cone angle. Half of flame cone angle (axisymmetric geometry) indicated by blue arc.

Figure 5.14: Flame front angle, the flame front location shown here as an indication is based on a progress variable value of 0.2

The flames for which the flame cone angle has been calculated are listed in table 5.2. The Zimont model is unable to stable (i.e. without flashback occurring) model flames for flame 1 and 2 (both an equivalence ratio of 0.8, 100 vol.% hydrogen and internal diameter of 20.06 mm), therefore no flame cone angles are reported for those flames.

The development of the flame cone angles for flame 3,4 and 5 (all three an equivalence ratio of 0.6, 100 vol.% hydrogen and internal diameter of 25.67 mm) is plotted in figure 5.15 using the previously described linearised flame fronts. It can be observed that the flame cone angle computed using the Zimont flame speed model decreases (resulting in a longer flame cone) for an increase in bulk velocity. However the experimental flame cone angle first increases before it decreases when the bulk velocity is increased.

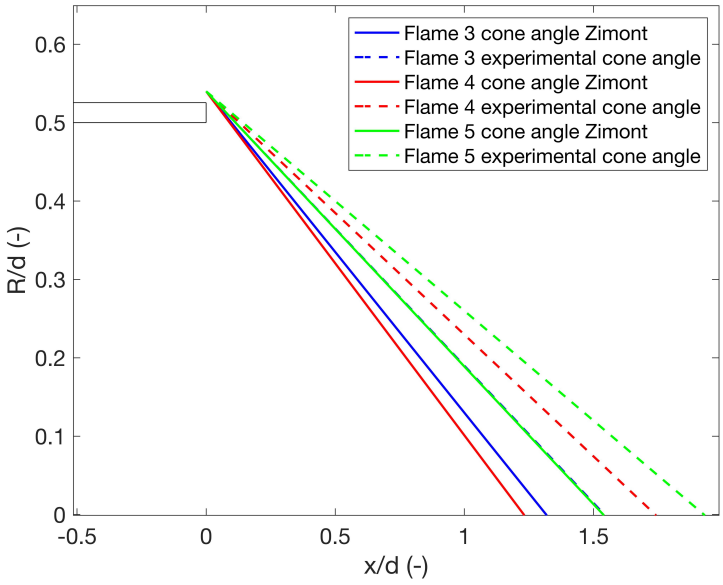

Figure 5.15: Flame cone angles of flames 3, 4 and 5 (100 vol.% hydrogen). Experimental data compared to numerical results.

The development of the flame cone angles for flame 6 and 7 (both an equivalence ratio of 0.8, 60 vol.% hydrogen and internal diameter of 39.20 mm) is plotted in figure 5.16 using linearised flame fronts.

It can be observed that the flame cone angle computed using the Zimont flame speed model increases for an increase in bulk velocity. However an increase in bulk velocity decreases the experimental cone angle.

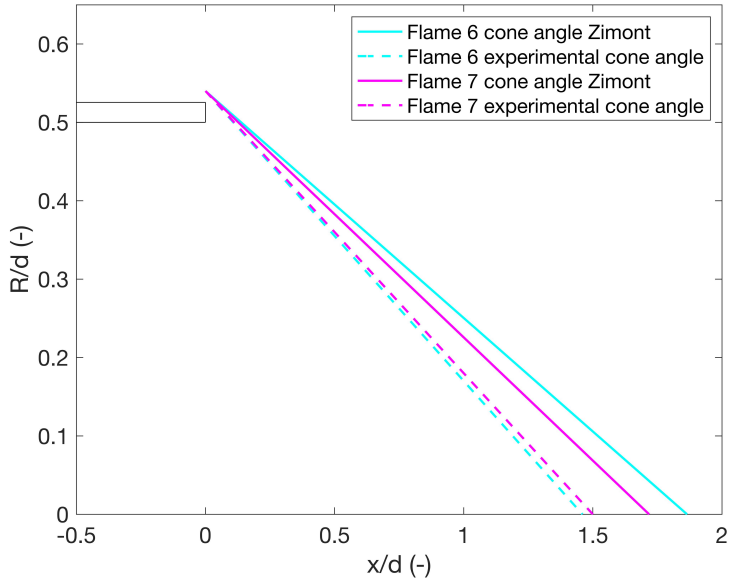

Figure 5.16: Flame cone angles of flames 6 and 7 (60 vol.% hydrogen). Experimental data compared to numerical results.

The development of the flame cone angles for flame 8 and 9 (both an equivalence ratio of 0.6, 80 vol.% hydrogen and internal diameter of 39.20 mm) is plotted in figure 5.17 using the linearised flame fronts. The cone angle decreases when the bulk velocity is increased for both cone angles calculated using the Zimont flame speed model and the experimental results.

So only the flame cone angles of the 80 vol.% hydrogen flames react the same to a change in bulk velocity in both the experiments and the numerical model. The 100 and 60 vol.% hydrogen flames do not react the same in the experiments and the numerical model on a change in bulk velocity. But the flame cone angles of flame 6 and 7 (60 vol.% hydrogen) in the experiments differ only by 1 degree, and in the numerical model the difference is only 2.6 degrees as seen in figure 5.16. So although the model does not predict the trend well, the numerical model does correctly predict that the flame cone angles of flame 6 and 7 are very similar in value.

Looking at the absolute values of the flame cone angles several things stand out. The absolute values of the flame cone angles of the 80 vol.% hydrogen flames determined using the numerical model match the experimentally determined flame cone angles fairly well. For flame 8 the difference is 4.5 degrees and for flame 9 only 3.2 degrees as can also be seen in figure 5.17. Which is satisfactory, especially considering the experimental flame cone angle is determined by means of the Mie-scattering measurements which are filtered with a simple multistep filter in order to reduce the scatter and to produce a smooth curve. The absolute values of the flame cone angles of the 60 vol.% hydrogen flames determined using the numerical model do not match the experimentally determined flame cone angles as well as can be seen in figure 5.16. For flame 6 the difference is 8.3 degrees and for flame 7 the difference is 4.7 degrees. The absolute values of the flame cone angles of the 100 vol.% hydrogen flames determined using the numerical model start to show a significantly greater deviation from the experimentally determined flame cone angles, which can be clearly seen in figure 5.15. The differences are 6, 12.9 and 7.4 degrees for flames 3, 4 and 5 respectively.

The results of the flame regime map in subsection 5.2.1 showed that the bulk velocity near flashback (and the turbulent flame speed) was underestimated for all cases except the 100 vol.% hydrogen flames with an equivalence ratio greater than 0.65 when modeled with the Zimont turbulent flame speed correlation. Therefore one would expect the numerically determined 60 and 80 vol.% hydrogen flames to have longer flame cones with smaller flame cone angles compared to the experimentally determined

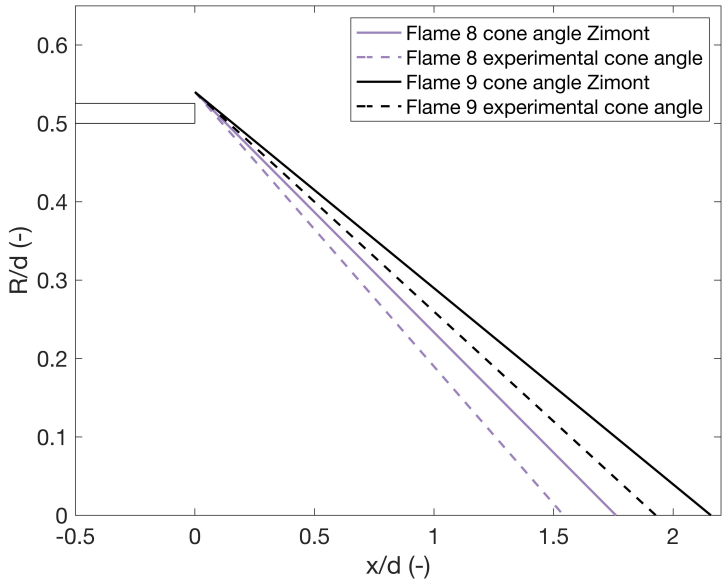

Figure 5.17: Flame cone angles of flames 8 and 9 (80 vol.% hydrogen). Experimental data compared to numerical results.

values. This was confirmed in the results of flame 6, 7, 8 and 9. Following the same logic flames 3, 4 and 5 were expected to show the same behaviour. Yet, the results showed the contrary. The numerically determined flame cone angles all were larger when compared to the experimentally determined values for flames 3, 4 and 5. The 100 vol.% hydrogen flames modeled to construct the flame regime maps and to determine the flame cone angles differ in the used pipe geometries. In case of the flame regime maps an internal pipe diameter of 20.06 mm is used, while an internal pipe diameter of 25.67 mm is used to model flames 3, 4 and 5. As a result the Reynolds number of flames 3, 4 and 5 is approximately 3500 to 7500 higher than the Reynolds number of the flame with an equivalence ratio of 0.6 and 100 vol.% hydrogen in the flame regime map. Since the Zimont turbulent flame speed is highly dependent on the turbulence levels in the flow, as seen in subsection 3.1.4, the increased Reynolds number results in higher turbulent flame speeds. Which explains why flames 3, 4 and 5 are the only flames with shorter cones and larger cone angles than seen in the experiments.

	Burner tube internal diameter, D (mm)	**Re (-)**	**Equivalence ratio, ϕ (-)**	**Bulk velocity, U_b ($\mathbf{m \cdot s^{-1}}$)**	**Fuel composition (-)**	**Flame cone angle experimental $\alpha_{c,exp}$ (°)**	**Flame cone angle Zimont $\alpha_{c,Zimont}$ (°)**
Flame 1	20.06	11310	0.8	11.24	100% H_2	41.6	-
Flame 2	20.06	13315	0.8	13.24	100% H_2	39.6	-
Flame 3	25.67	13310	0.6	9.91	100% H_2	38.6	44.6
Flame 4	25.67	12005	0.6	8.94	100% H_2	34.5	47.4
Flame 5	25.67	16139	0.6	12.02	100% H_2	31.3	38.7
Flame 6	39.20	10557	0.8	4.47	60% H_2	40.6	32.3
Flame 7	39.20	13353	0.8	5.65	60% H_2	39.6	34.9
Flame 8	39.20	11310	0.6	4.91	80% H_2	38.6	34.1
Flame 9	39.20	13805	0.6	6.00	80% H_2	31.3	28.1

Table 5.2: Flame cone angle comparison

5.2.3. Flame induced adverse pressure gradient

The flame induced pressure gradient has experimentally been determined by Faldella [30], employing the Navier-Stokes equations in cylindrical coordinates while assuming the flow to be incompressible and

isothermal and neglecting the viscous terms. Furthermore the momentum equation in axial direction has been made dimensionless. In the case that the contribution of both the Reynolds stresses are close to zero, the pressure gradient balances the advection term in axial direction. This implies that this approach to determine the flame induced pressure gradient is only valid up to the location x/d where the Reynolds stress gradients are no longer equal to zero. This corresponds to x/d = 0.35 at r = 0.3 d, up to x/d = 0.45 at r = 0.2d, up to x/d = 0.6 at r = 0.1d and up to x/d = 0.70 at r/d = 0 for the experimental results, as indicated by Faldella [30].

Since there is only experimental data available up to the previously mentioned locations along the radial locations, the numerical data will only be presented up to these corresponding locations. The equation seen in equation 5.4, which is the pressure term in the dimensionless Navier-Stokes equations in cylindrical coordinates, has been implemented in the CFD software to determine the dimensionless pressure gradient.

$$\frac{dp^*}{dx^*} = \frac{dp}{dx}\frac{D}{\rho U_b^2} \tag{5.4}$$

In which x is the location along the axis, D is the internal pipe diameter, ρ is the mixture density and U_b is the bulk velocity.

The flame induced pressure gradient has only been determined experimentally by Faldella [30] for flame 1 and 2 seen in table 5.2. Flame 1 is seen as an 'unstable' flame since it is very close to flashback. Flame 2 is seen as a 'stable' flame since it is not burning near flashback conditions. Unfortunately the Zimont model is unable to create a stable flame for flame 1 and 2 (the flames are past the flashback threshold), since the model overestimates the bulk velocity near flashback for the 100 vol.% hydrogen cases with an equivalence ratio greater than 0.65. Therefore four other flames are used to compare the numerical and experimental flame induced pressure gradient. The flames used are listed in table 5.3. All the extra modeled flames use the same geometry as flame 1 and 2, and a fuel composition of 100 vol.% hydrogen.

	Burner tube internal diameter, D (mm)	**Re (-)**	**Equivalence ratio, ϕ (-)**	**Bulk velocity, U_b ($\mathbf{m \cdot s^{-1}}$)**	**Fuel composition (-)**	**Flame cone angle Zimont $\alpha_{c,Zimont}$**
Flame 10	20.06	11993	0.6	11.24	100% H2	33.5
Flame 11	20.06	14127	0.6	13.24	100% H2	28.4
Flame 12	20.06	16650	0.8	16.5	100% H2	30.8
Flame 13	20.06	18668	0.8	18.5	100% H2	31.1

Table 5.3: Extra modeled flames to compare the flame induced pressure gradient

Flame 10 and 11 are two flames with the same bulk velocities as flame 1 and 2, however instead of an equivalence ratio of 0.8 an equivalence ratio of 0.6 is used. Since, as seen in figure 5.13, this the only equivalence ratio in the studied range for which a stable flame can be modeled at the bulk velocities of flame 1 and 2 using the Zimont model. Flame 12 and 13 are two flames with the same equivalence ratio as flame 1 and 2. However higher bulk velocities are used. Flame 12 is the 'unstable' flame based on the Zimont model since this flame is close to flashback at the corresponding bulk velocity. Flame 13 is the 'stable' flame, which is not operating near flashback conditions. The comparison of the dimensionless pressure gradients is seen in figures 5.18 and 5.19.

Before considering the results seen in figures 5.18 and 5.19 it should be noted that the flame shapes of the flames modeled using the Zimont model differ from the real world, experimental flame shapes. The difference in flame shape is exemplified by the difference in flame cone angles between flames 1, 10 and 12 and the flames 2, 11 and 13. The difference in flame shape results in a different development of the pressure gradient along the distance x/d from the pipe exit.

Looking at figure 5.18 it can be observed that the dimensionless pressure gradient of the 'unstable' flames 10 and 12 are under-predicted by the Zimont model with respect to the experimental results. The pressure gradient of the 'stable' flame 11 matches the experimental pressure gradient of flame 2

in order of magnitude, but the location at which the pressure gradient shows a minimum and maximum differs. This can probably be attributed to the difference in flame shape. On the other hand the pressure gradient of flame 13 is overestimated by the Zimont model, the maximum of this pressure gradient is even higher than the 'unstable' flame. this might be due to the fact that the 'stable' flame has a larger cone angle. The larger cone angle then causes a larger increase in velocity magnitude across the flame front and therefore a higher adverse pressure gradient. Furthermore a larger cone angle means a smaller distance between the burner outlet and the flame front. Which results in a stronger effect of the burner walls hampering the flow deflection.

Looking at figure 5.19 it can be observed that the dimensionless pressure gradient along all the radial locations of both the 'unstable' flames 10 and 12 is under-predicted by the Zimont model with respect to the experimental results. An under-predicted adverse pressure gradient implies under-predicted turbulent kinetic energy which tends to decrease the turbulent flame speed [82]. That results in a smaller increase in velocity magnitude across the flame front. This is in line with the observed under-prediction of the bulk velocity near flashback for a 100 vol.% hydrogen flame with an equivalence ratio of 0.6 as seen in figure 5.13. However, the bulk velocity near flashback conditions is actually over-predicted by the Zimont model for a flame with an equivalence ratio of 0.8 and 100 vol.% hydrogen, such as flame 12. This gives the impression that there are other factors that influence the turbulent flame speed predicted by the Zimont Turbulent Flame Closure model. Such as the non-linear relation between the laminar burning velocities and volumetric hydrogen content or the flame-flow interaction.

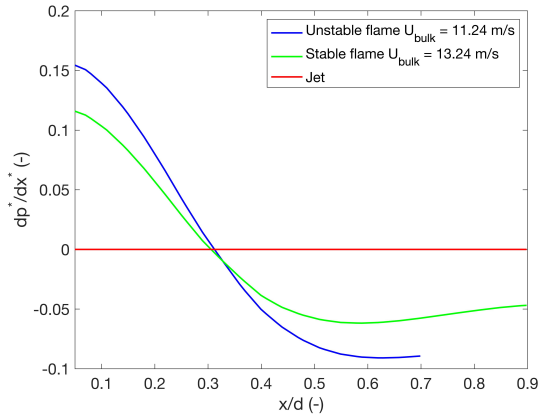

(a) Flame 10 and 11, determined using Zimont Turbulent Flame closure model, ϕ = 0.6

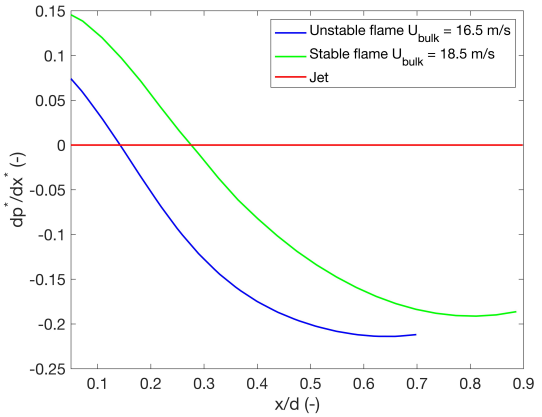

(b) Flame 12 and 13, determined using Zimont Turbulent Flame closure model, ϕ = 0.8

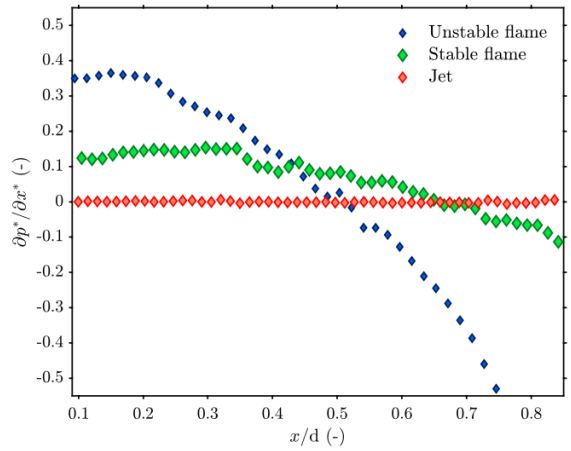

(c) Flame 1 and 2, determined experimentally, ϕ = 0.8, image taken from [30]

Figure 5.18: Comparison of pressure gradient in axial direction of flame 10 and 11 in table 5.3 and a jet, of flame 12 and 13 in table 5.3 and a jet, and flame 1 and 2 in table 5.2 and a jet.

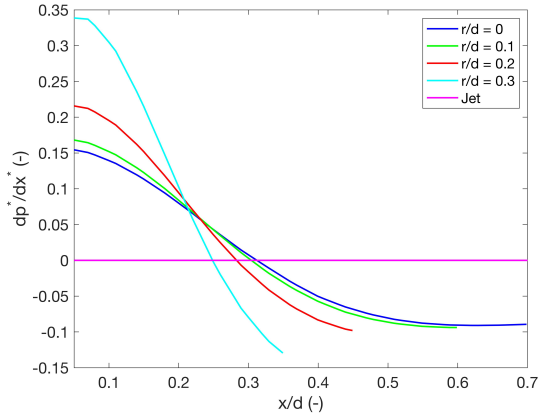

(a) Flame 10, determined using Zimont Turbulent Flame closure model, ϕ = 0.6

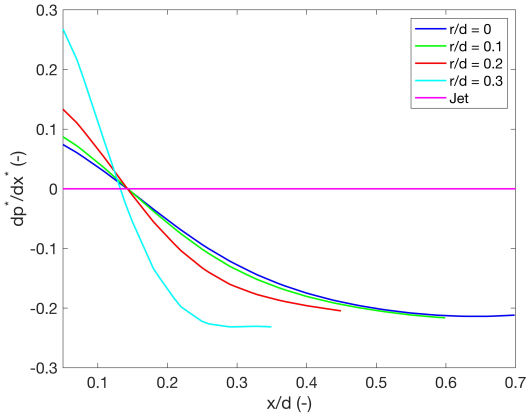

(b) Flame 12, determined using Zimont Turbulent Flame closure model, ϕ = 0.8

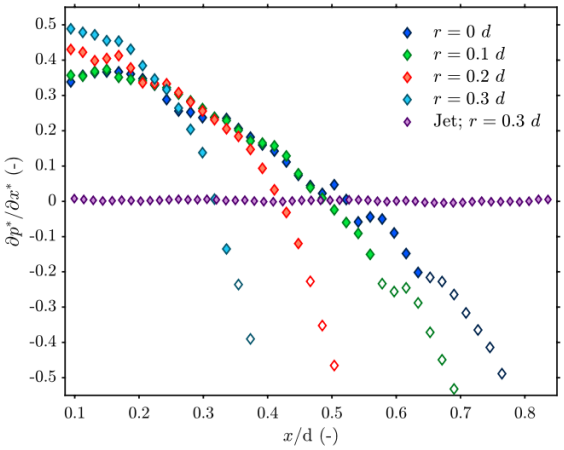

(c) Flame 1, determined experimentally, ϕ = 0.8, image taken from [30]

Figure 5.19: Comparison of pressure gradient in axial direction of flame 10 in table 5.3, flame 12 in table 5.3 and flame 1 in table 5.2. Each curve is computed at a different radial location.

5.3. Evaluation of turbulent flame speed correlations

In this section the results of the implementation of three turbulent flame speed correlations selected in subsection 3.2.6 will be evaluated for three different flames. For the first two flames only numerical data will be compared, the data will be presented in small sub topics with a short conclusion for the specific flame. For the last flame numerical data will be evaluated in the same way, besides also experimental data will be evaluated. Finally, an overall conclusion will be formulated summarizing the results.

As a flame front propagates, unburned fuel is ignited, converting unburned premixed fuel to burned products. The combustion model used in this study considers the reacting flow field to be divided into regions of burned and unburned species, separated by the flame sheet. The transition of the unburned region to the burned region is described by the progress variable. As described earlier, the transport equation for the progress variable is given by:

$$\frac{\partial}{\partial t}(\rho c) + \frac{\partial}{\partial x_i}(\rho u_i c) = \frac{\partial}{\partial x_i}\left(\rho D \frac{\partial c}{\partial x_i}\right) + \dot{\omega}_c \tag{5.5}$$

The progression of the reaction corresponds to the propagation of the flame front. And as described earlier the chemical reaction rate or the source term of c is defined as:

$$\dot{\omega}_c = \rho_u S_t |\nabla \tilde{c}| \tag{5.6}$$

The aim of this section is evaluating the results of implementing different correlations for S_t. The source term (more information on the source term can be found in subsection 3.1.3) is dependent on the turbulent flame speed and the gradient of the progress variable, as seen in equation 5.6. Meaning the turbulent flame speed should be evaluated while taking the gradient of the progress variable in consideration as well.

The standard k-epsilon model with enhanced wall treatment in combination with the Zimont turbulent flame closure model is capable of predicting the occurrence of flashback. However as seen in section 5.2 there is definitely room for improvement, especially for the fuels with higher volumetric hydrogen concentrations. High hydrogen concentration fuels are characterized by high flame speeds and, if sufficiently lean, by a Lewis number lower than 1. In combination with differential diffusion this leads to the thermal diffusive instability [73]. The Lewis number lower than 1 is related to unbalanced thermal and mass diffusion. While differential diffusion occurs when the fuel and oxidizer have different species diffusion, leading to locally different equivalence ratios. The Zimont turbulent flame speed correlation which is implemented in Fluent as standard, does not include Lewis number effects and is not optimized for flames influenced by such effects. Therefore an improvement could be realized by including the effect of the Lewis number in the correlations used to model the turbulent flame speed. This was also concluded in section 3.2 and multiple correlations for the turbulent flame speed provided in literature were evaluated. Furthermore the turbulence level with respect to the unstretched laminar flame speed defined as the range of u'/S_L^0 values for which a correlation is determined was considered. This led to the selection of two promising correlations to model hydrogen-methane flames with high hydrogen content. The correlations are a correlation derived by Muppala, Manickam and Dinkelacker seen in equation 5.8 and a correlation derived by Cai et al. seen in equation 5.9.

$$S_t = 0.52 {u'}^{3/4} {S_L^0}^{1/2} l_t^{1/4} \alpha^{-1/2}, \text{(Zimont.[88])} \tag{5.7}$$

$$S_t = S_L^0 + \frac{0.46}{exp\left(Le_{eff} - 1\right)} \left(\frac{l_t}{\nu}\right)^{0.25} {u'}^{0.55} {S_L^0}^{0.7} \left(\frac{p}{p_0}\right)^{0.2}, \text{(Dinkelacker et al.[60])} \tag{5.8}$$

$$S_{t,c=0.5} = S_L^0 + \frac{0.164}{Le_{eff}^{1.32}} \left(\frac{u' l_t}{\nu}\right)^{0.66} S_L^0, \text{(Cai et al.[16])} \tag{5.9}$$

As mentioned ,the aim of this section is to determine whether the selected correlations for the turbulent flame speed lead to an improvement with respect to the Zimont correlation, seen in equation 5.7. To evaluate the correlations they were implemented in Fluent and used in combination with the standard k-epsilon model just as the Zimont correlation, the used User Defined Functions can be found

in the appendix in section A.1. To ensure the used implementation method is correct, the Zimont correlation has also been implemented in Fluent using the same routines. Both the standard Zimont correlation provided in Fluent and the Zimont correlation implemented as a User Defined Function have been used to model flame 9. The comparison of the velocity fields and the used code can be found in the Appendix in section A.2. The results are near identical, meaning the method used to implement the correlations is correct.

Ideally one would compare the modeled results with experimental results. However, to be able to make that comparison, all three models must be able to model the flame for which experimental results are available. After some evaluation it turned out that of the flames for which Faldella [30] published experimental results, only flame 9 from table 5.2 could be modeled by all three correlations. Therefore this is the only flame for which the numerical results will be compared to experimental data. Furthermore two extra flames are modelled which can be modeled by all three correlations, an overview of the three flames is listed in table 5.4. As described in chapter 3 the method of calculating the effective Lewis number depends on the used model. The used approach to calculate the effective Lewis number in case of the Dinkelacker et al. correlation has been explained in subsection 3.1.5 and the approach if the Cai et al. correlation is employed has been explained in subsection 3.2.4. The resulting effective Lewis numbers for the modeled flames are also listed in table 5.4. The used fuel compositions are 20, 60 and 80 vol.% hydrogen. The flames with 20 and 60 vol.% hydrogen have an equivalence ratio of 0.8 and the flame with 80 vol.% hydrogen has an equivalence ratio of 0.6. Since the flame with 80 vol.% hydrogen and an equivalence ratio of 0.6 is the only flame that can be compared to experimental results, it was decided to use this 80 vol.% hydrogen flame instead of a flame with a higher equivalence ratio.

	Burner tube internal diameter, d	**Re (-)**	**Equivalence ratio,** ϕ	**Bulk velocity,** U_b $(\mathbf{m \cdot s^{-1}})$	**Unstretched Laminar flame speed,** S_L^0 $(\mathbf{m \cdot s^{-1}})$	**Fuel composition (-)**	$\mathbf{Le_{eff,AFSW}}$ **(-)**	$\mathbf{Le_{eff,Cai}}$ **(-)**
Flame 14	39.20	7464	0.8	3.00	0.2763	20% H_2	0.655	0.96
Flame 15	39.20	15277	0.8	6.50	0.4402	60% H_2	0.402	0.92
Flame 9	39.20	13805	0.6	6.00	0.4124	80% H_2	0.337	0.7

Table 5.4: Extra modeled flames to compare the turbulent flame speed correlations

Up front a simple analysis can be performed to predict how the turbulent flame speed correlations are expected to behave for the flames. The expected influence of certain flow and fuel properties on the equations presented in 5.7, 5.8 and 5.9 is evaluated. The focus is on the influence of variables which are recurring and differing in the correlations. That are S_L^0, u', l_t and Le_{eff}. The values of l_t and u' will be evaluated extensively later in this section as they are dependent on the pipe geometry, bulk velocity of the incoming flow and the velocity magnitude increase over the flame front. Therefore only the expected influence of S_L^0 and Le_{eff} will be evaluated here. Looking at equations 5.7, 5.8 and 5.9 it can be seen that the power with which S_L^0 is raised differs. In equation 5.7 S_L^0 is raised to the power of 0.5, in equation 5.8 to the power of 0.7 and in 5.9 to the power of 1. Since the unstretched laminar flame speed has a value lower than unity for all three flames, the factor by which is multiplied increases as the exponent decreases. It should be noted that in the correlations proposed by Dinkelacker et al. and Cai et al. the unstretched laminar flame speed is separately added to the equation in contrary to the Zimont correlation. The second factor to consider is the effective Lewis number, of course the Lewis number effect is not included in the Zimont correlation. In the correlation proposed by Dinkelacker et al. the second term of the right side of the equation is multiplied by a factor $1/\left(Le_{eff} - 1\right)$ which is equal to 1.412, 1.818 and 1.941 for flame 14, 15 and 9 respectively. Meaning that the inclusion of the effective Lewis number is expected to have a significant influence on the calculated turbulent flame speed of all three flames. In the correlation proposed by Cai et al, the second term of the right side of the equation equation is multiplied by $1/Le_{eff}^{1.32}$, equal to 1.055, 1.116 and 1.601 for flame 14, 15 and 9 respectively. Which means that the inclusion of the effective Lewis number is only expected to have a significant influence on flame 9.

In the remainder of this section the results of the implementation of the turbulent flame speed correlations will be evaluated and compared for all three flames, therefore multiple quantities have been

selected. Which are the contours of; the velocity field, the root mean square turbulent velocity fluctuations and the turbulent dissipation rate all including velocity direction vectors and an iso-line indicating a flame front location based on a progress variable value of 0.2. The velocity field is scaled with the bulk velocity and the radial coordinates are scaled with the tube inner diameter d. Also included are the turbulent flame speed contours including two iso-lines based on progress variable values of 0.1 and 0.9, which help understanding the contribution to the source term. Also included is the source term of the progress variable plotted along the pipe axis. And furthermore the normalized turbulent flame speed along the same flame front location is evaluated. The normalized turbulent flame speed is plotted against the normalized root mean square of the turbulent velocity fluctuations u'/S_L^0 and the integral length scale l_t.

The combination of these quantities provides a strong framework to evaluate the influence of the implementation of different turbulent flame speed correlations on the flow field and progress variable source term, while at the same time the underlying factors that are driving the changes in the turbulent flame speed correlations can be identified. For example; the flame front location gives an indication of the flame cone angle and curvature of the flame front. This is useful to gain better understanding in the acceleration of flow across the flame front. As previously explained, the unburned gas velocity component is axially directed at the tube outlet. Once the mixture reaches the flame front the combustion process expands the gas. This expansion results in an increase of the velocity component normal to the flame front. Using an one dimensional balance equation it can be seen that the increase in velocity has to be equal to the ratio of the density or temperature across the flame front. This simplified analysis only holds for a flat flame front. However the analysis can be used to investigate the modeled results, since a larger angle results in a larger increase in velocity across the flame front. Another aspect that can be investigated using the velocity field and the flame front location is the location at which the flames are anchored. Which is interesting, since the results described in subsection 5.1.1 seem to suggest that a smaller distance from the tube outlet to the average flame front location results in a stronger effect of the burner walls hampering the flow deflection. Furthermore a flame anchored closer to the pipe outlet leaves less room for leakage flow. Leakage flow flows between the pipe wall and the position at which the flame is anchored without being ignited. It ignites downstream of the flame front. This example shows how the flow field can be evaluated, but to gain a better understanding of the actual causes of the differences the combination of the described quantities is necessary.

5.3.1. Flame 14: Zimont vs Dinkelacker vs Cai

Normalized velocity field

Firstly the results of flame 14 will be considered. Flame 14 uses the 39.2 mm inner diameter burner, a bulk velocity of 3.00 m/s, an equivalence ratio of 0.8 and the fuel composition is 20 vol.% hydrogen. When comparing figures 5.20 and 5.21 it can be seen that the flames modeled using the correlation by Dinkelacker et al. and Cai et al. both have a shorter cone and a larger cone angle than the flame modeled using the Zimont correlation. This difference in cone angle leads to a higher acceleration of the flow across the flame front, as can be seen by considering the contour of the normalized velocity in the region just above the flame front. Looking at figure 5.20, the left side modeled using the Zimont correlation shows a region above the flame front where the velocity magnitude (ratio of local velocity and bulk velocity) is ranging from 1.7 to 2, while the right side modeled using the Dinkelacker et al. correlation shows a region above the flame front which is much larger and ranges from approximately 2 tot 2.3. Furthermore, it can be seen that the flame modeled using the Dinkelacker et al. correlation accelerates the flow in front of the flame front significantly. The explanation for this effect will be discussed in the next paragraph on the turbulent flame speed. Due to this acceleration upstream the boundary layers thickens and the velocity gradient increases, the average bulk velocity however remains the same. The higher acceleration when modeling the flame with the correlation by Dinkelacker et al. expresses itself in an increased velocity magnitude, an increased size of the higher velocity region and a suction effect on the incoming flow. The right side of figure 5.21 modeled using the Cai et al. correlation shows that the region above the flame front is enlarged but the velocity magnitude ranges from approximately 1.7 to 2, similar to the left side modeled using the Zimont correlation. Meaning the higher acceleration when modeling the flame with the correlation by Cai et al. expresses mostly as an increase in size of the higher velocity region. The flame modeled using the correlation by Cai et al. also has a flame front which is more concave than the flame modeled using the correlation by Dinkelacker et al. Furthermore the flame modeled using the correlation by Dinkelacker et al. is anchored the closest to the tube outlet, subsequently the flame modeled using the Zimont correlation and the flame modeled using the correlation by Cai et al. is anchored the furthest away from the tube outlet.

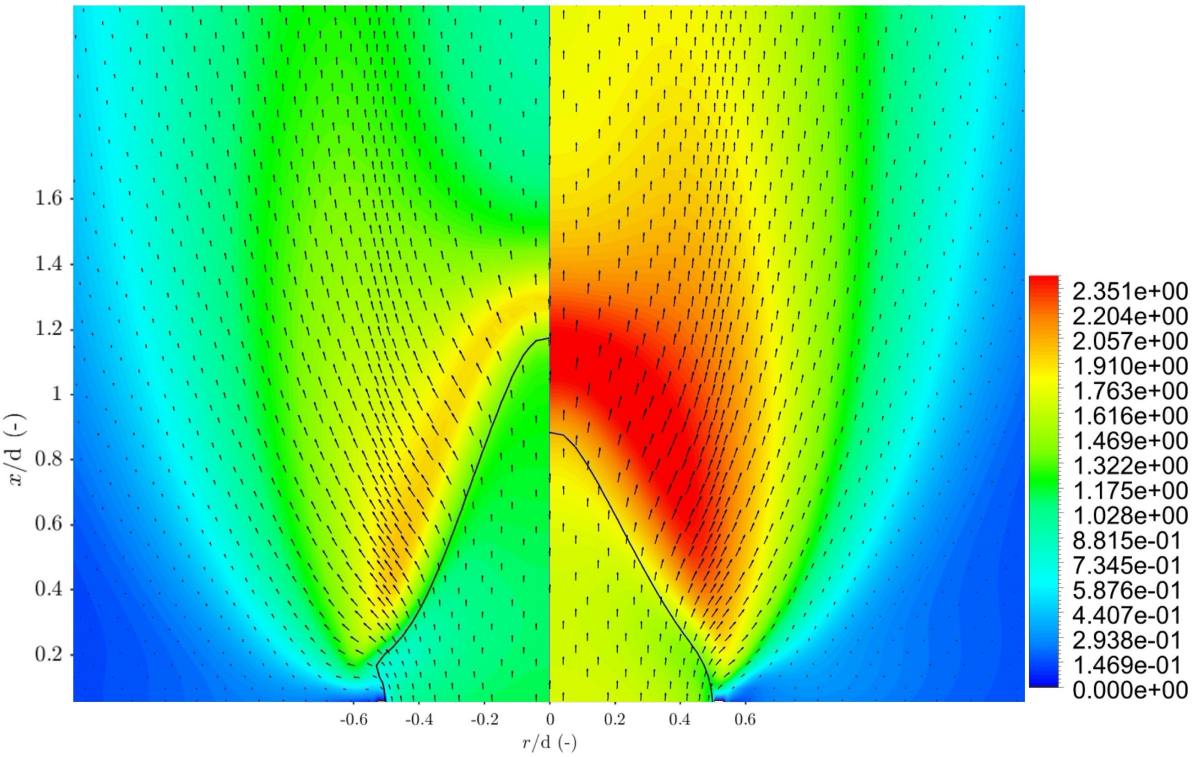

Figure 5.20: Comparison of velocity field u/U_b and flame front location corresponding to c = 0.2 for flame 14. Turbulent flame speed relation: Left hand side; Zimont and right hand side; Dinkelacker et al.

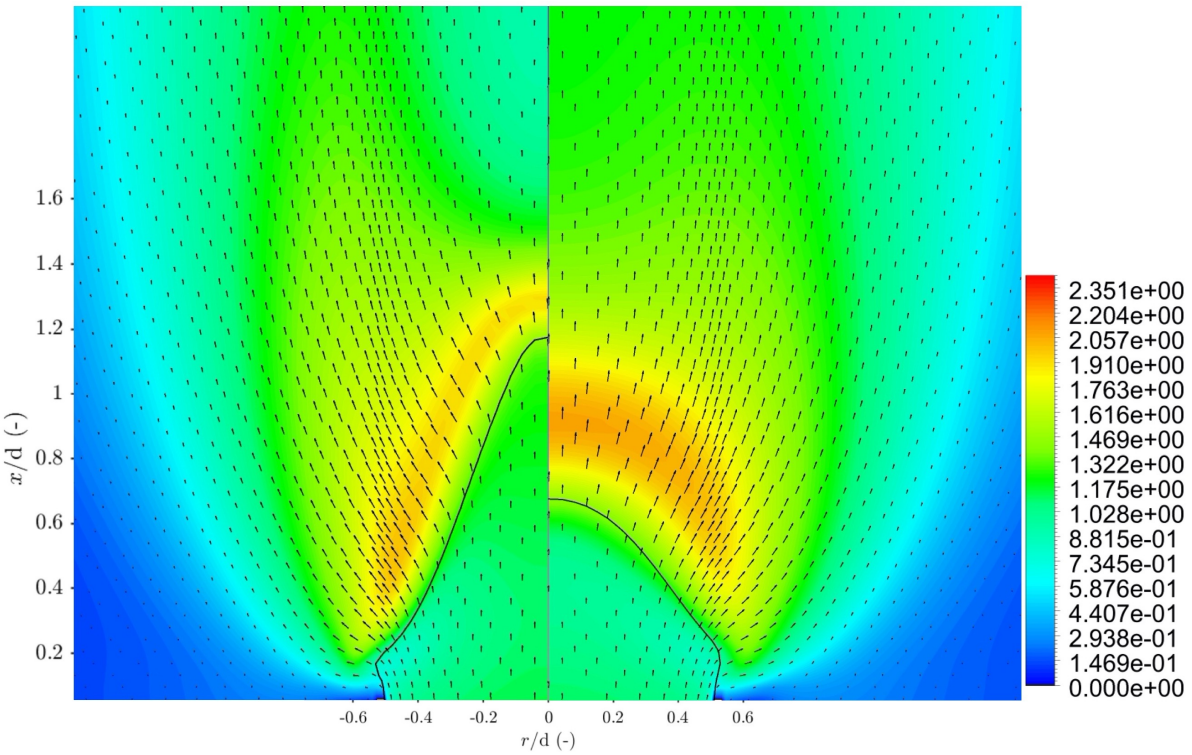

Figure 5.21: Comparison of velocity field u/U_b and flame front location corresponding to c = 0.2 for flame 14. Turbulent flame speed relation: Left hand side; Zimont and right hand side; Cai et al.

Turbulent flame speed and source term

The turbulent flame speed should be evaluated while taking the gradient of the progress variable in consideration as well. Therefore the contours of the turbulent flame speed are plotted together with two iso-lines of the progress variable with values of 0.1 and 0.9. The gradient of the progress variable is negligible outside this region. Looking at figures 5.23 and 5.24 it stands out that the iso-lines are separated by a larger distance in case of the new correlations, meaning the gradient is smaller. Therefore a higher turbulent flame speed with respect to the case modeled using the Zimont correlation will be compensated in the source term by a smaller gradient. Another thing that stands out is that in the case modeled using the Dinkelacker et al. correlation, the iso-line corresponding to the progress variable of 0.1 lies upstream of the area where the turbulent flame speed starts to increase significantly. While for the cases modeled using the other two correlations, the iso-lines closely follow the light blue transition area where the turbulent flame speeds starts to increase. Considering equation 5.5, the reason for the increased progress variable upstream should be caused by turbulent diffusion. Since the progress variable prescribes the transition from an unburned to a burned state it is associated with the heat release and expansion of the gas. The heat release ensures that an upwards fluctuation in c will be associated with an upwards fluctuation in u. Or in other words, the increased progress variable due to turbulent diffusion accelerates the flow upstream of the flame. Which explains the suction effect of the flame seen in the normalized velocity field in figure 5.23. For all cases the maximum in turbulent flame speed is observed near the location r/d = 0.6 and x/d = 0.4. However this is outside of the region between the iso-lines of the progress variable and therefore does not contribute to the production rate of the progress variable. Furthermore it can be seen that the observed values of the turbulent flame speed are fairly similar for all cases. Although the highest turbulent flame speed is observed for the case modeled using the Dinkelacker et al. correlation, seen on the right side of figure 5.23. And the lowest turbulent flame speed is observed for the case modeled using the Cai et al. correlation, seen on the right side of figure 5.24. Both cases modeled using the correlation by Dinkelacker et al. and Cai et al. show a larger area of high turbulent flame speed (red region) compared to the case modeled using the Zimont correlation. Additionally, the turbulent flame speed observed between the iso-lines has values of approximately 0.3 to 1.4 m/s in case of the Dinkelacker et al. correlation, 0.5 to 1.3 in case of the Cai et al. correlation, while this is 0.7 to 1 m/s in case of the Zimont correlation. Although it should be noted that a small region located at x/d = 0.3 and r/d = 0.5 has a maximum value of 1.5 m/s in case of the Zimont correlation. Another thing that stands out is the region of higher values of the turbulent flame speed downstream of the flame front along the center line, r/d = 0. This region is observed around x/d = 1.4 for both the Zimont en Dinkelacker et al. correlations and around x/d = 1.2 for the Cai et al. correlation. This high turbulent flame speed region is more pronounced in the cases modeled using the new correlations and therefore has a stronger influence on the source term.

To evaluate the combined effect of the greater distance between the iso-lines and the different observed turbulent flame speed for the cases modeled using the new correlations, the source term is plotted along the pipe axis in figure 5.22. Along the axis, the source terms modeled using the new correlations have values much lower than the values observed in the case modeled using the Zimont correlation. Another difference is the length of the distance x/d where the source term is not equal to zero. The source term modeled with the new correlations is present in a broader area, which is in line with the greater distance between the iso-lines.

The shorter cone length and the increase in velocity magnitude observed in figures 5.20 and 5.21 for the cases modeled with the new correlations can be attributed to a combination of factors. For this flame all three correlations result in similar turbulent flame speed values, but the maxima of the source terms modeled with the new correlations are lower than the maximum of the source term modeled with the Zimont correlation, as seen in figure 5.22. The main difference is that the iso-lines corresponding to c = 0.1 and c = 0.9 are separated by a larger distance in case of the new correlations. Resulting in a smaller gradient, but in combination with the higher turbulent flame speed values this leads to a larger area where the flow is affected. Another important factor is the increased progress variable upstream of the flame due to turbulent diffusion in the case modeled the Dinkelacker et al. correlation.

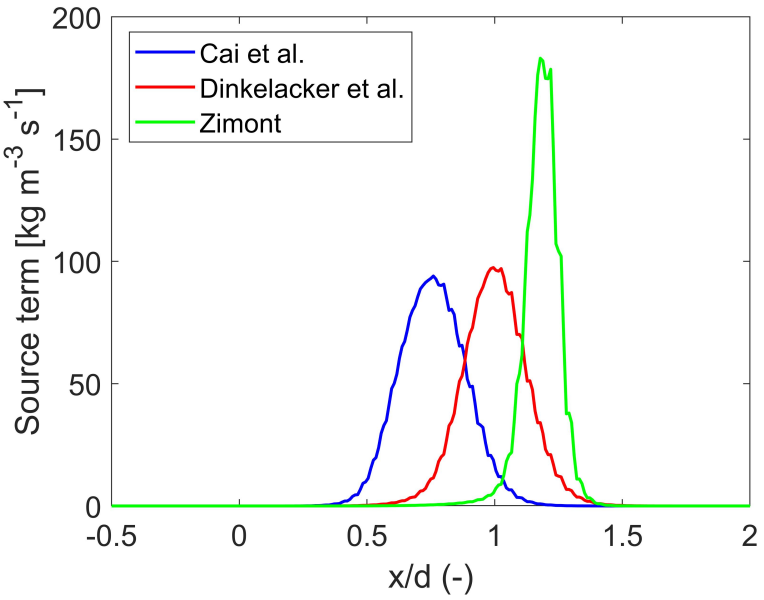

Figure 5.22: Comparison of the source term along the pipe axis for flame 14. Data generated using Fluent.

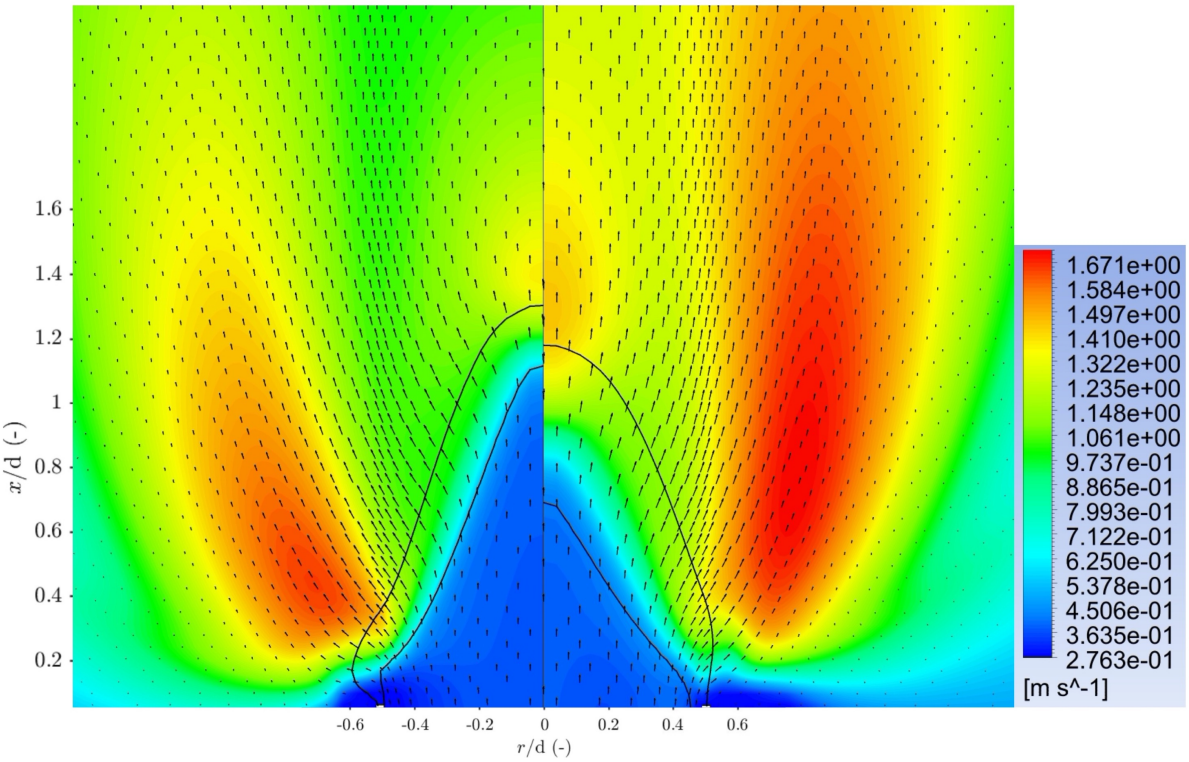

Figure 5.23: Comparison of turbulent flame speed contours, including progress variable isocontours corresponding to c = 0.1 and 0.9 and flow velocity vector field for flame 14. Turbulent flame speed relation: Left hand side; Zimont and right hand side; Dinkelacker et al.

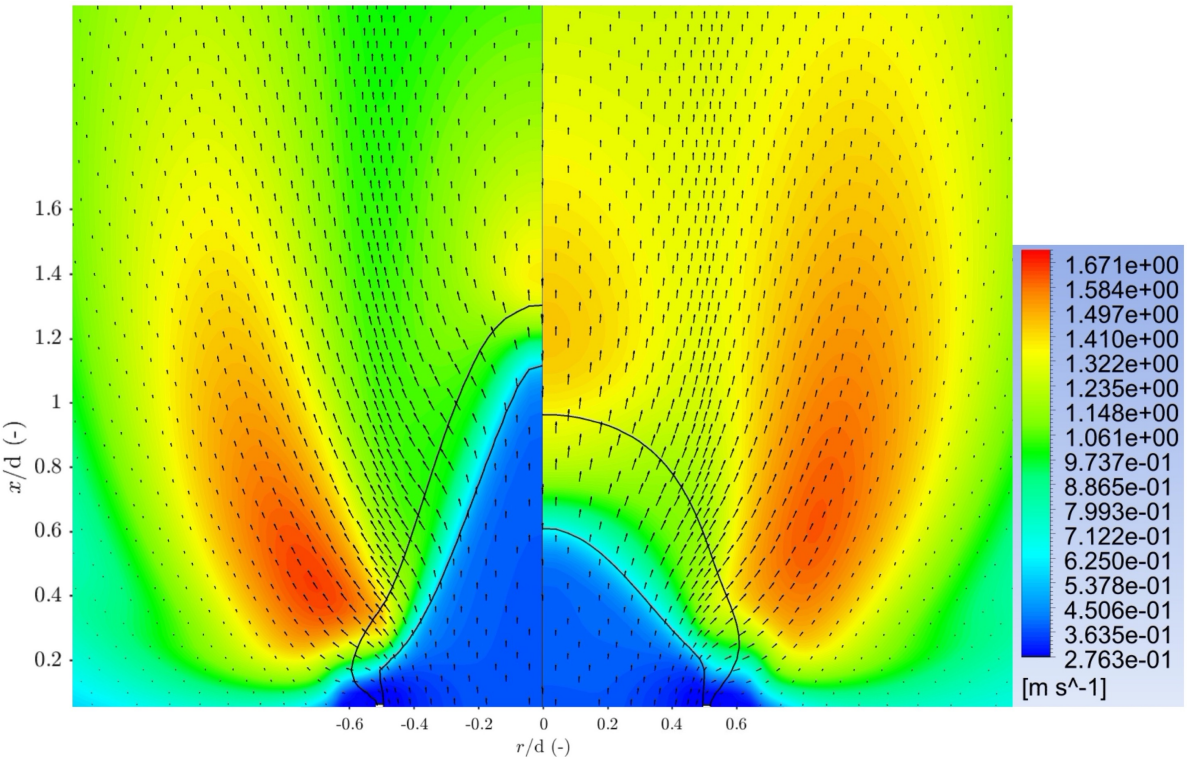

Figure 5.24: Comparison of turbulent flame speed contours, including progress variable isocontours corresponding to c = 0.1 and 0.9 and flow velocity vector field for flame 14. Turbulent flame speed relation: Left hand side; Zimont and right hand side; Cai et al.

Root mean square turbulent velocity fluctuations and turbulent dissipation rate
Although the turbulent flame speed only affects the chemical source term if the gradient of the progress variable is non zero, or in other words within the region where the progress variable transitions from 0 to 1. The turbulent flame speed can be evaluated outside this region. This is helpful to gain insight in the driving factors causing the difference in results using the new turbulent flame speed correlations. As earlier described, the turbulent flame speed is influenced by the root mean square of the turbulent velocity fluctuations u' and the integral length scale l_t. The contours of the u' values are plotted in figures 5.25 and 5.26. On the right side of figure 5.25 it can be seen that the correlation by Dinkelacker et al. results in a much larger area (above r/d = 0.6) of high u' values compared to the flame modeled using the Zimont correlation and both have similar maximum values. On the right side of figure 5.26 it can be seen that the u' values modeled using the Cai et al. correlation in the area above r/d = 0.6 are lower than the values observed on the left side of the figure. Another thing that stands out is the region of high u' values near the location x/d = 1.4 along the center line in the case modeled using the Zimont correlation. This region with high values is not present in the two other cases. The contours of the turbulent dissipation rate ϵ are plotted in figures 5.27 and 5.28. For clarification $l_t \sim k^{3/2}/\epsilon$. Meaning lower values of ϵ result in higher values of l_t. The comparison of the flame modeled using Zimont and Dinkelacker et al. correlations in figure 5.27 shows that similar values are observed. However the flame modeled using the Zimont correlation shows a maximum along the center line near the location x/d = 1.4. This maximum decreases the integral length scale and compensates for the high values of u' seen near the same location. Explaining why a less pronounced high turbulent flame speed region is observed downstream of the flame front along the center line when modeling the flame with the Zimont correlation. Furthermore it can be seen on the right side of figure 5.28 that much lower values for ϵ are observed above the area r/d = 0.6. Which implies higher turbulent length scales. This explains the increased turbulent flame speed and size of the higher turbulent flame speed area, despite the lower observed values for u'.

Another influence of the root mean square velocity fluctuations that should be considered is the fact that is has a lower value in the vicinity of the wall due to the lower flow velocity near the wall and the absence of turbulence fluctuations at the wall. This means that the turbulent flame speed is lower near the wall, and therefore the flame anchors more upstream at a location where the value of u' increases again. If u' is raised to a lower power this effect should be weaker. Therefore the correlation proposed by Dinkelacker et al. results in a flame which anchors very close to the pipe outlet. As a results there is less room for leakage flow and a stronger effect of the burner walls hampering the flow deflection.

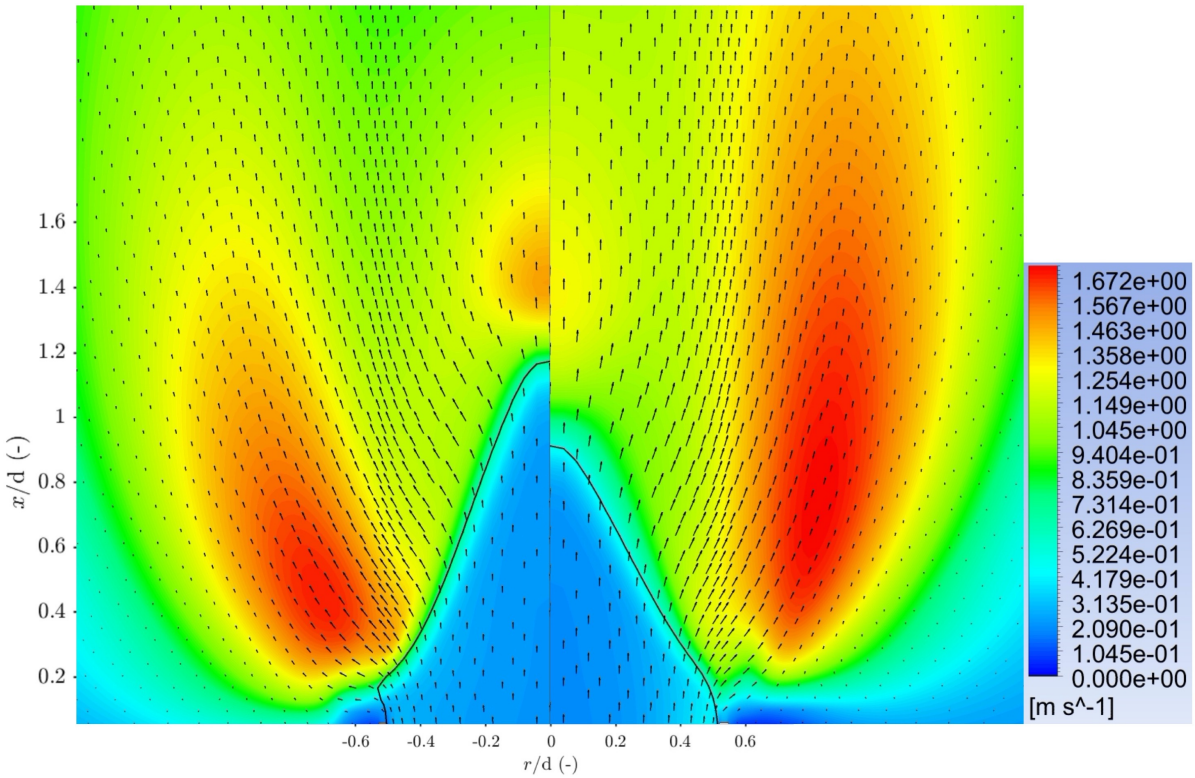

Figure 5.25: Comparison of root mean square turbulent velocity fluctuation contours, including flame front location corresponding to c = 0.2 and flow velocity vector field for flame 14. Turbulent flame speed relation: Left hand side; Zimont and right hand side; Dinkelacker et al.

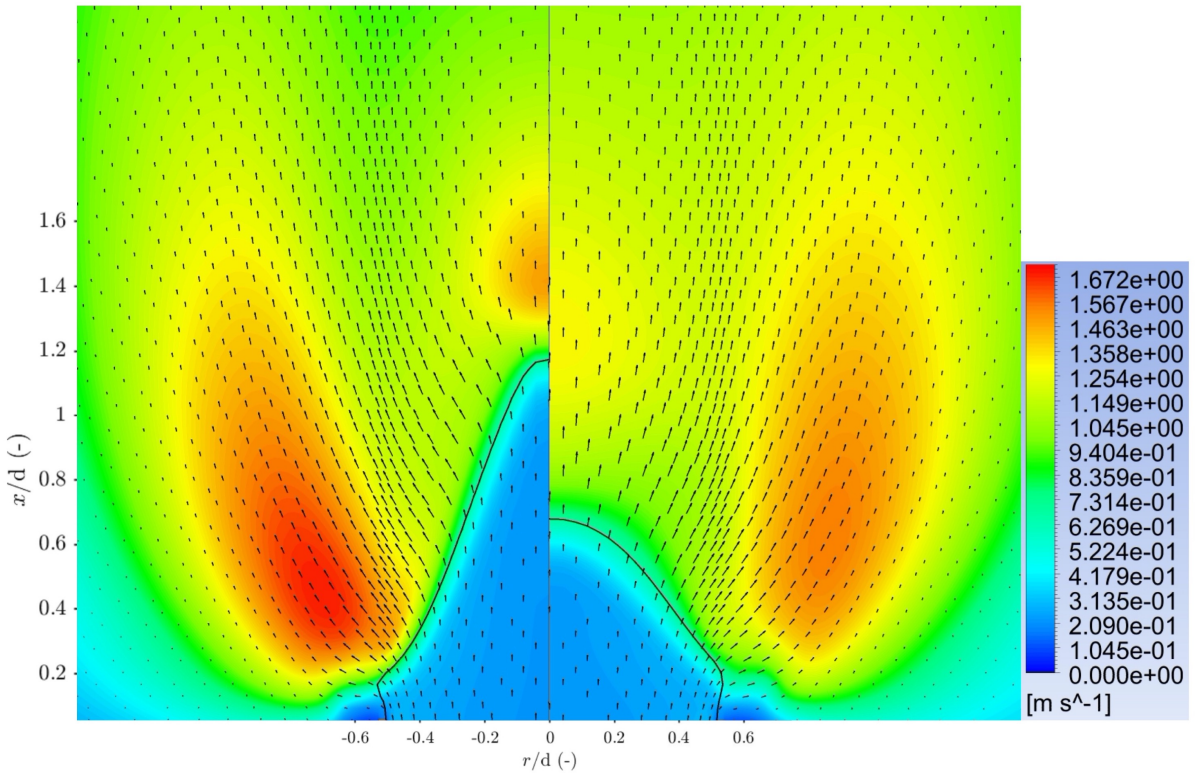

Figure 5.26: Comparison of root mean square turbulent velocity fluctuation contours, including flame front location corresponding to c = 0.2 and flow velocity vector field for flame 14. Turbulent flame speed relation: Left hand side; Zimont and right hand side; Cai et al.

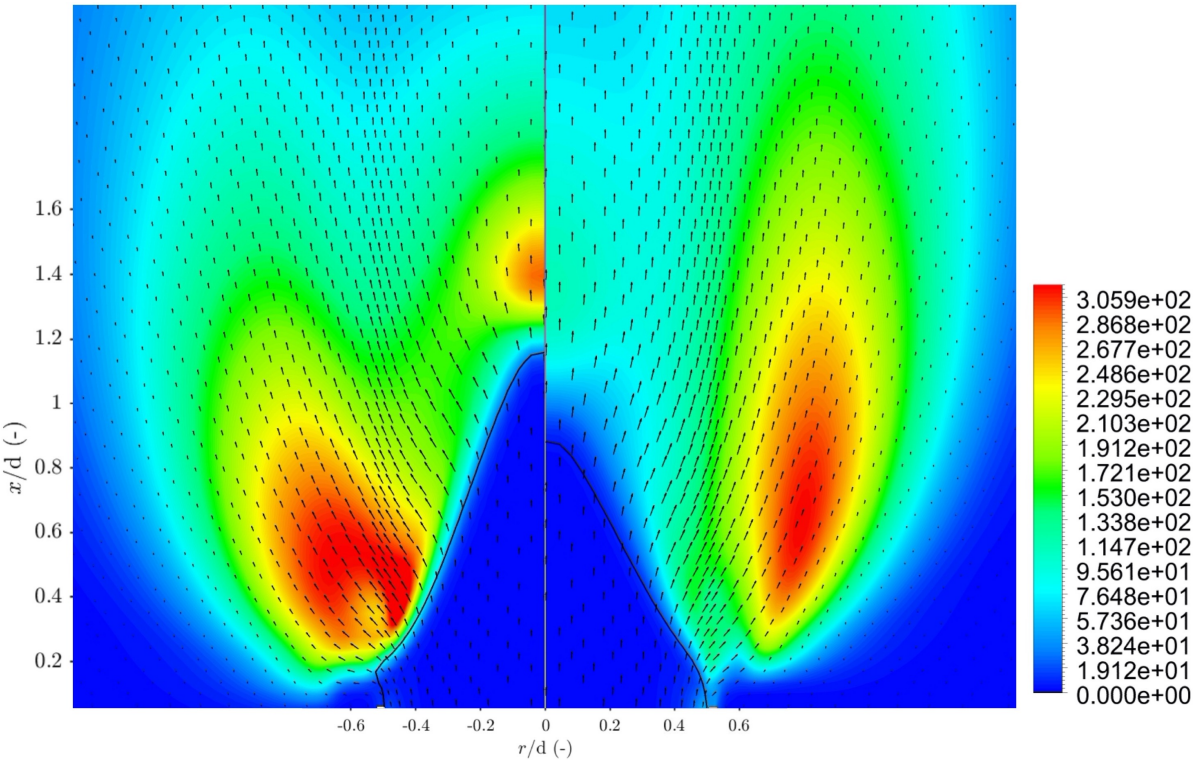

Figure 5.27: Comparison of turbulent dissipation rate contours, including flame front location corresponding to c = 0.2 and flow velocity vector field for flame 14. Turbulent flame speed relation: Left hand side; Zimont and right hand side; Dinkelacker et al.

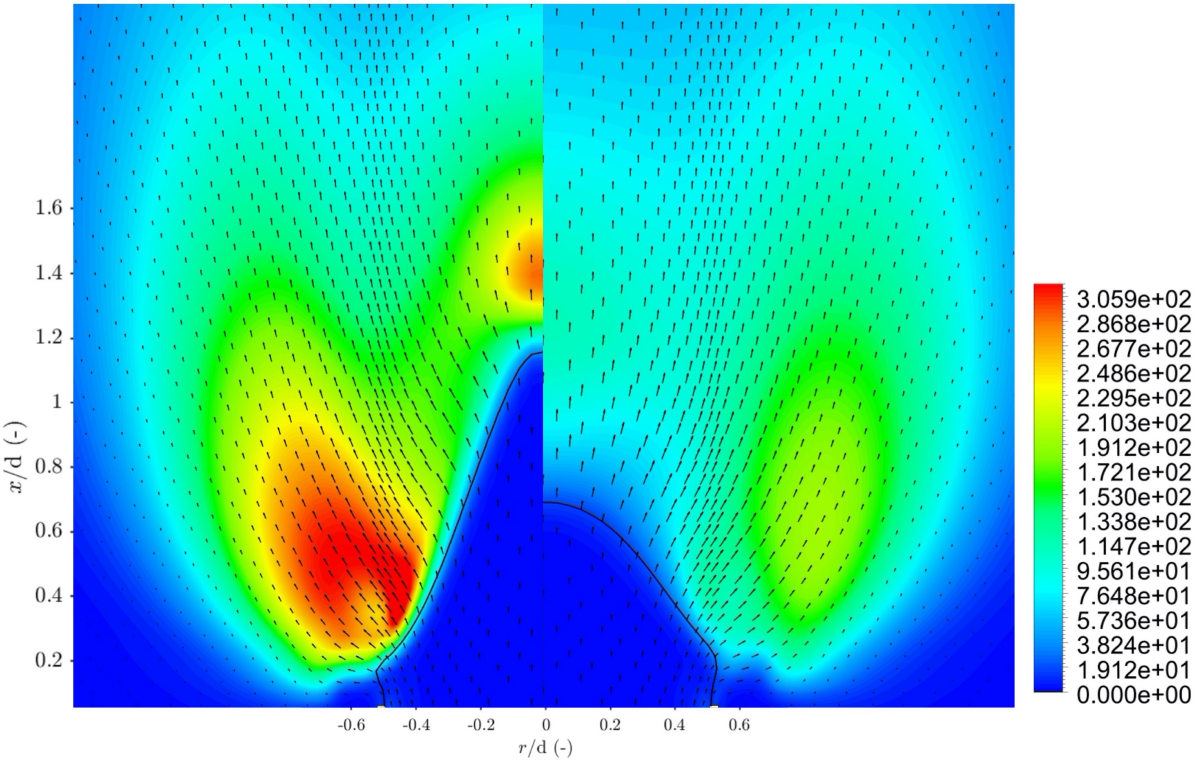

Figure 5.28: Comparison of turbulent dissipation rate contours, including flame front location corresponding to c = 0.2 and flow velocity vector field for flame 14. Turbulent flame speed relation: Left hand side; Zimont and right hand side; Cai et al.

Turbulent flame speed sensitivity

In figure 5.29 the relations between S_t, u' and l_t are plotted along the flame front locations, also seen in figures 5.20 and 5.21 corresponding to the progress variable of 0.2. The starting point of the figures where S_t/S_L^0 is equal to one is at the pipe wall, as there is no combustion and S_t is equal to S_L^0. And S_L^0 is a property of the incoming fuel mixture. From there the plotted curves follow the flame front to the pipe axis. Since $u' \sim \sqrt{(2/3)k}$ and $l_t \sim k^{3/2}/\epsilon$, these figures are in essence an analysis of the influence of the turbulent kinetic energy and the turbulent dissipation rate on the turbulent flame speed.

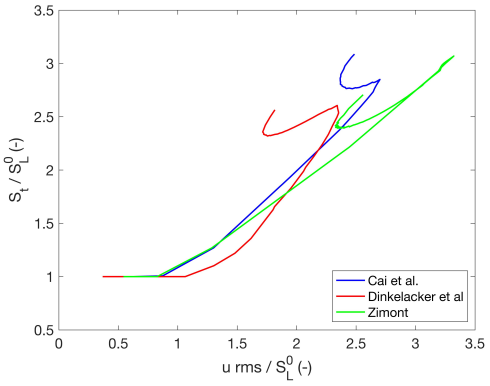

(a) Normalized turbulent flame speed plotted against normalized root mean square velocity.

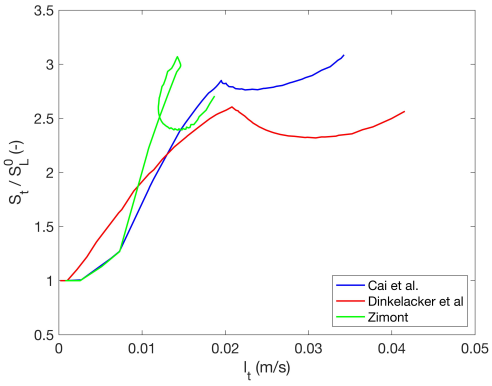

(b) Normalized turbulent flame speed plotted against integral length scale.

Figure 5.29: Normalized turbulent flame speed plots of flame 14 along the flame front location c = 0.2, from the pipe wall to the pipe axis. Data generated using Fluent.

The influence of u' and l_t is determined firstly by the values of u' and l_t which are flow dependent. But in this case one flame is studied with the same bulk velocity, only the turbulent flame speed correlations are changed. So upstream of the flame front u' and l_t have similar values, which is also seen in figures 5.25, 5.26, 5.27 and 5.28. And secondly by the power to which u' and l_t are raised in the specific correlation. Which is 0.75 in equation 5.7, 0.55 in equation 5.8 and 0.66 in equation 5.9 for u'. And respectively 0.25, 0.25 and 0.66 for l_t. The higher the value of the exponents, the greater the expected influence of u' and l_t on the turbulent flame speed. To validate this expectation figure 5.29 should be evaluated. As previously explained the plots start at the pipe wall. Following the flame front the turbulent flame speed rises until a maximum value is observed around the flame anchoring point (at this point the flame is more perpendicular with respect to the r/d plane), e.g. see x/d = 0.4 and r/d = 0.4 for the left hand side of figure 5.20. Further following the flame front a decrease in the turbulent flame speed is observed (more concave flame front). Finally another maximum is observed at the flame tip when the pipe axis is reached. It stands out that the maximum turbulent flame speed observed along the flame fronts is fairly similar for all three correlations, which was also seen in figures 5.23 and 5.24. However what drives the increase or decrease in turbulent flame speed differs. The Dinkelacker et al. and Cai et al. correlations are especially influenced more by the integral length scale than the Zimont correlation. Furthermore the correlation proposed by Cai et al. is driven less by changes in u' than the other correlations. Both of these conclusions are in line with the combination of all the contours.

Conclusion

Taking everything into account, the shorter cone and larger cone angle when modeling flame 14 with the correlations proposed by Dinkelacker et al. and Cai et al seems to be caused by a combination of factors. In both cases the shorter cone and larger cone angle is due to a larger distance between the iso-lines c = 0.1 and c = 0.9 of the progress variable compared to the flame modeled using the Zimont correlation. In case of the Dinkelacker et al. correlation the larger distance between the iso-lines is caused by turbulent diffusion effects. While for the case modeled using the Cai et al. correlation the larger distance seems to be an effect that compensates for the higher turbulent flame speed values by decreasing the gradient of the progress variable. The greater distance between the iso-lines results in lower values for the source term, but increases the size of the area where the flow field is influenced. Another important factor is the region with a high turbulent flame speed along the center line around

x/d = 1.4 for Dinkelacker et al. correlation and around x/d = 1.2 for the Cai et al. correlation. This high turbulent flame speed region is more pronounced and influences the source term in the cases modeled using the new correlations which seems to be a driving factor in shortening the cone length. The Dinkelacker et al. and especially the Cai et al. correlations are influenced more by the integral length scale than the Zimont correlation. Furthermore the correlation proposed by Cai et al. is driven less by changes in u' than the other correlations. This can also be formulated from another point of view, using the flame flow interaction. Meaning that the turbulent kinetic energy generated using Dinkelacker et al. and Cai et al. correlations dissipates at a lower rate compared to the case modeled using the Zimont correlation. And that the correlation by Cai et al. generates less turbulent velocity fluctuations. Other important factors in case of the Dinkelacker et al. correlation are the inclusion of the effective Lewis number. And the fact that the flame anchors very close to the pipe outlet, resulting in less leakage flow. Therefore more fuel is directly ignited resulting in a higher normalized velocity in the region just above the flame front. As a result the flame cone angle is larger and the cone is shorter.

5.3.2. Flame 15: Zimont vs Dinkelacker vs Cai

Normalized velocity field

Now the results of flame 15 will be considered. Flame 15 uses the 39.2 mm inner diameter burner, a bulk velocity of 6.50 m/s, an equivalence ratio of 0.8 and the fuel composition is 60 vol.% hydrogen. Comparing figures 5.30 and 5.31 it can be seen that the flames modeled using the correlations by Dinkelacker et al. and Cai et al. both have a shorter cone and a larger cone angle than the flame modeled using the Zimont correlation. This difference in cone angle leads to a higher acceleration of the flow across the flame front, as can be seen by considering the contour of the normalized velocity in the region just above the flame front. Looking at figure 5.30, the left side, modeled using the Zimont correlation shows a region above the flame front where the velocity magnitude is ranging from 1.4 to 1.7. While the right side, modeled using the Dinkelacker et al. correlation shows a region above the flame front which is much larger and ranges from approximately 1.7 to 2. The higher acceleration when modeling the flame with the correlation by Dinkelacker et al. expresses itself in an increase in velocity magnitude and an increase in size of the higher velocity region. The right side modeled using the Cai et al. correlation of figure 5.31 shows that the size of the region above the flame front has increased with respect to the left side modeled using the Zimont correlation. And that velocity magnitude ranges from approximately 1.4 to 1.8. So the higher acceleration when modeling the flame with the correlation by Cai et al. is mostly expressed by an increase in size of the higher velocity region. Once again the flame modeled using the correlation by Dinkelacker et al. is anchored the closest to the tube outlet, subsequently the flame modeled using the Zimont correlation and the flame modeled using the correlation by Cai et al. is anchored the furthest away from the tube outlet.

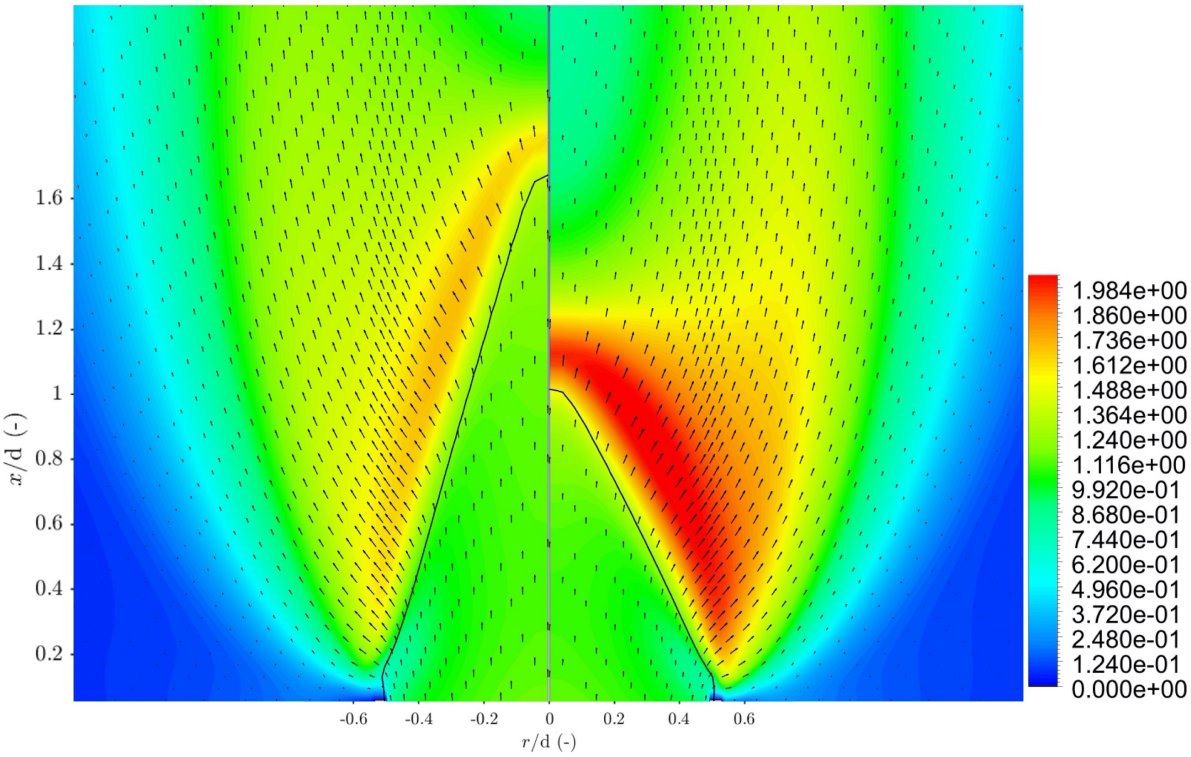

Figure 5.30: Comparison of velocity field u/U_b and flame front location corresponding to c = 0.2 for flame 15. Turbulent flame speed relation: Left hand side; Zimont and right hand side; Dinkelacker et al.

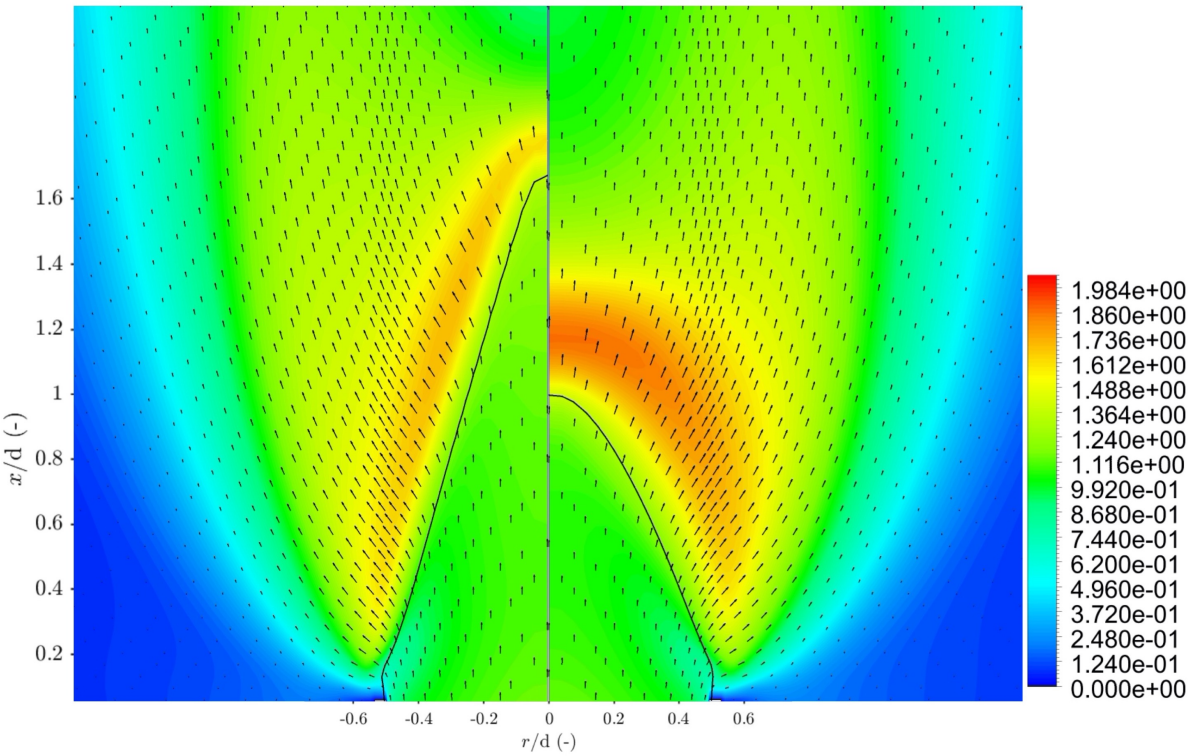

Figure 5.31: Comparison of velocity field u/U_b and flame front location corresponding to c = 0.2 for flame 15. Turbulent flame speed relation: Left hand side; Zimont and right hand side; Cai et al.

Turbulent flame speed and source term

As described earlier the turbulent flame speed should be considered while taking the gradient of the progress variable into consideration as well, to gain insight in what drives the source term. Therefore the contours of the turbulent flame speed are plotted together with two iso-lines of the progress variable with values of 0.1 and 0.9. The distance between the iso-lines gives an indication of the gradient of the progress variable. Looking at the turbulent flame speed contours seen in figures 5.33 and 5.34 it stands out that the iso-lines are separated by a larger distance in case of the new correlations, and especially in case of the Cai et al. correlation, meaning the gradient is smaller. Therefore a higher turbulent flame speed with respect to the case modeled using the Zimont correlation will be compensated in the source term by a smaller progress variable gradient. For all cases the maximum in turbulent flame speed is observed near the location r/d = 0.6 and x/d = 0.2. However this is largely outside of the region between the iso-lines of the progress variable and therefore does not contribute to the production rate of the progress variable. Furthermore it can be seen that the observed values of the turbulent flame speed are fairly similar for all cases. Although the highest turbulent flame speed is observed for the case modeled using the Dinkelacker et al. correlation, seen on the right side of figure 5.33. Both cases modeled using the correlation by Dinkelacker et al. and Cai et al. show a larger area of high turbulent flame speed (red region, outside the region between the iso-lines) compared to the case modeled using the Zimont correlation. Additionally, the turbulent flame speed observed between the iso-lines of the progress variable has values of approximately 1.0 to 2.3 m/s in the case modeled using the Dinkelacker et al. correlation and values of approximately 1.0 to 2.2 for the case modeled using the correlation by Cai et al., while this is only 1.0 to 1.8 m/s in case of the Zimont correlation. Another thing that stands out is the region of higher values of the turbulent flame speed downstream of the flame front along the center line, r/d = 0. This region is observed around x/d = 1.3 for the Dinkelacker et al. correlation and around x/d = 1.4 for the Cai et al. correlation. Both of these high turbulent flame speed regions influence the source term, since they affect the region between the iso-lines of the progress variable. This area of higher values of the turbulent flame speed is almost non existent for the case modeled using the Zimont correlation.

To evaluate the combined effect of the greater distance between the iso-lines and the higher observed turbulent flame speed for the cases modeled using the new correlations, the source term is plotted along the pipe axis in figure 5.32. Along the axis the source terms modeled using the Dinkelacker et al. correlation has a higher maximum than the maxima observed in the cases modeled using the Zimont and Cai et al. correlations. For the case modeled using the Cai et al. correlation, the length of the distance x/d where the source term is not equal to zero is larger than for the other two correlations. Therefore the source term modeled with the Cai et al. correlation is present in a broader area, which is in line with the greater distance between the iso-lines.

For this flame the correlation by Dinkelacker et al. results in the highest turbulent flame speed values. The maximum of the source term of the progress variable along the pipe axis is the highest using the Dinkelacker et al. correlation and the lowest using the Cai et al. correlation, as seen in figure 5.32. Another difference is that the iso-lines corresponding to c = 0.1 and c = 0.9 are separated by a larger distance in case of the new correlations, which is especially true for the flame modeled using the Cai et al. correlation. Resulting in a smaller gradient, but a larger area where the source term influences the flow. In conclusion, in the case modeled using the correlation by Dinkelacker et al. the shorter cone length is driven by the higher turbulent flame speed in the area between the iso-lines, leading to an increase of the source term with respect to the Zimont correlation. And in the case modeled using the correlation by Cai et al. the shorter cone length appears to be caused by the increased distance between the iso-lines. Which also explains the increase in velocity magnitude observed in figures 5.30 and 5.31 for the cases modeled with the new correlations.

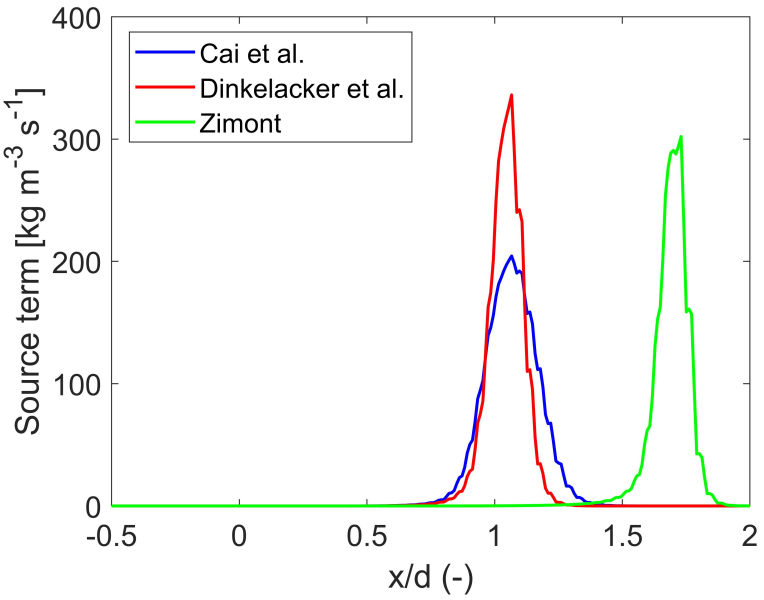

Figure 5.32: Comparison of the source term along the pipe axis for flame 15. Data generated using Fluent.

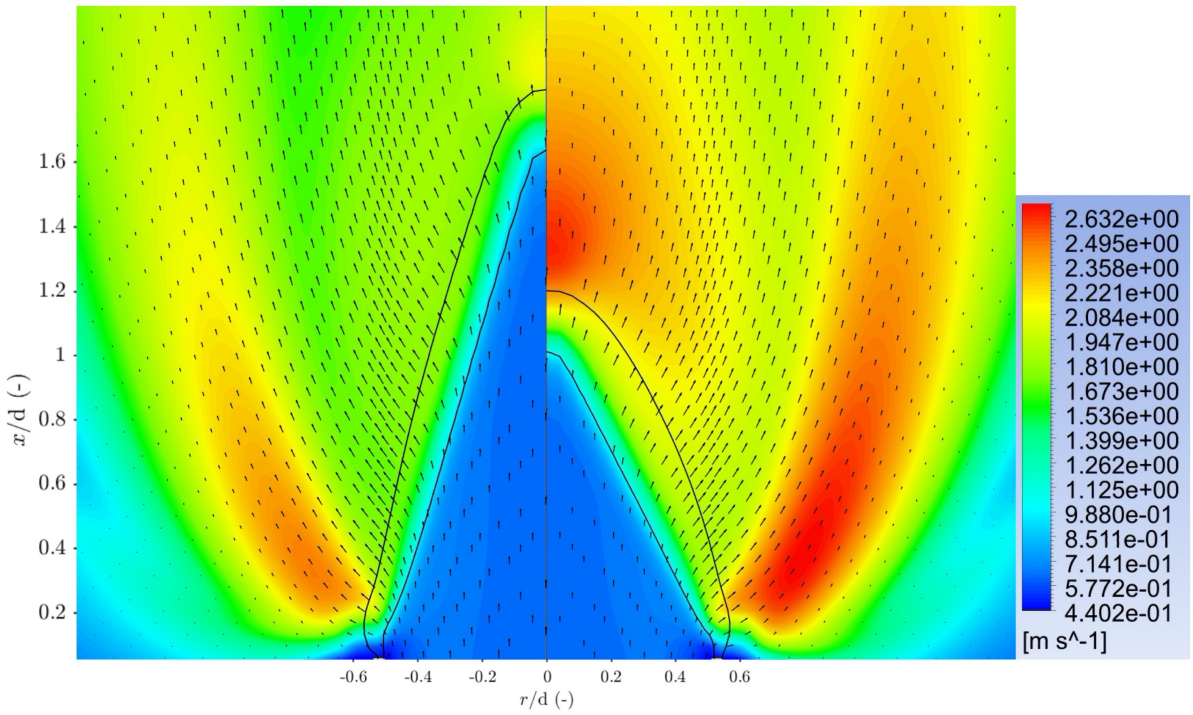

Figure 5.33: Comparison of turbulent flame speed contours, including progress variable isocontours corresponding to c = 0.1 and 0.9 and flow velocity vector field for flame 15. Turbulent flame speed relation: Left hand side; Zimont and right hand side; Dinkelacker et al.

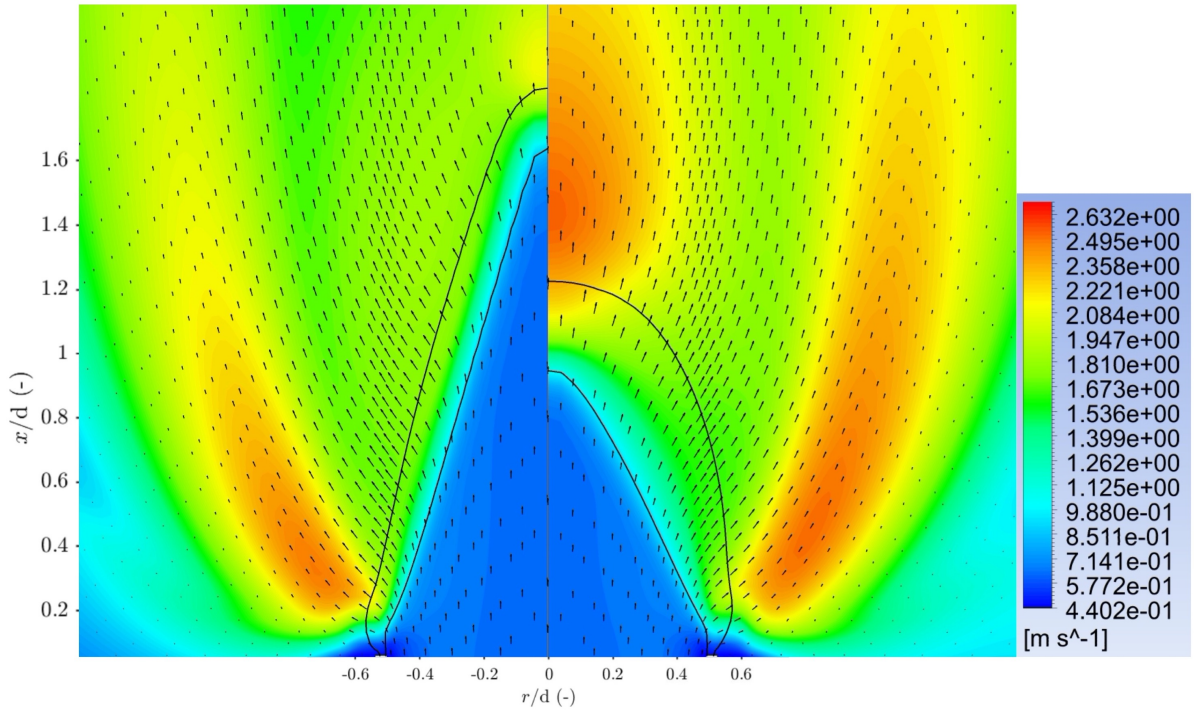

Figure 5.34: Comparison of turbulent flame speed contours, including progress variable isocontours corresponding to c = 0.1 and 0.9 and flow velocity vector field for flame 15. Turbulent flame speed relation: Left hand side; Zimont and right hand side; Cai et al.

Root mean square turbulent velocity fluctuations and turbulent dissipation rate

The turbulent flame speed only influences the source term if the gradient of the progress variable is non zero. But it is helpful to analyse the turbulent flame speed in areas where the gradient is zero, since it provides insight in the driving factors causing the difference in results using the new turbulent flame speed correlations. As earlier described the turbulent flame speed is influenced by the root mean square of the turbulent velocity fluctuations u' and the integral length scale l_t. The contours of the u' values are plotted in figures 5.35 and 5.36. On the right side of figure 5.35 it can be seen that the correlation by Dinkelacker et al. results in a much larger area (above r/d = 0.6) of high u' values compared to the flame modeled using the Zimont correlation on the left side. And the maximum values observed in the case modeled using the Dinkelacker et al. correlation are significantly higher than the case modeled using the Zimont correlation. Another thing that stands out is the region of high u' values near the location x/d = 1.3 along the center line in the case modeled using the Dinkelacker et al. correlation. This region with high values along the center line is present in the two other cases, but at a significantly lower extent. On the right side of figure 5.36 it can be seen that when modeled with the Cai et al. correlation, the u' values in the area above r/d = 0.6 are similar to the values observed on the left side of the figure. However an increase in size of region with high u' values is observed. The contours of the turbulent dissipation rate ϵ are plotted in figures 5.37 and 5.38. For clarification $l_t \sim k^{3/2}/\epsilon$. Meaning lower values of ϵ result in higher values of l_t. The comparison of the flame modeled using Zimont and Dinkelacker et al. correlations in figure 5.37 shows a higher turbulent dissipation rate for the flame modeled using the correlation by Dinkelacker et al. Furthermore this flame shows a peak in dissipation rate along the center line at x/d = 1.3. This maximum decreases the integral length scale and slightly compensates for the high values of u' seen near the same location. Furthermore it can be seen on the right side of figure 5.38 that the flame modeled using the correlation by Cai et al. shows lower values for ϵ above the area r/d = 0.6 than both the case modeled using the Zimont and Dinkelacker et al. correlations. Which implies larger turbulent length scales. Since the flame modeled using the Dinkelacker et al. correlation shows the highest turbulent dissipation rate, the turbulent length scales are the smallest. Therefore it can be concluded that the increased turbulent flame speed and size of the higher turbulent flame speed area is due to the increase in u' values and the increase in size of the high u' values region. For the case modeled using the Cai et al. correlation, the larger turbulent length scales in combination with the increased size of the region with high u' values explains the increased turbulent flame speed and size of the higher turbulent flame speed area.

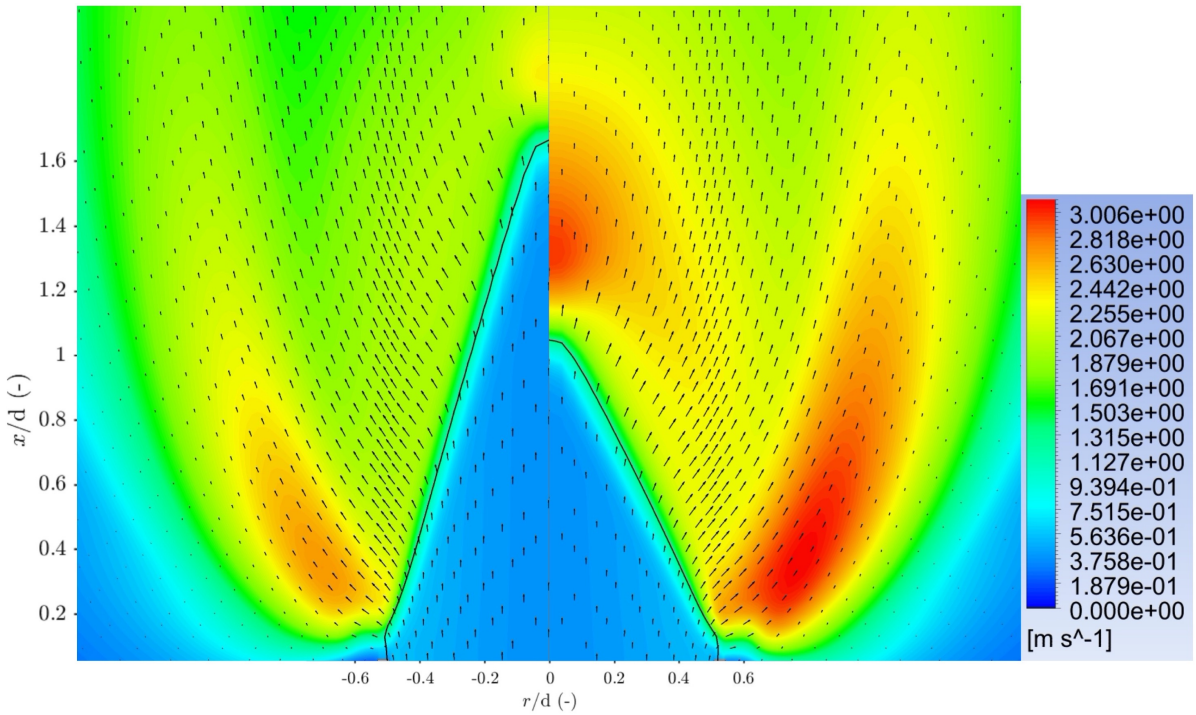

Figure 5.35: Comparison of root mean square turbulent velocity fluctuation contours, including flame front location corresponding to c = 0.2 and flow velocity vector field for flame 15. Turbulent flame speed relation: Left hand side; Zimont and right hand side; Dinkelacker et al.

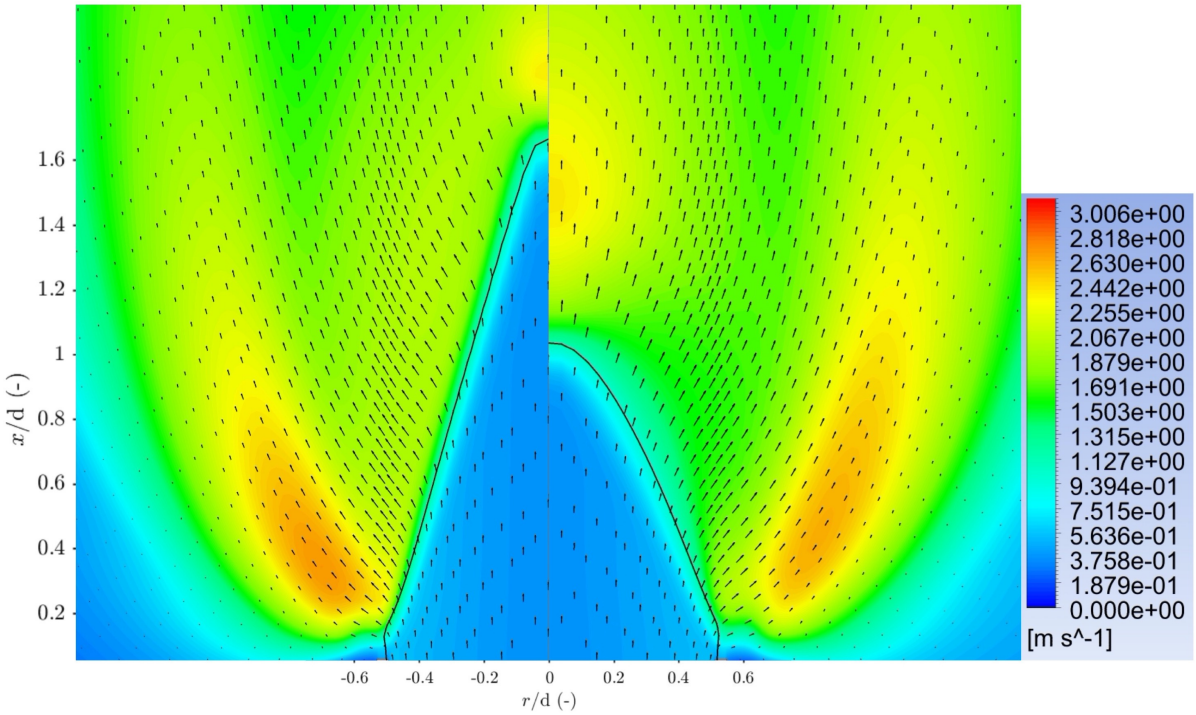

Figure 5.36: Comparison of root mean square turbulent velocity fluctuation contours, including flame front location corresponding to c = 0.2 and flow velocity vector field for flame 15. Turbulent flame speed relation: Left hand side; Zimont and right hand side; Cai et al.

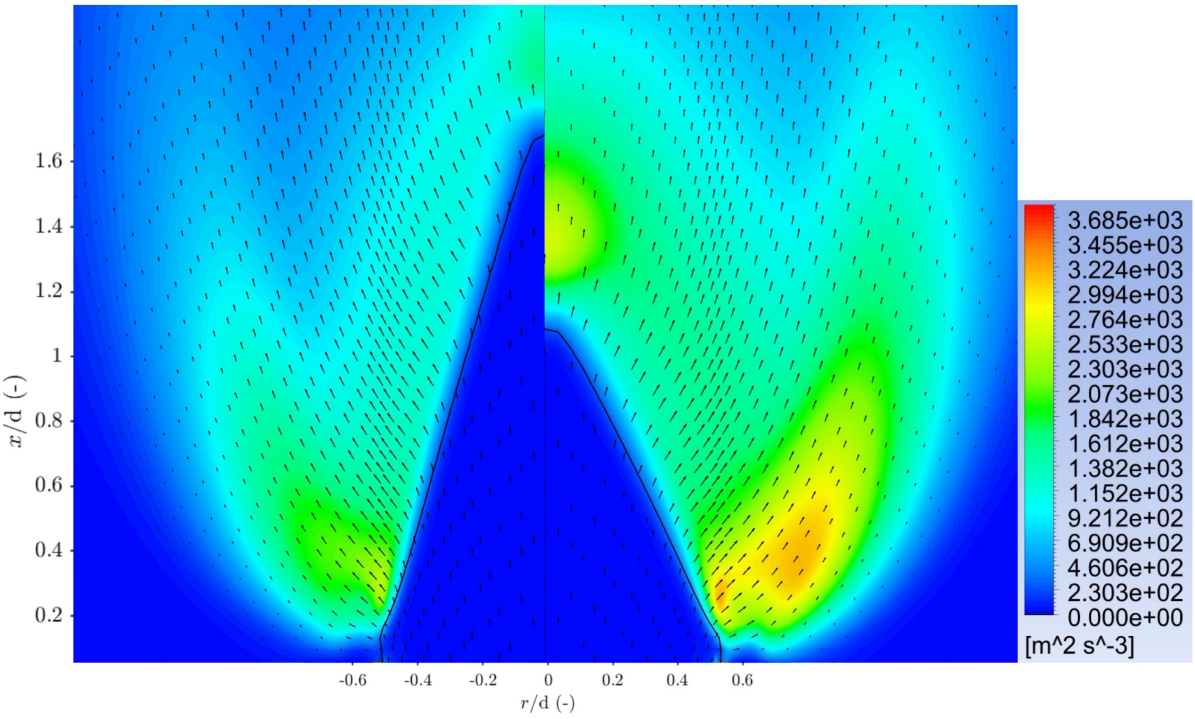

Figure 5.37: Comparison of turbulent dissipation rate contours, including flame front location corresponding to c = 0.2 and flow velocity vector field for flame 15. Turbulent flame speed relation: Left hand side; Zimont and right hand side; Dinkelacker et al.

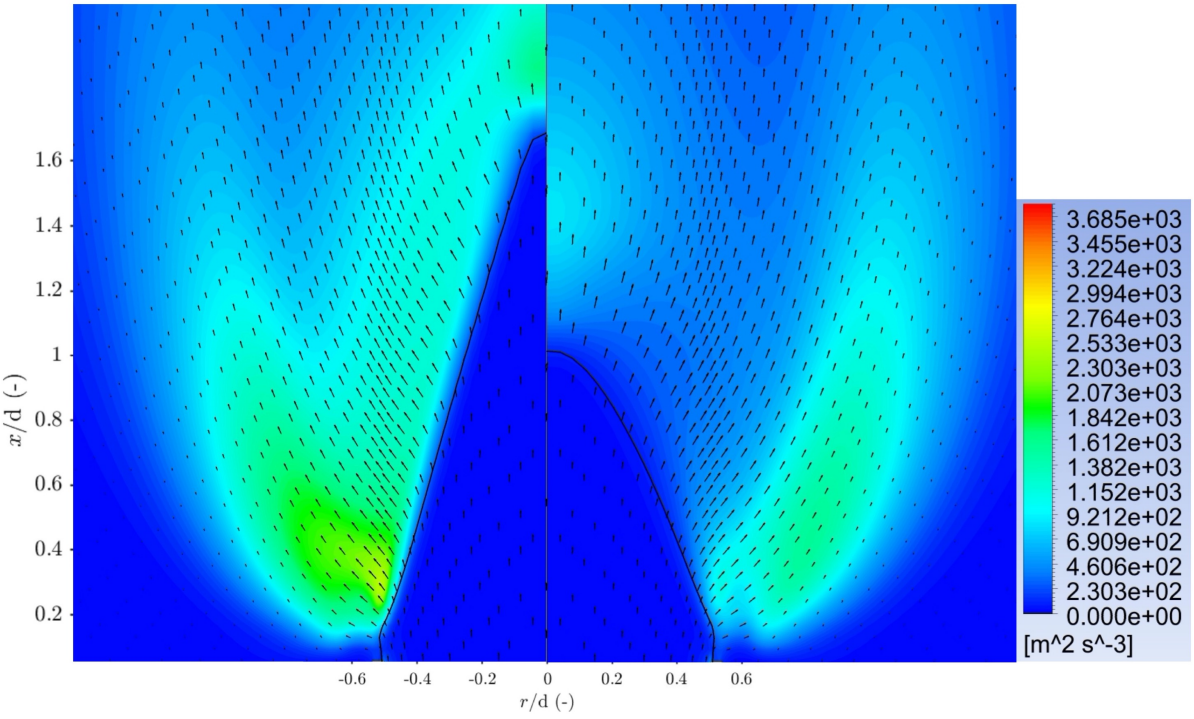

Figure 5.38: Comparison of turbulent dissipation rate contours, including flame front location corresponding to c = 0.2 and flow velocity vector field for flame 15. Turbulent flame speed relation: Left hand side; Zimont and right hand side; Cai et al.

Turbulent flame speed sensitivity

In figure 5.39 the relations between S_t, u' and l_t are plotted along the flame front locations, also seen in figures 5.30 and 5.31 corresponding to the progress variable of 0.2. The starting point of the figures where S_t/S_L^0 is equal to one is at the pipe wall, as there is no combustion and S_t is equal to S_L^0. From there the plotted curves follow the flame front to the pipe axis. Since $u' \sim \sqrt{(2/3)k}$ and $l_t \sim k^{3/2}/\epsilon$, these figures are in essence an analysis of the influence of the turbulent kinetic energy and the turbulent dissipation on the turbulent flame speed.

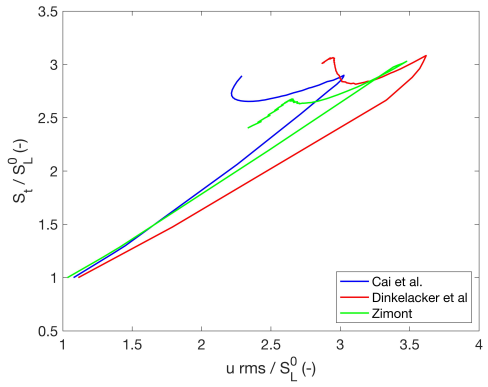

(a) Normalized turbulent flame speed plotted against normalized root mean square velocity.

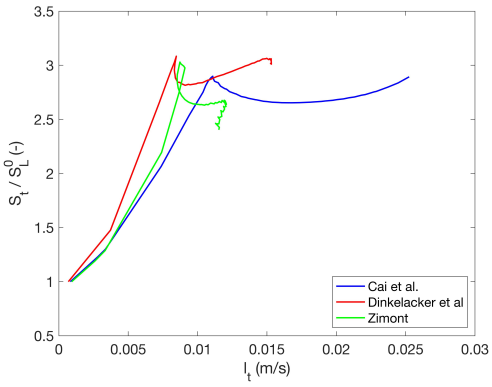

(b) Normalized turbulent flame speed plotted against integral length scale.

Figure 5.39: Normalized turbulent flame speed plots of flame 15 along the flame front location c = 0.2, from the pipe wall to the pipe axis. Data generated using Fluent.

Earlier the influence of u' and l_t was explained. In short the higher the value of the exponents, the greater the expected influence of u' and l_t on the turbulent flame speed. To validate this expectation figure 5.39 should be evaluated while taking the presented contours in consideration. As previously explained the plots start at the pipe wall. Following the flame front, the turbulent flame speed rises until a maximum value is observed around the flame anchoring point (at this point the flame is more perpendicular with respect to the r/d plane). E.g. x/d = 0.2 and r/d = 0.5 for the left hand side of figure 5.30. Further following the flame front a decrease in the turbulent flame speed is observed (more concave flame front). Finally another maximum is observed at the flame tip when the pipe axis is reached. Although in the case modeled using the Zimont correlation a drop in turbulent flame speed is observed at the flame tip. Again it stands out that the maximum turbulent flame speed observed along the flame fronts is fairly similar for all three correlations, but the flame modeled using the Zimont correlation shows the lowest turbulent flame speed. Which was also seen in figures 5.33 and 5.34. However what drives the increase or decrease in turbulent flame speed differs. The Cai et al. correlation is influenced more by the integral length scale than the other two correlations and the influence of u' is slightly higher compared to the Zimont correlation. The increased turbulent flame speed observed when modeling with the correlation proposed by Dinkelacker et al. is driven mostly by higher u' values.

Conclusion

When modeling flame 15 with the Dinkelacker et al. correlation the shorter cone and larger cone angle is caused by the increased source term with respect to the Zimont correlation. The increase in source term is caused by higher turbulent flame speed values. Also the iso-lines of the progress variable values of 0.1 and 0.9 are separated by a greater distance, which decreases the gradient and therefore the source term. But increases the size of the area where the flow field is influenced by the source term. Another important factor is the region with a high turbulent flame speed along the center line around x/d = 1.3. The main cause of the higher turbulent flame speed observed when modeling with the Dinkelacker et al. correlation is the higher influence of u' due to higher turbulent velocity fluctuations. In the case modeled using the Cai et al. correlation, the shorter cone and larger cone angle appears to be caused by a larger distance between the iso-lines c = 0.1 and c = 0.9 of the progress variable in combination with a higher turbulent flame speed, compared to the flame modeled using the Zimont correlation. The

main cause for the higher turbulent flame speed observed when modeling with the correlation by Cai et al is that the correlation is influenced more by the integral length scale than the Zimont and Dinkelacker et al correlations. The greater distance between the iso-lines results in a smaller gradient and therefore lowers the source term, but increases the size of the area where the flow field is influenced. Another important factor is the region with a high turbulent flame speed along the center line around x/d = 1.4. This high turbulent flame speed region is more pronounced in the cases modeled using the new correlations and seems to be a driving factor in shortening the cone length. This conclusion can also be formulated from another point of view, using the flame flow interaction. Meaning that the turbulent kinetic energy generated using the Cai et al. correlation dissipates at a lower rate compared to the case modeled using the Zimont and Dinkelacker et al. correlations. And that the Zimont correlation generates the least amount turbulent velocity fluctuations, thereafter the Cai et al. correlation. And the Dinkelacker et al generates the highest amount of turbulent velocity fluctuations. Other important factors in case of the Dinkelacker et al. correlation are the inclusion of the effective Lewis number. And the fact that the flame anchors very close to the pipe outlet, resulting in less leakage flow. Therefore more fuel is directly ignited resulting in a higher normalized velocity in the region just above the flame front. As a result the flame cone angle is larger and the cone is shorter.

5.3.3. Flame 9: Zimont vs Dinkelacker vs Cai

Normalized velocity field

Lastly the results of flame 9 with the highest hydrogen concentration, seen in figures 5.40 and 5.41 are evaluated. Flame 9 uses the 39.2 mm inner diameter burner, a bulk velocity of 6.00 m/s, an equivalence ratio of 0.6 and the fuel composition is 80 vol.% hydrogen. Once again it can be seen that the flames modeled using the correlations by Dinkelacker et al. and Cai et al. both have a shorter cone and a larger cone angle than the flame modeled using the Zimont correlation. Which leads to a higher acceleration of the flow across the flame front. However in contrary to the results of flames 14 and 15, in this case the largest increase in velocity magnitude is observed when modeling the flame using the correlation proposed by Cai et al. Looking at the right side of figure 5.41 the velocity magnitude determined using the Cai et al. correlation is ranging from 1.7 to 2, while the velocity magnitude determined using the Dinkelacker et al. correlation on the right side of figure 5.40 only ranges from 1.5 to 1.7. The velocity magnitude seen on the left side of both figures, when modeling the flame using the Zimont correlation is approximately equal to 1.5 in the entire region just downstream of the flame front. Furthermore the locations at which the flame anchors are relatively similar in this case.

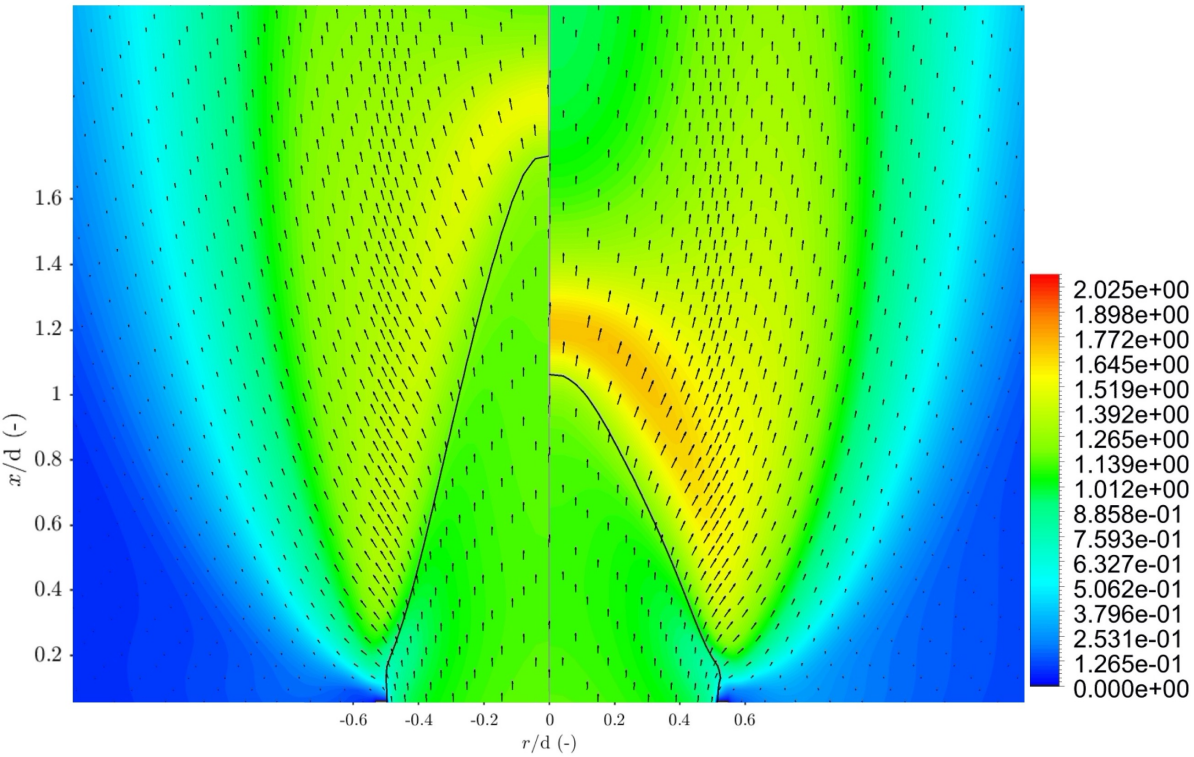

Figure 5.40: Comparison of velocity field u/U_b and flame front location corresponding to c = 0.2 for flame 9. Turbulent flame speed relation: Left hand side; Zimont and right hand side; Dinkelacker et al.

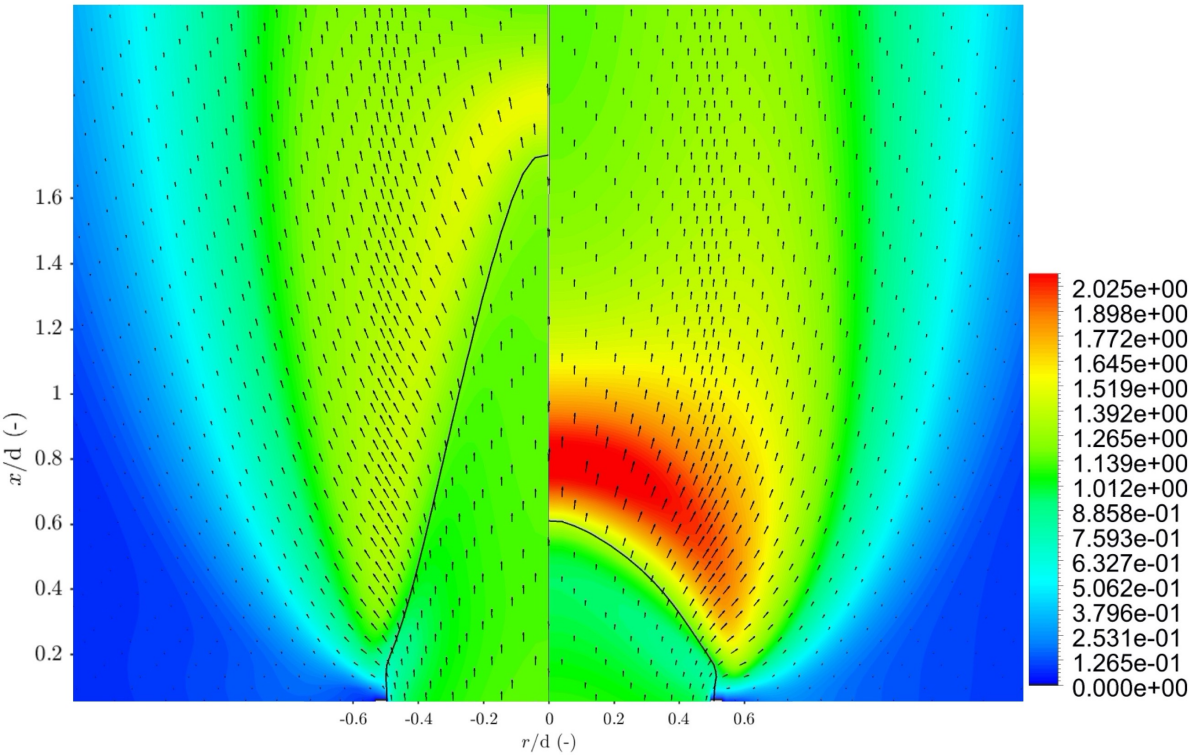

Figure 5.41: Comparison of velocity field u/U_b and flame front location corresponding to c = 0.2 for flame 9. Turbulent flame speed relation: Left hand side; Zimont and right hand side; Cai et al.

Turbulent flame speed and source term

The turbulent flame speed will again be considered while taking the gradient of the progress variable into account using the two iso-lines of the progress variable. Looking at the turbulent flame speed contours seen in figures 5.43 and 5.44 it can be seen that the iso-lines are separated by a larger distance in case of the Cai et al. correlation, while they are separated by a similar distance in the cases modeled using the Dinkelacker et al. and Zimont correlations. Therefore a higher turbulent flame speed will be compensated by a smaller gradient only in the case modeled using the Cai et al. correlation. It stands out that for all cases a maximum in turbulent flame speed is observed near the location r/d = 0.6 and x/d = 0.2. However this is largely outside of the region between the iso-lines of the progress variable and therefore does not contribute to the production rate of the progress variable. Furthermore it can be seen that the observed values of the turbulent flame speed are the highest for the cases modeled using the Dinkelacker et al. and Cai et al. correlations, seen on the right sides of figures 5.43 and 5.44. Both cases modeled using the correlation by Dinkelacker et al. and Cai et al. show a larger area of high turbulent flame speed (red region, outside the area between the iso-lines) compared to the case modeled using the Zimont correlation. Additionally, the turbulent flame speed observed between the iso-lines has values of approximately 0.8 to 2.0 m/s in case of the Dinkelacker et al. correlation, 0.8 to 2.2 in case of the Cai et al. correlation, while this is 0.7 to 1.7 m/s in case of the Zimont correlation. Again the region of higher values of the turbulent flame speed downstream of the flame front along the center line, r/d = 0 stands out. This region is observed around x/d = 1.4 for the Dinkelacker et al. correlation and around x/d = 1.1 for the Cai et al. correlation. This area of higher values of the turbulent flame speed is almost non existent for the case modeled using the Zimont correlation. The high turbulent flame speed region along the center line downstream of the flame front in the cases modeled using the new correlations is located within the region between the iso-lines and therefore influences the source terms. Once again they appear to be a driving factor for the shorter flame cone.

To evaluate the combined effect of the greater distance between the iso-lines and the higher observed turbulent flame speed for the cases modeled using the new correlations, the source term is plotted along the pipe axis in figure 5.42. Along the axis the source term modeled using the Dinkelacker et al. correlation has values higher than the values observed in the cases modeled using the Zimont and Cai et al. correlations. For this flame the maximum of the source terms modeled with the Zimont and Cai et al. correlations are similar. Although for the case modeled using the Cai et al. correlation the maximum is observed much closer to the exit of the pipe. Furthermore the source term modeled with the Cai et al. correlation is present over a longer distance x/d, which is in line with the greater distance between the iso-lines.

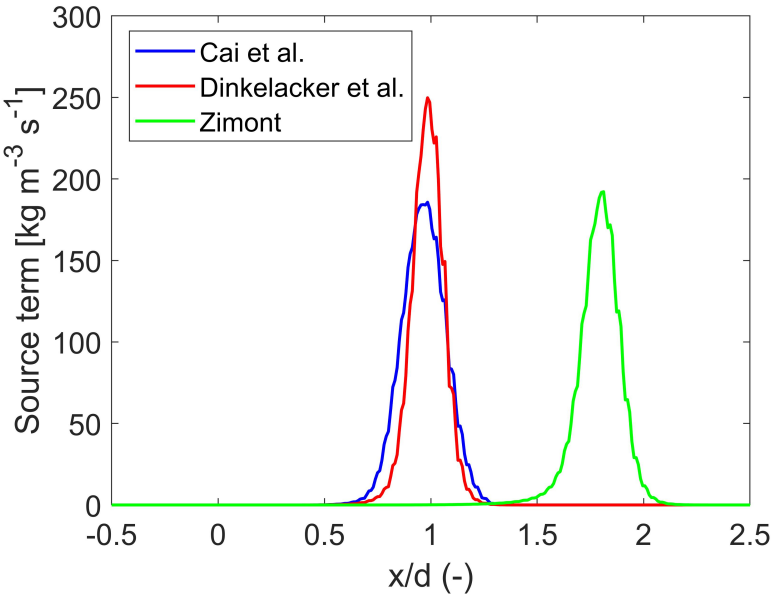

Figure 5.42: Comparison of the source term along the pipe axis for flame 9. Data generated using Fluent.

For this flame the two new correlations result in a higher turbulent flame speed values, but only the maximum of the source term modeled with the Dinkelacker et al. correlation is higher than the maximum of the source term modeled with the Zimont correlation, as seen in figure 5.42. For the Cai et al. correlation the difference with respect to the Zimont correlation is that the iso-lines corresponding to c = 0.1 and c = 0.9 are separated by a larger distance and the observed turbulent flame speed values are higher. This combination results in a source term similar to the Zimont correlation. But due to a larger area where the flow is affected, the flame cone is shorter. The increase in velocity magnitude observed in figure 5.40 modeled with the Dinkelacker et al. correlation instead of the Zimont correlation can be attributed to the higher turbulent flame speed leading to a higher source term. While the increase in velocity magnitude when modeled with the Cai et al. correlation observed in figure 5.41 can be attributed to the combination of the higher flame speed values and the larger distance between the iso-lines.

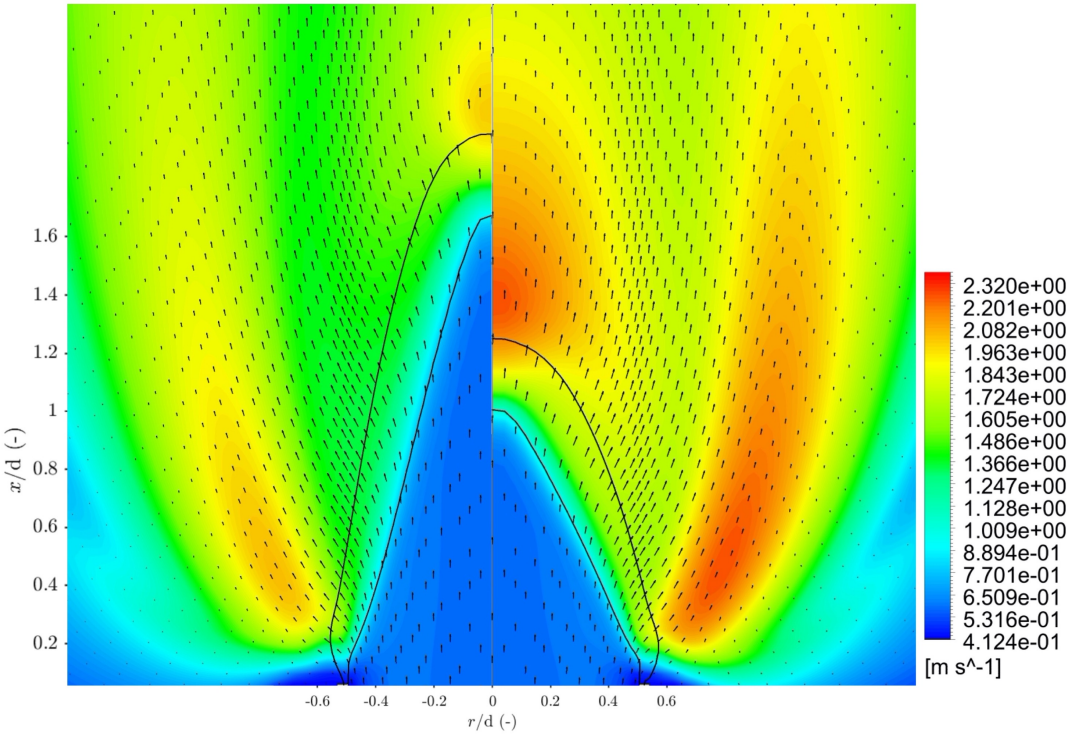

Figure 5.43: Comparison of turbulent flame speed contours, including progress variable isocontours corresponding to c = 0.1 and 0.9 and flow velocity vector field for flame 9. Turbulent flame speed relation: Left hand side; Zimont and right hand side; Dinkelacker et al.

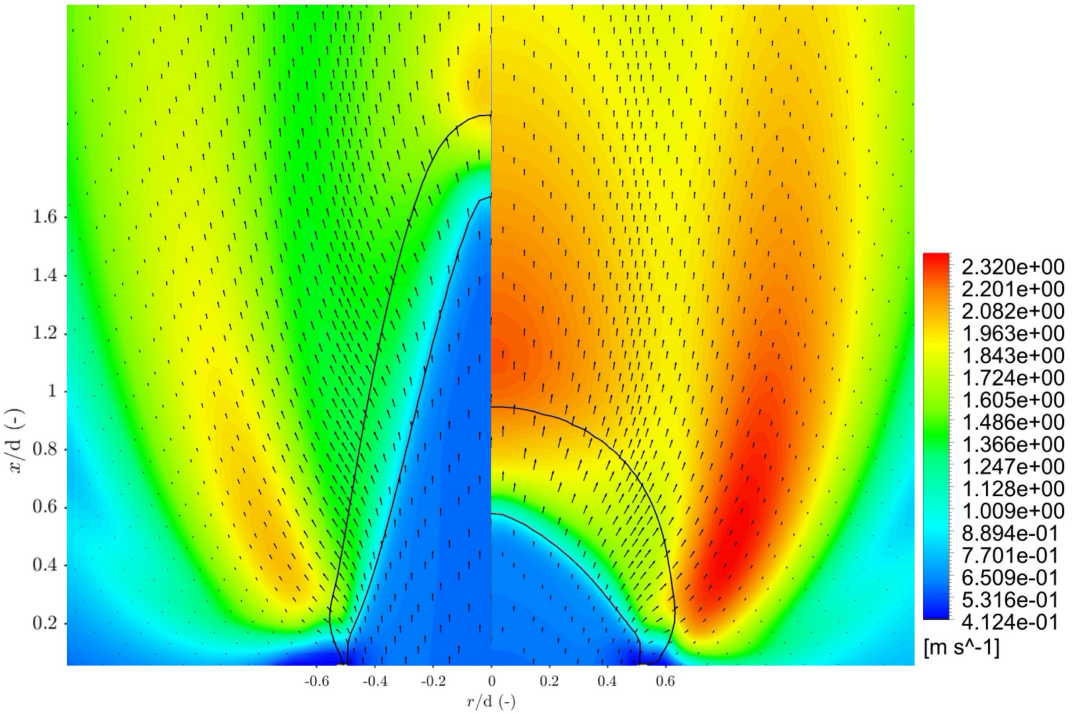

Figure 5.44: Comparison of turbulent flame speed contours, including progress variable isocontours corresponding to c = 0.1 and 0.9 and flow velocity vector field for flame 9. Turbulent flame speed relation: Left hand side; Zimont and right hand side; Cai et al.

Root mean square turbulent velocity fluctuations and turbulent dissipation rate

As earlier described the turbulent flame speed is influenced by the root mean square of the turbulent velocity fluctuations u' and the integral length scale l_t. Similar to the previous flame the influence of these parameters will be evaluated outside of the region where they influence the source term to gain insight in the factors driving the turbulent flame speed. The contours of the u' values are plotted in figures 5.45 and 5.46. On the right side of figure 5.45 it can be seen that the correlation by Dinkelacker et al. results in a much larger area (above r/d = 0.6) of high u' values compared to the flame modeled using the Zimont correlation on the left side. And the maximum values observed in the case modeled using the Dinkelacker et al. correlation are significantly higher than the case modeled using the Zimont correlation. The same is seen on the right side of figure 5.46 modeled using the correlation by Cai et al. Another thing that stands out is the region of high u' values near the locations x/d = 1.4 and x/d = 1.1 along the center line in the cases modeled using the correlations by Dinkelacker et al. and Cai et al. respectively. This region with high values along the center line is present in the case modeled using the Zimont correlation, but at a significantly lower extent. The contours of the turbulent dissipation rate ϵ are plotted in figures 5.47 and 5.48. Again for clarification $l_t \sim k^{3/2}/\epsilon$, meaning lower values of ϵ result in higher values of l_t. The comparison of the flame modeled using Zimont and Dinkelacker et al. correlations in figure 5.47 shows a higher turbulent dissipation rate for the flame modeled using the correlation by Dinkelacker et al. Furthermore this flame shows a peak in dissipation rate along the center line at x/d = 1.4. This maximum decreases the integral length scale and slightly compensates for the high values of u' seen near the same location. Furthermore it can be seen on the right side of figure 5.48 that the flame modeled using the correlation by Cai et al. shows higher values for ϵ above the area r/d = 0.6 than the case modeled using the Zimont correlation. Which implies smaller turbulent length scales. Since the flame modeled using the Dinkelacker et al. correlation shows the highest turbulent dissipation rate, the turbulent length scales are the smallest. Therefore it can be concluded that the increased turbulent flame speed and size of the higher turbulent flame speed area is due to the increase in u' values and the increase in size of the high u' values region. For the case modeled using the Cai et al. correlation, a similar statement can be made since the turbulent dissipation rate is significantly higher than observed in the case modeled using the Zimont correlation and fairly similar to the case modeled using the Dinkelacker et al correlation.

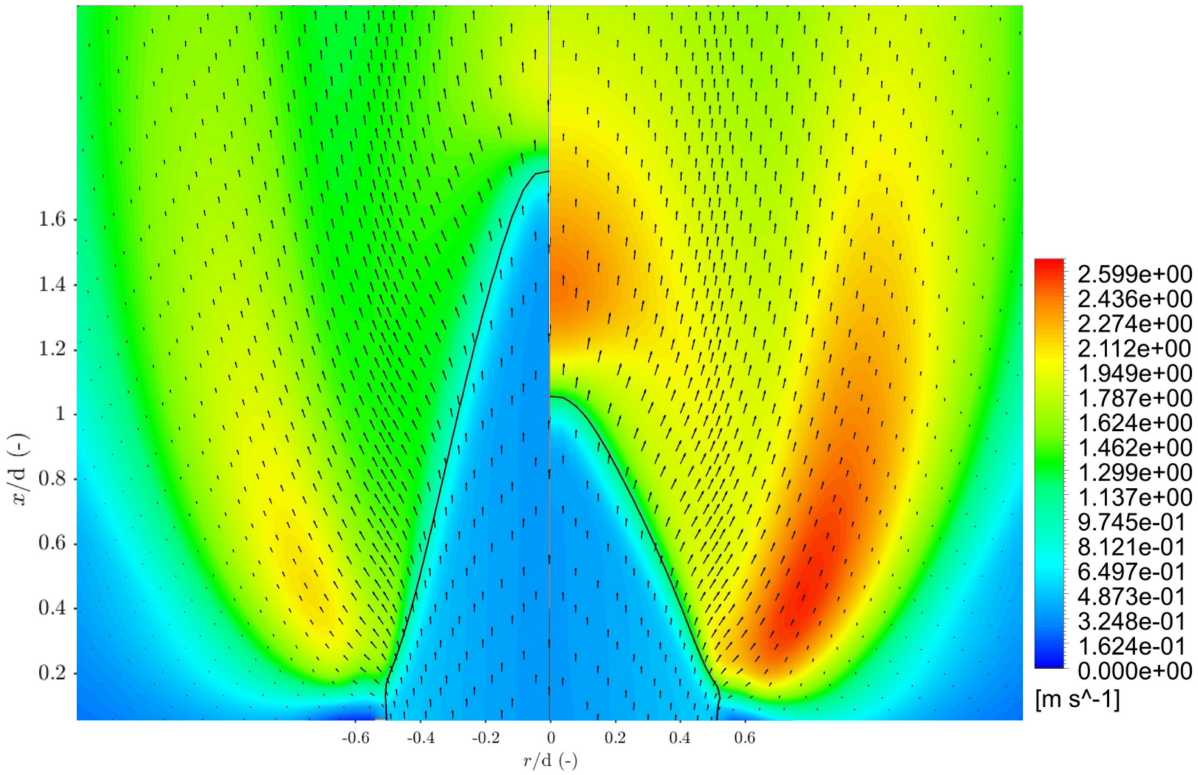

Figure 5.45: Comparison of root mean square turbulent velocity fluctuation contours, including flame front location corresponding to c = 0.2 and flow velocity vector field for flame 9. Turbulent flame speed relation: Left hand side; Zimont and right hand side; Dinkelacker et al.

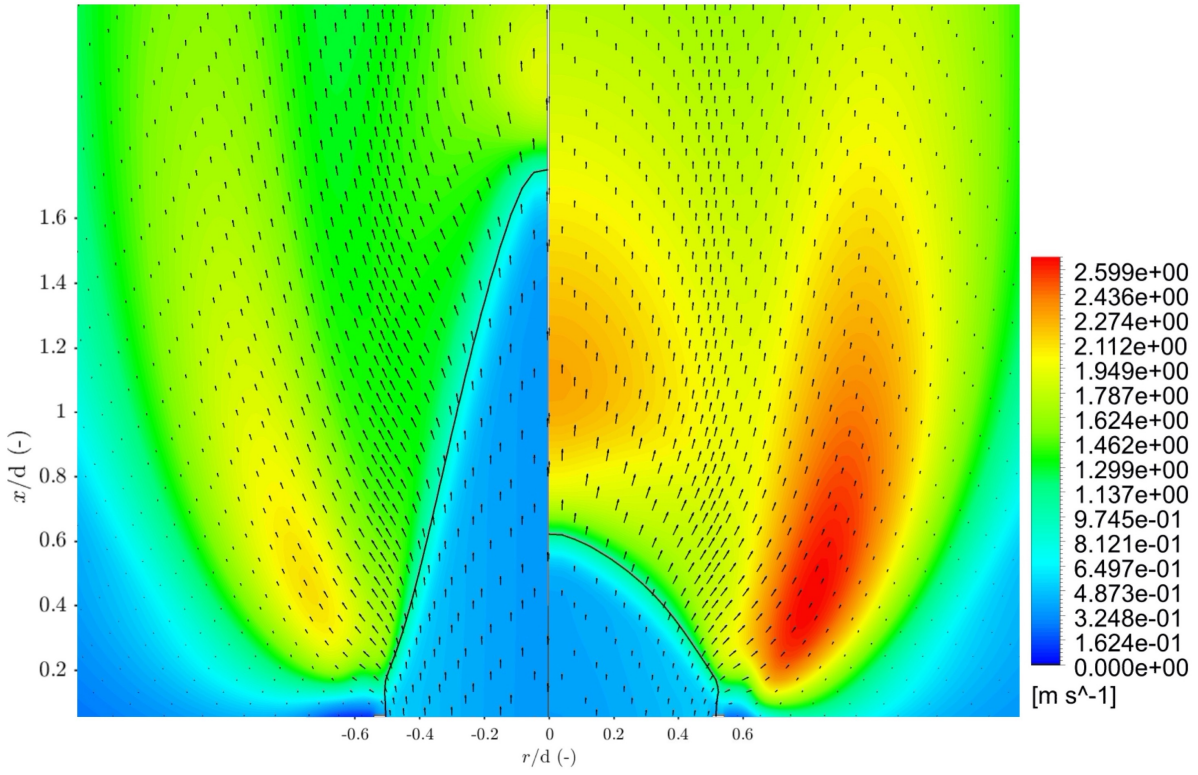

Figure 5.46: Comparison of root mean square turbulent velocity fluctuation contours, including flame front location corresponding to c = 0.2 and flow velocity vector field for flame 9. Turbulent flame speed relation: Left hand side; Zimont and right hand side; Cai et al.

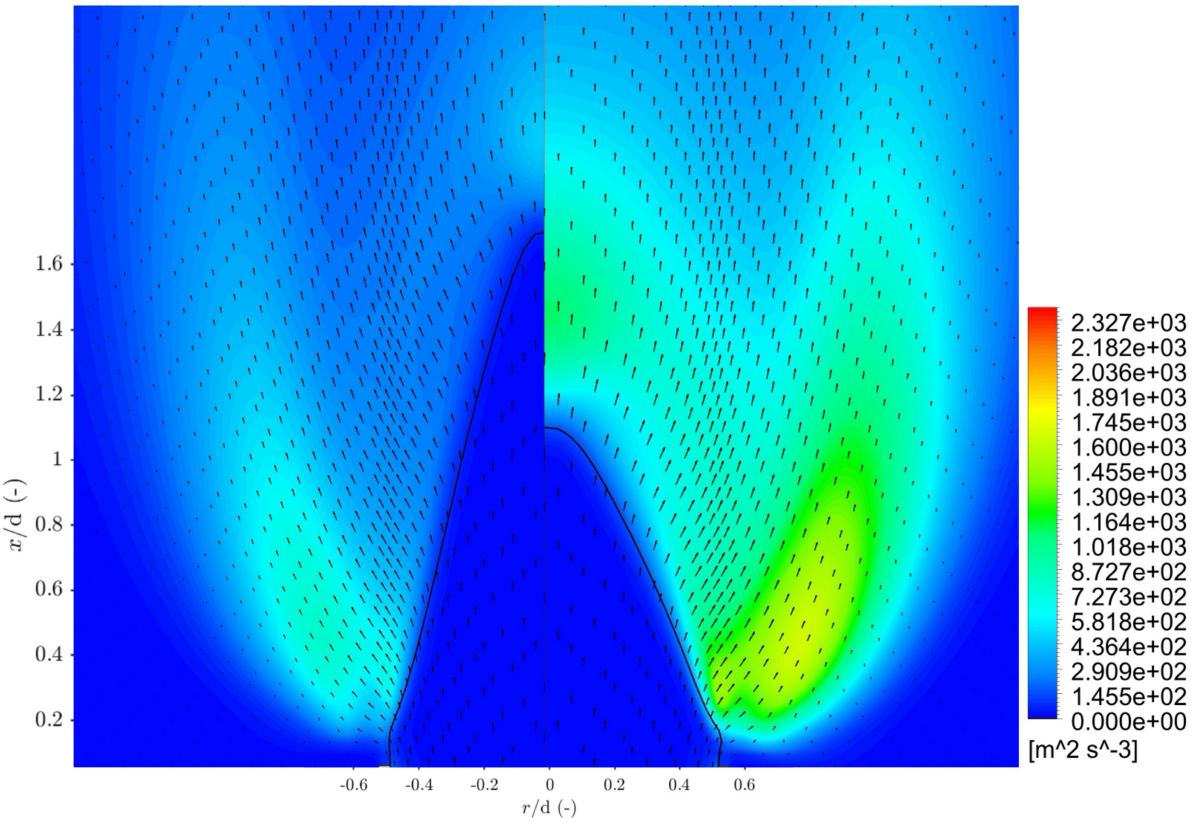

Figure 5.47: Comparison of turbulent dissipation rate contours, including flame front location corresponding to c = 0.2 and flow velocity vector field for flame 9. Turbulent flame speed relation: Left hand side; Zimont and right hand side; Dinkelacker et al.

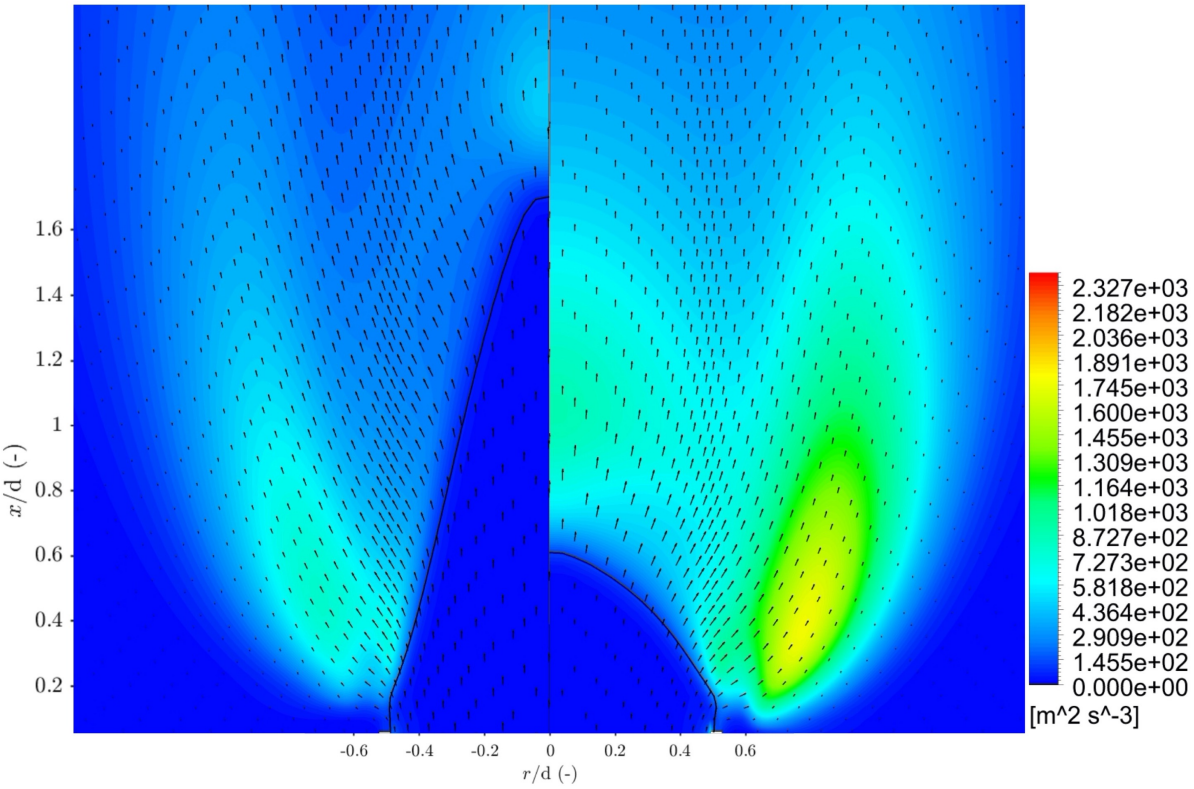

Figure 5.48: Comparison of turbulent dissipation rate contours, including flame front location corresponding to c = 0.2 and flow velocity vector field for flame 9. Turbulent flame speed relation: Left hand side; Zimont and right hand side; Cai et al.

Turbulent flame speed sensitivity

Earlier the influence of u' and l_t was explained. In short the higher the value of the exponents, the greater the influence of u' or l_t on the turbulent flame speed. In figure 5.49 the relations between S_t, u' and l_t are plotted along the flame front locations corresponding to c = 0.2, also seen in figures 5.40 and 5.41. Again the starting point of the figures where S_t/S_L^0 is equal to one is at the pipe wall, as there is no combustion. And S_t is equal to S_L^0. From there the plotted curves follow the flame front to the pipe axis. Looking at figure 5.49 it can be seen that the correlation proposed by Cai et al. has the least amount of changes in u' values over the flame front. The other two correlations have a similar sensitivity to changes in u'. All three correlations are influenced similarly by the integral length scale, although the largest integral length scales are observed for the case modeled using the Zimont correlation. Which is in line with the results seen on the left side of figure 5.47.

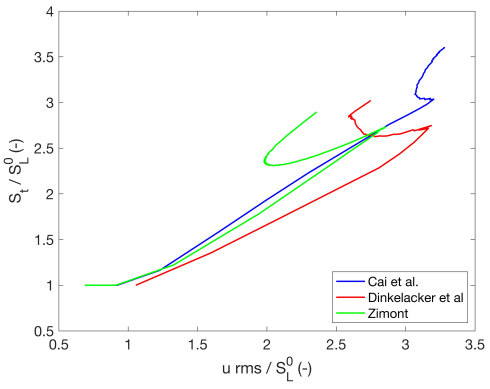

(a) Normalized turbulent flame speed plotted against normalized root mean square velocity.

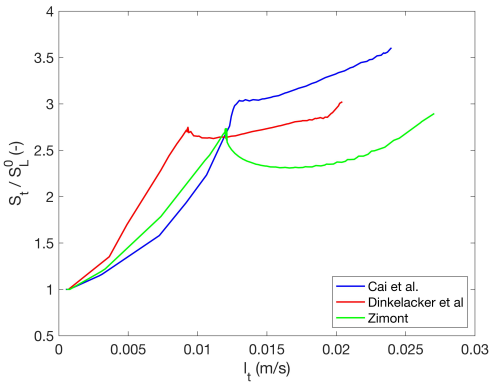

(b) Normalized turbulent flame speed plotted against integral length scale.

Figure 5.49: Normalized turbulent flame speed plots of flame 9 along the flame front location c = 0.2, from the pipe wall to the pipe axis. Data generated using Fluent.

Comparing the results of flame 9 to the results of flame 15, a number of things stand out. Firstly, in flame 9 the correlation proposed by Cai et al. leads to the largest velocity magnitude, but for flame 15 this is the correlation by Dinkelacker et al. However, the mixtures in both flames have a similar unstretched laminar flame speed and the bulk velocity is also of the same magnitude. Therefore it is expected that the unstretched laminar flame speed has a similar effect on both flames for the same correlation. It is also expected that the root mean square turbulent velocity fluctuations upstream of the flame front are of the same order of magnitude, since the bulk velocities are too. This leads to the idea that the difference in sensitivity to u' and the integral length scale, and inclusion of the effective Lewis number are causing the difference. But there is one other factor which so far has not been considered in this analysis. That is the difference in adiabatic flame temperature. Flame 9 and 15 have adiabatic flame temperatures of 1755°C and 2047°C respectively. This affects the increase in velocity across the flame front and the root mean square turbulent velocity fluctuations. Which could explain why the correlation proposed by Cai et al. leads to largest velocity magnitude for flame 9, but for flame 15 this is the correlation by Dinkelacker et al.

Conclusion

Taking everything into account, the shorter cone and larger cone angle when modeling flame 9 with the correlations proposed by Dinkelacker et al. and Cai et al seems to be caused by a combination of factors. In both cases the shorter cone and larger cone angle is due to a higher turbulent flame speed in comparison to the flame modeled using the Zimont correlation. Another important factor is the region with a high turbulent flame speed along the center line around x/d = 1.4 for Dinkelacker et al. correlation and around x/d = 1.1 for the Cai et al. correlation. This high turbulent flame speed region is more pronounced in the cases modeled using the new correlations and seems to be a driving factor in shortening the cone length, since it also influences the source term. In the case modeled using the Cai et al. correlation, the increased distance between the iso-lines of the progress variable values of 0.1 and 0.9 also plays a role. While this decreases the gradient of the progress variable, it increases

the size of the area where the flow field is influenced by the source term. The main cause of the higher turbulent flame speed observed when modeling both new correlations is the higher influence of u' due to higher turbulent velocity fluctuations. This can also be formulated from another point of view, using the flame flow interaction. Meaning that new correlations generate more turbulent velocity fluctuations compared to the case modeled using the Zimont correlation. Other important factors are the inclusion of the effective Lewis number and the adiabatic flame temperature.

5.3.4. Flame 9: Experimental validation

As previously mentioned, ideally one would compare the numerical data with experimental data. By comparing the numerical results to experimental data, it will be easier to determine whether the correlations by Dinkelacker et al. and Cai et al. are an improvement with respect to the Zimont correlation. Of the flames for which experimental data has been published by Faldella [30] flame 9 is the only flame that could be modeled using all three turbulent flame speed correlations. Therefore this section is dedicated to comparing all three correlations to the experimental results for flame 9. As mentioned, flame 9 uses the 39.2 mm inner diameter burner, a bulk velocity of 6.00 m/s, an equivalence ratio of 0.6 and the fuel composition is 80 vol.% hydrogen. The results will be compared using the normalized velocity field, the flame front location and the pressure gradients along different radial locations. The normalized velocity fields of the numerical results are the same normalized velocity fields seen earlier in this subsection. Only in this case the legends and colour ranges differ for the used correlations. This makes for a easier comparison to the experimentally determined normalized velocity field. The numerically determined flame front locations are again based on a progress variable value of 0.2. The experimentally determined flame front was determined using the method described in subsection 5.2.2, meaning the flame front is shown as a line. But instead of the density, the full width at half width maximum (FWHM) seeding density determined by means of Mie-scattering measurement was used. The pressure gradient has been determined using the same method described in subsection 5.2.3. In comparison to the pressure gradient data of flame 1 seen in figure 5.19c, the experimental data of the pressure gradient for flame 9 is messy and shows some outliers. Especially along the radial location r/d = 0. Therefore it was decided to only plot along the radial locations 0.1, 0.2 and 0.3 as seen in figure 5.51. The reason for these outliers is unknown.

Zimont vs Experiments

In subsection 5.2.2 it was concluded that the k-epsilon model with enhanced wall treatment in combination with the Zimont turbulent flame speed correlation already resulted in a flame cone angle which matched the experimental flame cone angle fairly well. The flame cone angle was slightly underestimated by the numerical model. This can also be seen in figure 5.50. In addition, the flame cone of the flame modeled using the Zimont correlation is slightly longer than the experimental flame cone, which is as expected since the flame cone angle is underestimated. Looking at the normalized velocity fields it can be seen that the velocity magnitude downstream of the flame front has values of 1.2 to 1.4 in both the numerical and experimental results. Moreover, the pressure gradient determined using the Zimont correlation seen in figure 5.51 follows the same trend as the experimentally determined pressure gradient seen in the figure, but the values are underestimated. Also the maxima and minima are observed at different locations, this can attributed to the difference in flame shape. All things considered it can be concluded that for flame 9 the Zimont correlation is able to predict the turbulent flame speed, the flow field and flame shape rather good.

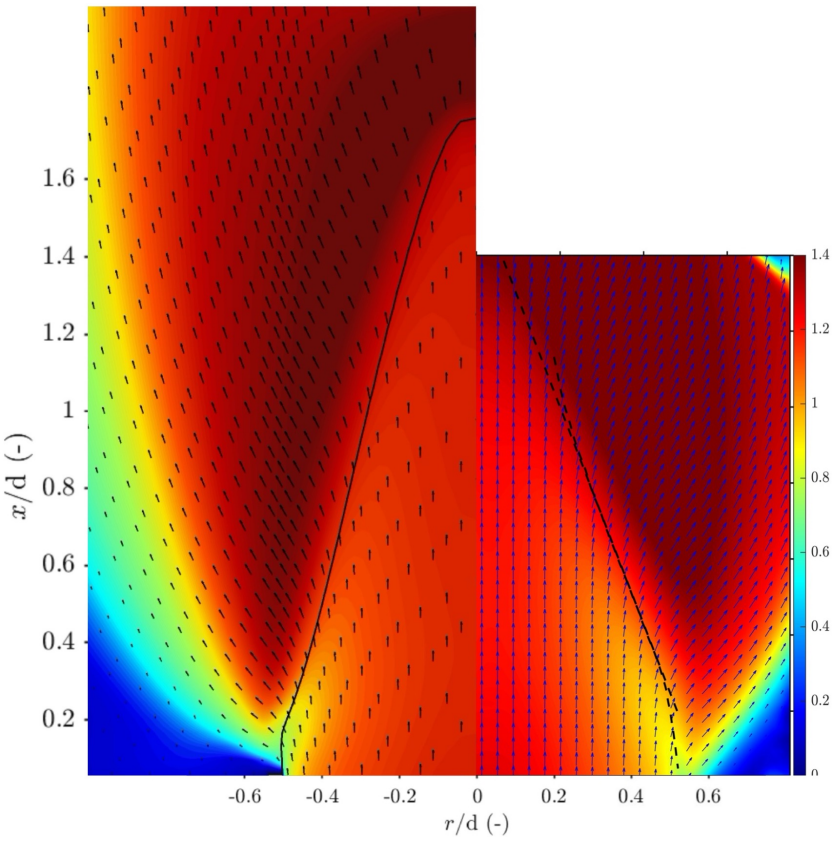

Figure 5.50: Comparison of velocity field u/U_b and flame front location for flame 9. Left hand side; Zimont and right hand side; Experimental results.

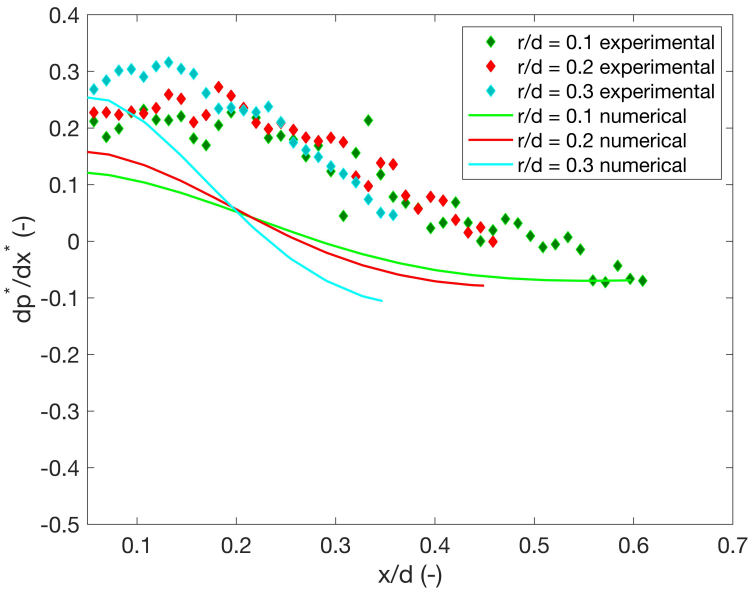

Figure 5.51: Comparison of experimental and numerical pressure gradient of flame 9. Numerically determined using the turbulent flame speed correlation proposed by Zimont.

Dinkelacker et al. vs Experiments

In figure 5.52 the normalized velocity field and flame front location of the flame modeled using the correlation by Dinkelacker et al. are compared to the experimental data. It can be seen that the flame cone angle of the numerically modeled flame is larger than the experimental flame cone angle. Resulting in a shorter flame cone. Looking at the normalized velocity field it can be seen that downstream of the flame front the numerical result shows a much larger area with values of 1.4 compared to the experimental result. It should be noted that the max value in the used legend is 1.4, in reality the numerical result shows values up to 1.7. Evaluating the pressure gradient determined using the Dinkelacker et al. correlation, seen in figure 5.53. It stands out that the pressure gradient along the line r/d = 0.3 has a higher maximum and lower minimum than the experimentally determined pressure gradient seen in the figure along the same line. The maxima observed along the lines r/d = 0, 0.1 and 0.2 are similar, but the minima are significantly lower. Furthermore, the maxima and minima are observed at different locations, this can be attributed to the difference in flame shape. The observed jump in the numerically determined pressure gradient is greater than the experimentally determined jump in pressure gradient. The combination of the larger flame cone angle, shorter flame cone, higher velocity magnitude downstream of the flame front and the greater jump in pressure gradient observed in the flame modeled using the Dinkelacker et al. correlation with respect to the experimental results leads to the conclusion that the Dinkelacker et al. correlation overpredicts the turbulent flame speed for flame 9 and is not an improvement compared to the Zimont correlation.

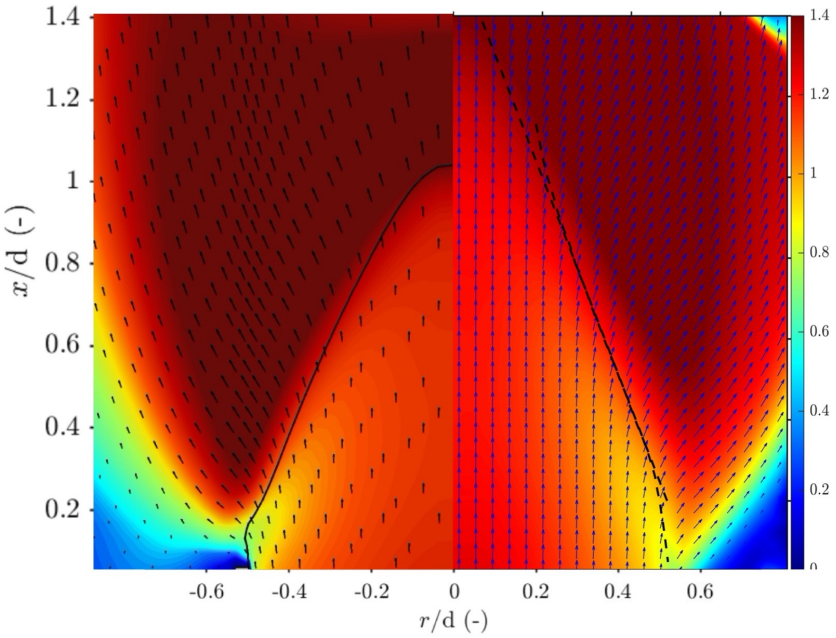

Figure 5.52: Comparison of velocity field u/U_b and flame front location for flame 9. Left hand side; Dinkelacker et al. and right hand side; Experimental results. The maximum value shown by the color range is 1.4, however in case of the Dinkelacker et al. correlation higher values are observed (up to 1.7, see figure 5.40), values higher than 1.4 are shown with the same color as 1.4.

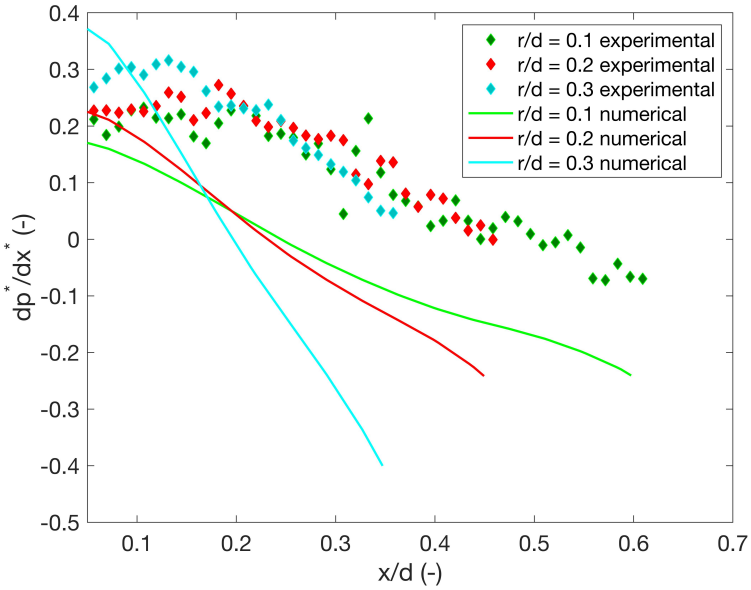

Figure 5.53: Comparison of experimental and numerical pressure gradient of flame 9. Numerically determined using the turbulent flame speed correlation proposed by Dinkelacker et al.

Cai et al. vs Experiments

The normalized velocity field and flame front location of the flame modeled using the correlation by Cai et al. are compared to the experimental data in figure 5.54. It can be seen that the flame cone angle of the numerically modeled flame is larger than the experimental flame cone angle. Resulting in a shorter flame cone. Looking at the normalized velocity field it can be seen that downstream of the flame front the numerical result shows a much larger area with values of 1.4 compared to the experimental result. It should be noted that the max value in the used legend is 1.4, in reality the numerical result shows values up to 2.0. Evaluating the pressure gradient determined using the Cai et al. correlation, seen in figure 5.53. It stands out that the pressure gradient along the line r/d = 0.3 has a higher maximum and similar minimum with respect to the experimentally determined pressure gradient seen in the figure along the same line. The maxima observed along the lines r/d = 0, 0.1 and 0.2 are slightly higher, while the minima along the lines r/d = 0.1 and 0.2 are similar. Overall the numerically determined pressure gradient actually matches the experimentally determined pressure gradient really well. However, the comparison of the numerical and experimental pressure gradients should be considered with caution as the flame shapes are highly different. Perhaps one should even wonder if the matching results have any significance or are just a coincidence. In conclusion, the combination of the larger flame cone angle, shorter flame cone and the higher velocity magnitude downstream of the flame front observed in the flame modeled using the Cai et al. correlation with respect to the experimental results leads to the conclusion that the Cai et al. correlation overpredicts the turbulent flame speed for flame 9 and is not an improvement when compared to the Zimont correlation.

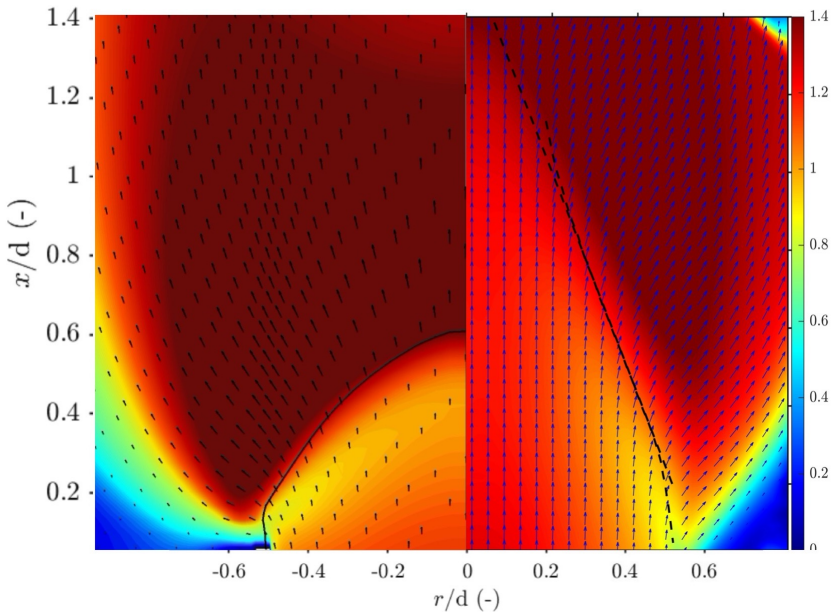

Figure 5.54: Comparison of velocity field u/U_b and flame front location for flame 9. Left hand side; Cai et al. and right hand side; Experimental results. The maximum value shown by the color range is 1.4, however in case of the Cai et al. correlation higher values are observed (up to 2.0, see figure 5.41), values higher than 1.4 are shown with the same color as 1.4.

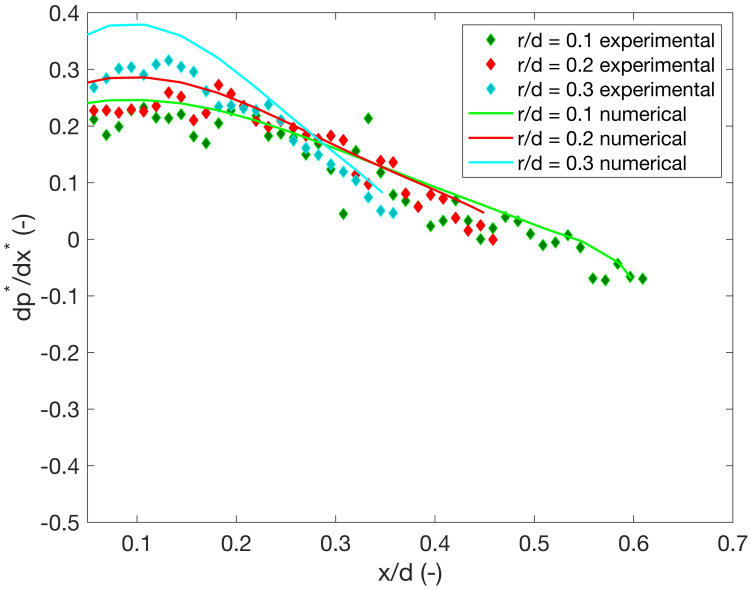

Figure 5.55: Comparison of experimental and numerical pressure gradient of flame 9. Numerically determined using the turbulent flame speed correlation proposed by Cai et al.

5.3.5. Conclusion on the influence of the turbulent flame speed correlations

The initial goal of implementing other turbulent flame speed correlations, was to improve the prediction of flame flashback and flame shape with respect to the Zimont correlation. Based on the sensitivity analysis in subsection 3.2.6, it was expected that the correlation of Dinkelacker et al. would lead to a lower flame speed and thus shorter flame cone and a smaller flame cone angle for both the low and high vol.% hydrogen flames. Which is the opposite of what can be seen in the results. However it should be noted the sensitivity analysis was fairly simple and did not consider any feedback of the flame on the turbulent flow field and neither included expansion due to heat release.

First of it should be stated that of the flames seen in table 5.2 the Zimont model was able to stable (i.e. without the occurance of flashback) model 7 out of the 9 flames. Using the correlation of Cai et al. 2 out of 9 flames (flame 7 and 9) could be modeled stably, and using the correlation of Dinkelacker et al. only 1 out of 9. Which was already an indication that the new correlations would predict shorter flame cones and therefore calculated higher turbulent flame speeds. Furthermore the flame cone angle of flame 9 modeled using the Zimont correlation already matched the experimental results quite good. Taking into account that the two correlations are not able to model most of the experimental flames. And that the flame cone angle calculated using the two new correlations corresponded less well with the experimentally determined flame cone angle than the cone angle determined using the Zimont model. It can be stated that the turbulent flame speed correlations by Dinkelacker et al. and Cai et al. do not perform better for calculating the flame shape.

The flashback propensity was already estimated fairly well in the hydrogen flames with a content up to 40 vol.% hydrogen by the Zimont model. For the flames with 60 and 80 vol.% hydrogen content the bulk velocity at which flashback occurs was slightly underestimated. And for the 100 vol.% hydrogen flames, with an equivalence ratio greater than 0.65 the bulk velocity at which flashback occurs was overestimated. The correlations of Dinkelacker et al. and Cai et al. predict shorter flame cones, resulting in a greater velocity increase over the flame front than observed when modeling with the Zimont correlation. This increase is higher than the amount by which the bulk velocity at flashback is underestimated by the Zimont model at 60 and 80. vol.% hydrogen content. A further increase in predicted turbulent flame speed for 100 vol.% hydrogen is definitely not an improvement since the Zimont model already overestimated the bulk velocity at which flashback occurs. Therefore it can also be stated that the turbulent flame speed correlations by Dinkelacker et al. and Cai et al. do not perform better for predicting the flashback propensity.

The results show that flames 14, 15 and 9 all have a shorter cone and a larger cone angle when modeling with either the correlation proposed by Dinkelacker et al. or Cai et al. instead of the Zimont correlation. In case of flame 14 the correlation by Dinkelacker et al. led to a higher flow velocity both downstream and upstream of the flame in comparison to the Zimont correlation. The higher velocity was caused by an increased turbulent flame speed. But also by the effect of turbulent diffusion which increased the value of the progress variable upstream of the flame and therefore accelerated the flow. For flames 15 and 9 the shorter flame cone and larger cone angle when modeled with the Dinkelacker et al. correlation was caused by an increased turbulent flame speed. Which led to a higher source term of the progress variable with respect to the Zimont correlation.

As mentioned the correlation proposed by Cai et al. led to a shorter cone and a larger cone for all the modeled flames. The results showed that the shorter flames were caused by different factors than the shorter flames modeled with the Dinkelacker et al. correlation. For all three flames, the observed turbulent flame speed values in the region between the iso-lines of the progress variable was higher than the values observed in the cases modeled using the Zimont correlation. But the source term of the progress variable along the pipe axis always had the lowest maximum when modeled with the correlation proposed by Cai et al. The lower source term was due to a larger distance between the iso-lines of the progress variable and therefore a smaller gradient. The greater distance between the iso-lines allowed the source term to have an influence on a larger area of the flow field. Therefore, despite the lower source term, the flames all had shorter cones and larger cone angles than the flames modeled with the Zimont correlation.

The three turbulent flame speed correlations were developed by the authors from different viewpoints. The Zimont correlation was originally related to experimental data and was tuned for numerical use by adding the empirical constant of 0.52 by which the correlation is multiplied. The correlation proposed by Dinkelacker et al. was specifically developed for numerical use based on a flame surface

density approach. On the other hand the correlation proposed by Cai et al. was based on experimental data and defined at c = 0.5. Furthermore the authors stated that the correlation was able to predict experimental data as well as turbulent burning velocities measured using both turbulent Bunsen flames and expanding flames at high pressures. This means that in the cases modeled with the correlation by Cai et al. the reason for higher turbulent flame speed is probably related to the definition of the reference point of the turbulent flame speed, as indicated by Dinkelacker and Hölzler [21]. In experiments the turbulent flame speed is correlated to the local flow conditions just in front of the flame. While in the numerical study, the turbulent flame speed is used as a field variable and calculated at every position. This means the turbulent flame speed is also dependent on the turbulence intensity inside the flame, where the calculated turbulence intensity is larger than in front of the flame. This leads to higher (than intended) values of the turbulent flame speed if the correlation is used numerically, without extra empirical fit parameters. Including additional fit constants might improve the results when modeling with the correlation proposed by Cai et al. in combination with a turbulent flame speed closure approach based on the flame surface density. However this should not be done without considering the actual experimental data.

6

Conclusion and Recommendations

6.1. Conclusion

Hydrogen technology in combination with gas turbine technology could play a major role in the energy transition. It could contribute to solving the imbalance between fluctuating renewable power supply and power demand. Furthermore, carbon dioxide emissions could be eliminated and by using lean premixed combustion NOx emissions can also be kept to a minimum. Using hydrogen based fuels in premixed combustion applications also has drawbacks. Premixed hydrogen-air mixtures are especially prone to boundary layer flashback due to the high reactivity of hydrogen. Which led to the objective of this thesis to numerically predict flame predict flame flashback in premixed tube burners with turbulent flow and high hydrogen content. More specifically, boundary layer flashback of turbulent jet flames of hydrogen-methane-air mixtures in the TU Delft tube burner was investigated.

In order to achieve this objective in a structured way, this thesis has been divided into a number of chapters. After the introduction, a chapter was presented in which relevant general theory on fluid flow, CFD and combustion was explained. Followed by a chapter in which different combustion models were presented. Then the used numerical setup used in this study was presented. And finally the results of this study were presented and discussed. The results were divided into three sections:

- Identification of the conditions leading to flashback.
- Experimental validation.
- Evaluation of turbulent flame speed correlations.

The first section was dedicated to understanding the flashback process when modeled with the standard $k-\epsilon$ turbulence model with enhanced wall treatment and the Zimont Turbulent Flame Speed Closure combustion model.

The second section of was dedicated to comparing the numerical results to experimental data presented by Faldella [30].

The final section evaluated the turbulent flame speed correlations selected in the literature review by comparing numerical results as well as experimental data.

The results presented in the first section showed that the standard $k-\epsilon$ turbulence model with enhanced wall treatment combined with the Zimont Turbulent Flame Speed Closure combustion model was able to model flame flashback.

It stood out that during the approach to flashback conditions (i.e. by lowering the bulk velocity) the flame front increased to be more parallel to the radial plane of the pipe at a radial location almost equal to the radius of the pipe.

Once it was determined that flashback could be modeled, multiple hypotheses were tested to determine a method which enables predicting flame flashback in advance. Some were confirmed and this led to multiple findings. Firstly, the gradient with respect to the x-axis of the pressure coefficient showed the highest maximum and lowest minimum for the flame closest to flashback. Furthermore the radial velocity increased with respect to the bulk velocity during the approach to flashback conditions.

On the other hand the wall shear stress did not go to zero during the approach to flashback conditions. Also the flow velocity did not become lower than the turbulent burning velocity of the flame near flashback conditions. And finally it was confirmed that a streamline close to the pipe wall will be deflected stronger if a flame is closer to flashback.

Although some of the hypotheses were confirmed, this did not provide a method of predicting flame flashback in advance. This led to the concluding hypothesis that the flashback process will only start after passing a threshold and is self-amplifying once this threshold has been passed. The concluding hypothesis could neither be confirmed or denied based on the presented results. However the hypothesis appeared to be a logical explanation.

The second section of was dedicated to determining how well the numerical results match with experimental data. The results included the flame regime map, the flame cone angles and flame induced adverse pressure gradients of multiple flames.

Based on the flame regime map it was concluded that a higher volumetric concentration hydrogen in the fuel mixture led to a higher flashback propensity in both the numerical and experimental results. Furthermore the behaviour for the lower volumetric concentrations of hydrogen being 0%, 20% and 40% was similar. When the volumetric concentration hydrogen was increased even further to 60 vol.% hydrogen the change in flashback propensity was also not very strong yet. But at 80%, and in particular at 100% hydrogen content in the fuel, the propensity changed drastically. Furthermore it stood out that the numerical model underestimated the bulk velocity of the incoming mixture for almost all fuel mixtures and equivalence ratios. However, considering the simplicity of the used models, the fact that the numerical model was able to capture that an increase in the hydrogen concentration in the fuel led to an increased flashback propensity was already exceptional on itself.

The numerically determined flame cone angles were compared to experimental data for flames with 60, 80 and 100 vol.% hydrogen. The numerically determined 60 and 80 vol.% hydrogen flames had longer flame cones with smaller flame cone angles compared to the experimentally determined values. This was as expected, since the results of the flame regime map showed that the bulk velocity near flashback was underestimated for almost all flames. The numerically determined flame cone angles for the 100 vol.% hydrogen flames all were larger compared to the experimentally determined values. The geometries for the 100 vol.% hydrogen flames in the flame regime map and flame cone angles differ. The flame cone angle geometry employed a larger diameter, which resulted in a higher Reynolds number. The increased turbulence also increased the turbulent flame speed and therefore explained the different behaviour of the cone angles of the 100 vol.% hydrogen flames.

Experimental data on the adverse pressure gradient was only available for two flames that could not be modeled with the numerical model, since the numerical model predicted the flames to show flashback. Therefore four other comparable flames were modeled to compare the adverse pressure gradient. The adverse pressure gradient is responsible for the flame flow interaction which causes the approaching flow to be deflected and retarded. The strongest effect of the adverse pressure gradient was seen for a flame close to flashback, as was also seen in the first section of this chapter. This was due to the flame front being more parallel to the pipe outlet. The numerically determined adverse pressure gradient was underestimated with respect to the experimental pressure gradient for the flames close to flashback.

The final section focused on turbulent flame speed correlations proposed by Dinkelacker et al. [22] and Cai et al. [16] which were selected in the literature review. The correlations were expected to perform better than the Zimont correlation for flames with high hydrogen content since they were derived specifically for fuel mixtures containing hydrogen and included Lewis number effects. The correlations were evaluated by comparing numerical results as well as experimental data of three flames with fuel mixtures containing 20, 60 and 80 vol.% hydrogen and having equivalence ratios of 0.8, 0.8 and 0.6 respectively. The results showed all flames had a shorter cone and a larger cone angle when modeling with either the correlation proposed by Dinkelacker et al. or Cai et al. instead of the Zimont correlation. It was concluded that the turbulent flame speed correlations by Dinkelacker et al. and Cai et al. did not perform better for calculating the flame shape or for predicting the flashback propensity.

The worse performance of the correlations was caused by different factors. For the flames modeled using the Dinkelacker et al. correlation the turbulent flame speed was higher than the turbulent flame speed modeled for the same flames with the Zimont correlation. This led to an increased source term of the progress variable. For the flames modeled using the Cai et al. correlation, the worse performance

was explained by a higher turbulent flame speed and an increased distance between the iso-lines of the progress variable corresponding to 0.1 and 0.9. This decreased the source term of the progress variable, but allowed the source term to have an influence on a larger area of the flow field.

Furthermore it should be noted that the Zimont and Dinkelacker et al. correlation were optimized for CFD use by the authors while the Cai et al. correlation focused on validating experimental data and was defined at the flame front location where the progress variable is equal to 0.5. In future attempts to implement turbulent flame speed correlations in CFD in combination with a flamelet approach, it must be established with certainty that the correlations are optimized for CFD and thus not only defined for a single value of the progress variable.

6.2. Recommendations

In this study it was found that the standard $k-\epsilon$ turbulence model with enhanced wall treatment combined with the Zimont Turbulent Flame Speed Closure combustion model was able to model flame flashback and was able to capture that an increase in the hydrogen concentration in the fuel led to an increased flashback propensity. However this study focused on a simple unconfined tube burner geometry. For further research it would be interesting to see if the numerical model is still able to predict flame flashback and the trend of increased flashback propensity for higher hydrogen concentrations in a more complex geometry. Several options can be devised for a more complex geometry. For example an option could be a confined burner geometry, which could be created by adding a quartz tube with a larger inner diameter to the tube outlet. Other options could be to use burners encountered in gas turbines such as can, cannular and annular combustors optionally with swirl stabilized combustion.

To perform such an analysis first flame regime maps should be created experimentally. Meaning that the bulk velocity as function of equivalence ratio at flashback conditions for different fuel mixture compositions should be mapped for the more complex geometries. Thereafter the flame regime maps should be determined using the numerical model presented in this study, to evaluate whether the numerical model still works for a more complex case.

Other recommendations for future research includes:

- Extend the section on the evaluation of turbulent flame speed correlations. Select (and test) other turbulent flame speed correlations derived specifically for turbulent premixed flames with high hydrogen content with the option to include Lewis number effects, but the selected correlations must be optimized for the flame surface density approach to close the source term.
- Perform the numerical study with a RANS turbulence model that does not assume isotropic turbulence such as the Reynolds Stress Transport (RST) model. Or use a Large Eddy Simulation (LES) method. Since the turbulence intensity is correlated with the turbulent flame speed and therefore the source term of the progress variable. This could lead to improved results and a better match with the experimental data.
- Redo the experimental validation or perform the entire numerical study while including flame stretch effects and assume non-adiabatic conditions. Chong et al. [78] argue that the prediction of turbulent premixed flames under non-adiabatic conditions can be improved by considering the combined effects of strain and heat loss on reaction rates. They follow the idea that in order to properly predict the flame shape, the combined influence of strain and heat loss should be taken into account by the combustion model. This effect can be taken into account with the combustion modeling approach used in this study by multiplying the source term with a stretch factor G, but this does not consider the enhanced sensitivity to strain under non-adiabatic conditions. Chong et al. state that a possible consequence of ignoring the effects of heat losses are the incorrect predictions of the flame shape. They used an enhanced combustion model where the effects of strain and heat losses are taken into account. They state that the flame showed better agreement in the spatial and axial heat release distribution, the flame length was similar to the length observed in the experiment and the flow field was also improved
- A comparison between numerical modeling of rich and lean H2-air flames would allow further assessing the effect of the inclusion of Lewis number effects in the turbulent flame speed correlations.

A

Appendix A

A.1. Turbulent flame speed UDF

A.1.1. Dinkelacker et al.

```
    #include ”udf.h”
#include ”sg_pdf.h” /* not included in udf.h so must include here */
#include ”mpi.h”
#include ”math.h”

DEFINE_TURB_PREMIX_SOURCE
(turb_flame_src_dinkelacker,c,t,turb_flame_speed,source)
{
real up = TRB_VEL_SCAL(c,t);
real ut,sl0,le,Ret,grad_c,rho_u,Xl,DV[ND_ND],mulam,rho,lx,eps,k;

eps = C_D(c,t);
k = C_K(c,t);
lx = pow(0.09,0.75)*pow(k,1.5)/eps;
mulam = C_MU_L(c,t);
rho = C_R(c,t);

sl0 = C_LAM_FLAME_SPEED(c,t);
le=0.655;
Calculate_unburnt_rho_and_Xl(t,&rho_u,&Xl);

if(NNULLP(THREAD_STORAGE(t,SV_PREMIXC_G)))
{
NV_V(DV, =, C_STORAGE_R_NV(c,t,SV_PREMIXC_G));
grad_c = sqrt(NV_DOT(DV,DV));
}

Ret = rho*up*lx/mulam;

ut = sl0 + (0.46*sl0*exp(-1*(le-1))*pow(Ret,0.25)*pow((up/sl0),0.3));
*turb_flame_speed = ut;
*source = rho_u*ut*grad_c;
}
```

A.1.2. Cai et al.

```
#include ”udf.h”
#include ”sg_pdf.h” /* not included in udf.h so must include here */
```

```
#include "mpi.h"
#include "math.h"

DEFINE_TURB_PREMIX_SOURCE(turb_flame_src_cai,c,t,turb_flame_speed,source)
{
real up = TRB_VEL_SCAL(c,t);
real ut,sl0,le,Ret,grad_c,rho_u,Xl,DV[ND_ND],mulam,rho,lx,eps,k;

eps = C_D(c,t);
k = C_K(c,t);
lx = pow(0.09,0.75)*pow(k,1.5)/eps;
mulam = C_MU_L(c,t);
rho = C_R(c,t);

sl0 = C_LAM_FLAME_SPEED(c,t);
le=0.96;
Calculate_unburnt_rho_and_Xl(t,&rho_u,&Xl);

if(NNULLP(THREAD_STORAGE(t,SV_PREMIXC_G)))
{
NV_V(DV, =, C_STORAGE_R_NV(c,t,SV_PREMIXC_G));
grad_c = sqrt(NV_DOT(DV,DV));
}

Ret = rho*up*lx/mulam;

ut = (sl0 + (0.164*sl0*pow(Ret,0.66)*pow(le,-1.32)));
*turb_flame_speed = ut;
*source = rho_u*ut*grad_c;
}
```

A.2. Validation of turbulent flame speed UDF implementation

A.2.1. Velocity fields

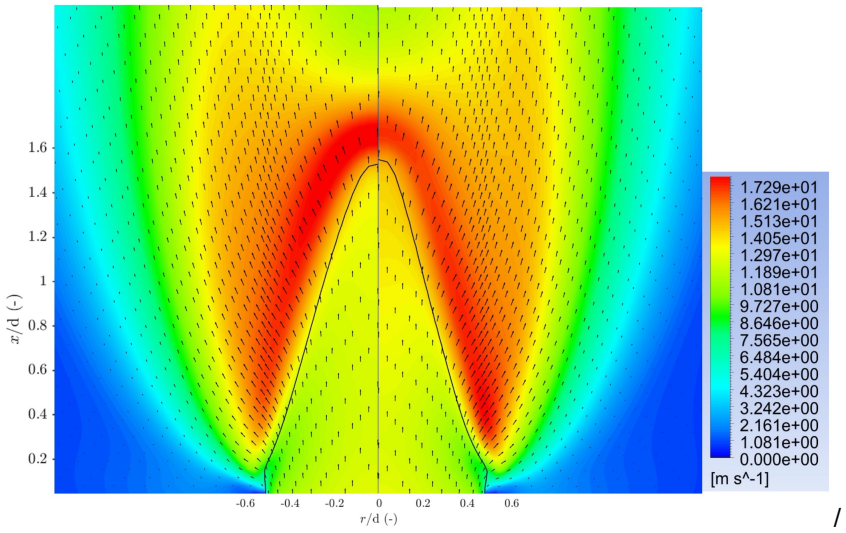

Figure A.1: Velocity fields, flame front locations and velocity vector fields compared for the Zimont correlation provided in Fluent and the Zimont correlation implemented in Fluent using a UDF. Left; Zimont provided in Fluent, Right; Zimont implemented in Fluent using UDF.

A.2.2. Zimont UDF code

```
#include ”udf.h”
#include ”sg_pdf.h” /* not included in udf.h so must include here */
#include ”mpi.h”
#include ”math.h”

DEFINE_TURB_PREMIX_SOURCE(turb_flame_src_cai,c,t,turb_flame_speed,source)
{
real ut,up,sl0,alpha,grad_c,rho_u,Xl,DV[ND_ND],rho,lx,eps,k;

eps = C_D(c,t);
k = C_K(c,t);
up = pow((2/3)*k, 0.5);
lx = pow(0.09,0.75)*pow(k,1.5)/eps;
rho = C_R(c,t);

sl0 = C_LAM_FLAME_SPEED(c,t);
alpha = 3.8141E-05;
Calculate_unburnt_rho_and_Xl(t,&rho_u,&Xl);

if(NNULLP(THREAD_STORAGE(t,SV_PREMIXC_G)))
{
NV_V(DV, =, C_STORAGE_R_NV(c,t,SV_PREMIXC_G));
grad_c = sqrt(NV_DOT(DV,DV));
}

ut = 0.52*pow(up,0.75)*pow(sl0,0.5)*pow(alpha,-0.25)*pow(lx,0.25);
*turb_flame_speed = ut;
*source = rho_u*ut*grad_c;
}
```

Bibliography

[1] R Addabbo, JK Bechtold, and Moshe Matalon. Wrinkling of spherically expanding flames. *Proceedings of the Combustion Institute*, 29(2):1527–1535, 2002.

[2] BA Albrecht, S Zahirovic, RJM Bastiaans, JA Van Oijen, and LPH De Goey. A premixed flamelet-pdf model for biomass combustion in a grate furnace. *Energy & fuels*, 22(3):1570–1580, 2008.

[3] Riccardo Amirante, Elia Distaso, Paolo Tamburrano, and Rolf D Reitz. Laminar flame speed correlations for methane, ethane, propane and their mixtures, and natural gas and gasoline for spark-ignition engine simulations. *International Journal of Engine Research*, 18(9):951–970, 2017.

[4] *ANSYS Fluent Theory Guide*. ANSYS, Inc., Canonsburg, PA 15317, 15.0 edition, November 2013.

[5] Wm T Ashurst, N Peters, and MD Smooke. Numerical simulation of turbulent flame structure with non-unity lewis number. *Combustion science and technology*, 53(4-6):339–375, 1987.

[6] MJ Assael, S Mixafendi, and William A Wakeham. The viscosity and thermal conductivity of normal hydrogen in the limit of zero density. *Journal of physical and chemical reference data*, 15(4):1315–1322, 1986.

[7] Georg Baumgartner, Lorenz R Boeck, and Thomas Sattelmayer. Experimental investigation of the transition mechanism from stable flame to flashback in a generic premixed combustion system with high-speed micro-piv and micro-plif combined with chemiluminescence imaging. In *Turbo Expo: Power for Land, Sea, and Air*, volume 56680, page V04AT04A047. American Society of Mechanical Engineers, 2015.

[8] A.C. Benim and K.J. Syed. *Flashback Mechanisms in Lean Premixed Gas Turbine Combustion*. Elsevier Science, 2014. ISBN 9780128008263. URL `https://books.google.nl/books?id=o3ODBAAAQBAJ`.

[9] Ali Cemal Benim and Björn Pfeiffelmann. Comparison of combustion models for lifted hydrogen flames within rans framework. *Energies*, 13(1):152, 2020.

[10] Ólafur H Björnsson, Sikke Klein, and Joeri Tober. Boundary layer flashback model for hydrogen flames in confined geometries including the effect of adverse pressure gradient. *Journal of Engineering for Gas Turbines and Power*, 2020.

[11] Thirupathi Boningari and Panagiotis G Smirniotis. Impact of nitrogen oxides on the environment and human health: Mn-based materials for the nox abatement. *Current Opinion in Chemical Engineering*, 13:133–141, 2016.

[12] Sabre Bougrine, Stéphane Richard, Andre Nicolle, and Denis Veynante. Numerical study of laminar flame properties of diluted methane-hydrogen-air flames at high pressure and temperature using detailed chemistry. *International journal of hydrogen energy*, 36(18):12035–12047, 2011.

[13] Nicolas Bouvet, Fabien Halter, Christian Chauveau, and Youngbin Yoon. On the effective lewis number formulations for lean hydrogen/hydrocarbon/air mixtures. *International journal of hydrogen energy*, 38(14):5949–5960, 2013.

[14] Derek Bradley, AKC Lau, Malcolm Lawes, and FT Smith. Flame stretch rate as a determinant of turbulent burning velocity. *Philosophical Transactions of the Royal Society of London. Series A: Physical and Engineering Sciences*, 338(1650):359–387, 1992.

[15] Alexander Burcat. Thermochemical data for combustion calculations. In *Combustion chemistry*, pages 455–473. Springer, 1984.

[16] Xiao Cai, Jinhua Wang, Zhijian Bian, Haoran Zhao, Meng Zhang, and Zuohua Huang. Self-similar propagation and turbulent burning velocity of ch4/h2/air expanding flames: Effect of lewis number. *Combustion and Flame*, 212:1–12, 2020.

[17] Sanjay M Correa. A review of nox formation under gas-turbine combustion conditions. *Combustion science and technology*, 87(1-6):329–362, 1993.

[18] Gerhard Damköhler. Der einfluss der turbulenz auf die flammengeschwindigkeit in gasgemischen. *Zeitschrift für Elektrochemie und angewandte physikalische Chemie*, 46(11):601–626, 1940.

[19] S Daniele, P Jansohn, J Mantzaras, and Konstantinos Boulouchos. Turbulent flame speed for syngas at gas turbine relevant conditions. *Proceedings of the Combustion Institute*, 33(2):2937–2944, 2011.

[20] Santanu De, Avinash Agarwal, Swetaprovo Chaudhuri, and Swarnendu Sen. *Modeling and Simulation of Turbulent Combustion*. Springer, 12 2017. ISBN 978-981-10-7409-7. doi: 10.1007/978-981-10-7410-3.

[21] F Dinkelacker and S Hölzler. Investigation of a turbulent flame speed closure approach for premixed flame calculations. *Combustion science and technology*, 158(1):321–340, 2000.

[22] F Dinkelacker, B Manickam, and SPR Muppala. Modelling and simulation of lean premixed turbulent methane/hydrogen/air flames with an effective lewis number approach. *Combustion and Flame*, 158(9):1742–1749, 2011.

[23] J Doherty, P Ngan, J Monty, and M Chong. The development of turbulent pipe flow. *16th Australasian Fluid Mechanics Conference*, 2007.

[24] Ronan Doherty and Mark O'malley. A new approach to quantify reserve demand in systems with significant installed wind capacity. *IEEE Transactions on Power Systems*, 20(2):587–595, 2005.

[25] James F Driscoll. Turbulent premixed combustion: Flamelet structure and its effect on turbulent burning velocities. *Progress in Energy and Combustion Science*, 34(1):91–134, 2008.

[26] P.A. Durbin and B.A.P. Reif. *Statistical Theory and Modeling for Turbulent Flows*. Wiley, 2010. ISBN 9780470972069. URL https://books.google.nl/books?id=qLkOSTmyK_0C.

[27] Tarek Echekki and Epaminondas Mastorakos. *Turbulent combustion modeling: Advances, new trends and perspectives*, volume 95. Springer, 01 2011. ISBN 978-94-007-0411-4. doi: 10.1007/978-94-007-0412-1.

[28] Christian Thomas Eichler. *Flame flashback in wall boundary layers of premixed combustion systems*. Verlag Dr. Hut, 2011.

[29] Jim Eyer and Garth Corey. Energy storage for the electricity grid: Benefits and market potential assessment guide. *Sandia National Laboratories*, 20(10):5, 2010.

[30] Filippo Faldella. Experimental investigation of boundary layer flashback in high h2 concentration turbulent premixed jet flames. master thesis, Delft University of Technolog, 2020. URL http://resolver.tudelft.nl/uuid:ab0c472e-0dd1-4086-8eeb-18ef14ee226e.

[31] Alireza Farhadi, Arno Mayrhofer, Michael Tritthart, Martin Glas, and Helmut Habersack. Accuracy and comparison of standard k-□ with two variants of k-ω turbulence models in fluvial applications. *Engineering Applications of Computational Fluid Mechanics*, 12(1):216–235, 2018.

[32] Sergei A Filatyev, James F Driscoll, Campbell D Carter, and Jeffrey M Donbar. Measured properties of turbulent premixed flames for model assessment, including burning velocities, stretch rates, and surface densities. *Combustion and Flame*, 141(1-2):1–21, 2005.

[33] AB Gallo, JR Simões-Moreira, HKM Costa, MM Santos, and E Moutinho dos Santos. Energy storage in the energy transition context: A technology review. *Renewable and sustainable energy reviews*, 65:800–822, 2016.

[34] David G. Goodwin, Harry K. Moffat, and Raymond L. Speth. Cantera: An object-oriented software toolkit for chemical kinetics, thermodynamics, and transport processes. http://www.cantera.org, 2017. Version 2.3.0.

[35] INGE R. GRAN and BJØRN F. MAGNUSSEN. A numerical study of a bluff-body stabilized diffusion flame. part 2. influence of combustion modeling and finite-rate chemistry. *Combustion Science and Technology*, 119(1-6):191–217, 1996. doi: 10.1080/00102209608951999. URL https://doi.org/10.1080/00102209608951999.

[36] Marcus Herrmann. Numerical simulation of turbulent bunsen flames with a level set flamelet model. *Combustion and flame*, 145(1-2):357–375, 2006.

[37] Vera Hoferichter, Christoph Hirsch, and Thomas Sattelmayer. Analytic prediction of unconfined boundary layer flashback limits in premixed hydrogen–air flames. *Combustion Theory and Modelling*, 21(3):382–418, 2017.

[38] Vera Hoferichter, Christoph Hirsch, and Thomas Sattelmayer. Prediction of confined flame flashback limits using boundary layer separation theory. *Journal of Engineering for Gas Turbines and Power*, 139(2), 2017.

[39] Zuohua Huang, Yong Zhang, Ke Zeng, Bing Liu, Qian Wang, and Deming Jiang. Measurements of laminar burning velocities for natural gas–hydrogen–air mixtures. *Combustion and Flame*, 146 (1-2):302–311, 2006.

[40] IEA. Total primary energy supply by fuel, 1971 and 2018, 2020. URL https://www.iea.org/data-and-statistics/charts/total-primary-energy-supply-by-fuel-1971-and-2018.

[41] WP Jones and Brian Edward Launder. The prediction of laminarization with a two-equation model of turbulence. *International journal of heat and mass transfer*, 15(2):301–314, 1972.

[42] K Kadoya, N Matsunaga, and A Nagashima. Viscosity and thermal conductivity of dry air in the gaseous phase. *Journal of physical and chemical reference data*, 14(4):947–970, 1985.

[43] Alireza Kalantari and Vincent McDonell. Boundary layer flashback of non-swirling premixed flames: Mechanisms, fundamental research, and recent advances. *Progress in Energy and Combustion Science*, 61:249–292, 2017.

[44] Alan R Kerstein, William T Ashurst, and Forman A Williams. Field equation for interface propagation in an unsteady homogeneous flow field. *Physical Review A*, 37(7):2728, 1988.

[45] Toshiaki Kitagawa, Takashi Nakahara, Kosuke Maruyama, Kunihiro Kado, Akihiro Hayakawa, and Shoichi Kobayashi. Turbulent burning velocity of hydrogen–air premixed propagating flames at elevated pressures. *International Journal of Hydrogen Energy*, 33(20):5842 – 5849, 2008. ISSN 0360-3199. doi: https://doi.org/10.1016/j.ijhydene.2008.06.013. URL http://www.sciencedirect.com/science/article/pii/S036031990800726X.

[46] Hideaki Kobayashi, Takashi Tamura, Kaoru Maruta, Takashi Niioka, and Forman A. Williams. Burning velocity of turbulent premixed flames in a high-pressure environment. *Symposium (International) on Combustion*, 26(1):389 – 396, 1996. ISSN 0082-0784. doi: https://doi.org/10.1016/S0082-0784(96)80240-2. URL http://www.sciencedirect.com/science/article/pii/S0082078496802402.

[47] Hideaki Kobayashi, Katsuhiro Seyama, Hirokazu Hagiwara, and Yasuhiro Ogami. Burning velocity correlation of methane/air turbulent premixed flames at high pressure and high temperature. *Proceedings of the Combustion Institute*, 30(1):827 – 834, 2005. ISSN 1540-7489. doi: https://doi.org/10.1016/j.proci.2004.08.098. URL http://www.sciencedirect.com/science/article/pii/S0082078404001511.

[48] Neeraj A Kumar. *Compressibility factors for natural and sour reservoir gases by correlations and cubic equations of state*. PhD thesis, Texas Tech University, 2004.

[49] P.K. Kundu, I.M. Cohen, and D.R. Dowling. *Fluid Mechanics*. Academic Press. Academic Press, 2015. ISBN 9780124059351. URL https://books.google.nl/books?id=uYevoQEACAAJ.

[50] Eric W Lemmon, Marcia L Huber, Daniel G Friend, and Carl Paulina. Standardized equation for hydrogen gas densities for fuel consumption applications1. Technical report, SAE Technical Paper, 2006.

[51] Tim Lieuwen, Vince McDonell, Domenic Santavicca, and Thomas Sattelmayer. Burner development and operability issues associated with steady flowing syngas fired combustors. *Combustion Science and Technology*, 180(6):1169–1192, 2008.

[52] Yu-Chun Lin, Peter Jansohn, and Konstantinos Boulouchos. Turbulent flame speed for hydrogen-rich fuel gases at gas turbine relevant conditions. *International journal of hydrogen energy*, 39 (35):20242–20254, 2014.

[53] RP Lindstedt and EM Vaos. Transported pdf modeling of high-reynolds-number premixed turbulent flames. *Combustion and Flame*, 145(3):495–511, 2006.

[54] AN Lipatnikov and J Chomiak. Lewis number effects in premixed turbulent combustion and highly perturbed laminar flames. *Combustion science and technology*, 137(1-6):277–298, 1998.

[55] U Maas. Simplifying chemical kinetics using intrinsic low-dimensional manifolds. In *Gas Phase Chemical Reaction Systems*, pages 334–342. Springer, 1996.

[56] B Magnussen. On the structure of turbulence and a generalized eddy dissipation concept for chemical reaction in turbulent flow. In *19th aerospace sciences meeting*, page 42, 1981.

[57] B Manickam. *Nunmerical Modelling and Simulation of Hydrogen Enriched Premixed Turbulent Flames with RANS and LES Approaches*. PhD thesis, Leibniz University of Hannover, 2012.

[58] SP Reddy Muppala, Naresh K Aluri, Friedrich Dinkelacker, and Alfred Leipertz. Development of an algebraic reaction rate closure for the numerical calculation of turbulent premixed methane, ethylene, and propane/air flames for pressures up to 1.0 mpa. *Combustion and Flame*, 140(4): 257–266, 2005.

[59] SPR Muppala and F Dinkelacker. Numerical modelling of the pressure dependent reaction source term for premixed turbulent methane/air flames. *Progress in Computational Fluid Dynamics, an International Journal*, 4(6):328–336, 2004.

[60] SPR Muppala, B Manickam, and F Dinkelacker. A comparative study of different reaction models for turbulent methane/hydrogen/air combustion. *Journal of Thermal Engineering*, 1(5):367–380, 2015.

[61] JR Nanduri, DR Parsons, SL Yilmaz, IB Celik, and PA Strakey. Assessment of rans-based turbulent combustion models for prediction of emissions from lean premixed combustion of methane. *Combustion science and technology*, 182(7):794–821, 2010.

[62] M.T. Nguyen, D.W. Yu, and S.S. Shy. General correlations of high pressure turbulent burning velocities with the consideration of lewis number effect. *Proceedings of the Combustion Institute*, 37 (2):2391 – 2398, 2019. ISSN 1540-7489. doi: https://doi.org/10.1016/j.proci.2018.08.049. URL http://www.sciencedirect.com/science/article/pii/S1540748918305935.

[63] Frans T.M. Nieuwstadt, Jerry Westerweel, and Bendiks J. Boersma. *Turbulence*. Springer International Publishing, Switzerland, 2016.

[64] Pavlos Nikolaidis and Andreas Poullikkas. A comparative overview of hydrogen production processes. *Renewable and sustainable energy reviews*, 67:597–611, 2017.

[65] Norbert Peters. Laminar flamelet concepts in turbulent combustion. In *Symposium (International) on Combustion*, volume 21, pages 1231–1250. Elsevier, 1988.

[66] Norbert Peters. The turbulent burning velocity for large-scale and small-scale turbulence. *Journal of Fluid mechanics*, 384:107–132, 1999.

[67] SL Plee and AM Mellor. Review of flashback reported in prevaporizing/premixing combustors. *Combustion and Flame*, 32:193–203, 1978.

[68] T. Poinsot and D. Veynante. *Theoretical and Numerical Combustion*. Edwards, 2005. ISBN 9781930217102. URL https://books.google.nl/books?id=cqFDkeVABYoC.

[69] Stephen B Pope. Pdf methods for turbulent reactive flows. *Progress in energy and combustion science*, 11(2):119–192, 1985.

[70] Stephen B. Pope. *Turbulent Flows*. Cambridge University Press, 2000. doi: 10.1017/CBO9780511840531.

[71] WJS Ramaekers, de Goey (LPH), van Oijen (JA), BA Albrecht, and RLGM Eggels. *The application of flamelet generated manifolds in modelling of turbulent partially-premixed flames*. Technische Universiteit Eindhoven, 2005.

[72] Sankaranarayanan Ravi and Eric L Petersen. Laminar flame speed correlations for pure-hydrogen and high-hydrogen content syngas blends with various diluents. *International journal of hydrogen energy*, 37(24):19177–19189, 2012.

[73] Jonathan D Regele, Edward Knudsen, Heinz Pitsch, and Guillaume Blanquart. A two-equation model for non-unity lewis number differential diffusion in lean premixed laminar flames. *Combustion and flame*, 160(2):240–250, 2013.

[74] Mahdi Saeedipour, Simon Schneiderbauer, Stefan Pirker, and Salar Bozorgi. Numerical simulation of turbulent liquid jet breakup using a sub-grid criterion with industrial application. In *Proceedings of ILASS-Europe annual conference on liquid atomization and spray systems, Bremen, Germany*, 2014.

[75] Tsan-Hsing Shih, William W Liou, Aamir Shabbir, Zhigang Yang, and Jiang Zhu. A new k-□ eddy viscosity model for high reynolds number turbulent flows. *Computers & fluids*, 24(3):227–238, 1995.

[76] F Tabet, B Sarh, M Birouk, and I Gökalp. The near-field region behaviour of hydrogen-air turbulent non-premixed flame. *Heat and Mass Transfer*, 48(2):359–371, 2012.

[77] YOSHIYUKI TANAKA, MASAHIRO NOGUCHI, HIRONOBU KUBOTA, and TADASHI MAKITA. Thermal conductivity of gaseous methane and sulfur hexafluoride under pressure. *Journal of Chemical Engineering of Japan*, 12(3):171–176, 1979.

[78] Luis Tay-Wo-Chong, Mathieu Zellhuber, Thomas Komarek, Hong G Im, and Wolfgang Polifke. Combined influence of strain and heat loss on turbulent premixed flame stabilization. *Flow, Turbulence and Combustion*, 97(1):263–294, 2016.

[79] Denis Thibaut and Sebastien Candel. Numerical study of unsteady turbulent premixed combustion: Application to flashback simulation. *Combustion and Flame*, 113(1-2):53–65, 1998.

[80] JA Van Oijen and LPH De Goey. Modelling of premixed laminar flames using flamelet-generated manifolds. *Combustion Science and Technology*, 161(1):113–137, 2000.

[81] JA Van Oijen, A Donini, RJM Bastiaans, JHM ten Thije Boonkkamp, and LPH De Goey. State-of-the-art in premixed combustion modeling using flamelet generated manifolds. *Progress in Energy and Combustion Science*, 57:30–74, 2016.

[82] Denis Veynante and Thierry Poinsot. Effects of pressure gradients on turbulent premixed flames. *Journal of Fluid Mechanics*, 353:83–114, 1997.

[83] Denis Veynante and Luc Vervisch. Turbulent combustion modeling. *Progress in energy and combustion science*, 28(3):193–266, 2002.

[84] J. Warnatz, Ulrich Maas, and Robert W. Dibble. *Combustion*. Springer-Verlag Berlin Heidelberg, Germany, 2006.

[85] aokomoriuta Wikimedia Commons. Law of the wall, 2011. URL https://commons.wikimedia.org/wiki/File:Law_of_the_wall_(English).svg.

[86] Victor Yakhot and Steven A Orszag. Renormalization group analysis of turbulence. i. basic theory. *Journal of scientific computing*, 1(1):3–51, 1986.

[87] Zhenghua Yan. *Numerical modeling of turbulent combustion and flame spread*. PhD thesis, Lund University Lund„ Sweden, 1999.

[88] VL Zimont, AN Lipatnikov, et al. A numerical model of premixed turbulent combustion of gases. *Chem. Phys. Reports*, 14(7):993–1025, 1995.

[89] Vladimir L Zimont. Gas premixed combustion at high turbulence. turbulent flame closure combustion model. *Experimental thermal and fluid science*, 21(1-3):179–186, 2000.